Theses and Dissertations

2017

Compact, Wideband, Low-dispersion, Multi-bit MEMS Phase Shifters

Vahid Gholizadeh
Lehigh University

Compact, Wideband, Low-dispersion, Multi-bit MEMS Phase Shifters

by

Vahid Gholizadeh

Presented to the Graduate and Research Committee
of Lehigh University
in Candidacy for the degree
of Doctor of Philosophy

in

Electrical Engineering

Lehigh University
August, 2017

Approved and recommended for acceptance as a dissertation in partial fulfillment of

the requirements for the degree of Doctor of Philosophy.

_____

Date

_____

Dr. James C. M. Hwang, Dissertation Advisor, Chair

_____

Accepted Date

Committee Members:

_____

Dr. Miltiadis Hatalis

_____

Dr. Svetlana Tatic-Lucic

_____

Dr. Charles L. Goldsmith

Acknowledgments

I would like to express my special appreciation and thanks to my advisor Professor James C. M. Hwang, you have been a tremendous mentor for me. I would like to thank you for encouraging my research and for allowing me to grow as an independent research scientist. Your advice on both research as well as on my career have been invaluable. I would also like to thank my committee members, Professor Miltiadis Hatalis, Professor Svetlana Tatic-Lucic and Doctor Charles L. Goldsmith for serving as my committee members even at hardship. I also want to thank you for letting my defense be an enjoyable moment, and for your brilliant comments and suggestions, thanks to you.

I would especially like to thank former and current colleagues at Compound Semiconductor Technology Laboratory (CSTL), particularly, Dr. Cristiano Palego, Dr. Yaqing Ning, Dr. Xi Luo, Mohammad Javad Asadi, Xiao Ma, Zhibo Cao, Xin Jin, Kevin Xiong, Xiaotian Du, Lei Li and Xiaopeng Wang who have made my graduate research at CSTL an enjoyable experience. I would also like to express my deep gratefulness to Dr. Charles Goldsmith at MEMtronics Corp. for his enormous support and inspiration

through my Ph.D. research.

A special thanks to my family. Words cannot express how grateful I am to my parents and my siblings for all those sacrifices that you've made on my behalf. Your prayer for me was what sustained me thus far. I would also like to especially thank to Saeid my dear brother. Thank you for supporting me for everything, and especially I can't thank you enough for encouraging me throughout this experience. To my dear sister Batool, I would like to express my thanks for being such a supportive sister always cheering me up. Finally, I thank my God. for letting me through all the difficulties. I have experienced Your guidance day by day. You are the one who let me finish my degree. I will keep on trusting You for my future.

Table of Contents

vi

List of Tables

List of Figures

xiii

Abstract

Low-dispersion phase shifters are key components for electrically large phased-array radar and communication systems. Unlike true-time-delay phase shifters with linear dispersion, low-dispersion phase shifters can be designed by switching between right-handed (low-pass) and left-handed (high-pass) states to achieve a constant phase shift over a wide bandwidth. However, the implementation of low-dispersion phase shifters with MEMS switches has been challenging. The designs to date suffer from either high insertion loss or high dispersion. Most important, they all occupy a large area and use a large number of MEMS switches, which negatively impact the yield and reliability, especially in view of the relatively immature RF MEMS technology.

This dissertation studies design, implementation, characterization and modeling of novel metamaterial-based low-dispersion multi-bit phase shifters that use single-pole-single-throw MEMS capacitive switches to switch between right-handed and left-handed states for a specified phase shift. Three-dimensional finite-element electromagnetic simulation was used to design the basic unit cells. Each phase shifter unit cell is based on a coplanar slow-wave structure with defected ground and uses two MEMS switches in series and parallel configurations. In this dissertation, for the first

1

time, we enhanced the maximum achievable phase shift of metamaterial-based MEMS phase shifter unit cell from 45° to 180°.

Thanks to our novel 180° unit cell design, for the first time, the number of required MEMS switches for multi-bit phase shifter was reduced to two times of bits count such that a 3-bit phase shifter requires only six MEMS switches. For 2-bit and 3-bit phase shifters fabricated on a 600-µm-thick sapphire substrate, a relatively flat phase shift was obtained across the band of 21.5–24.5 GHz with a root-mean-square phase error of less than 14°. Across the same frequency band, presented 2-bit and 3-bit phase shifters have less than 2.7 dB and 3.4 dB insertion loss, respectively.

Accurate modeling and electromagnetic simulations were performed to characterize the insertion loss of the presented phase shifters. The loss is mainly due to replacing gold for copper during fabrication as well as having lossy substrate. Furthermore, there is extra mismatch loss associated with the non-flat membrane as well as radiation loss. This can be further reduced by optimizing the MEMS switch and the coplanar waveguide. The present design principle appears to be sound and can lead to phase shifters with high performance, yield and reliability with low cost for electrically large phased-array antennas.

Chapter 1 Introduction

Controlling events has been a dream for human being throughout the history of mankind. Wireless control was pioneered by Nikola Tesla throughout 1890s [1]. The wireless control started by single and simple antennas and nowadays, simple antennas evolve into antenna arrays. Among different types of antenna arrays, phased array antennas are very important in which the beam can be steered electronically to point in any direction over a wide angle in front of the array, without physically moving the antenna. Phased array antennas have many advantages over traditional antenna concepts, including fast, reliable electronic beam steering, a compact volume profile, and graceful degradation with device failures.

Beam steering is very crucial for applications like tracking an object or short-range communication system to increase the quality of the communication. This steering can be "mechanical" to change the positions of the antennas or "electrical" to change the angle of the main beam with phase shifters. Mechanical beam steering is simple but slower and noisier than the electrical beam steering. Both mechanical and electrical beam steering techniques can be used depending on the requirements of the application. For

applications like tracking a fast object or daily life communication systems, fast beam

steering is required. That is why electrical beam steering with phase shifters is preferred

for these applications.

Phased-array multi-function radar and communication systems are ideal for

unmanned and micro air vehicles that possess challenging requirements for size, weight,

power consumption and cost. Whether a radar or communication system can meet such

challenging requirements is critically dependent on the design of not only the antenna,

but also key components such as phase shifters and transmit/receive electronics that are

required to drive individual antenna elements. For example, conventional phased-array

systems use one phase shifter and one transmit/receive electronic module to drive each

antenna element. The phase shifter is placed before the power amplifier to reduce its

burden. Since transmit/receive electronic modules are the most costly components of a

phase-array system, it is too expensive to be deployed in most unmanned and micro air

vehicles. However, recent advances in high-power gallium-nitride semiconductor

technology allow one transmit/receive electronic module to drive the combination of

several phase shifters and antenna elements, if and only if the phase shifters have

sufficiently low loss so that they can be placed after the electronic module (see Fig. 1-1)

4
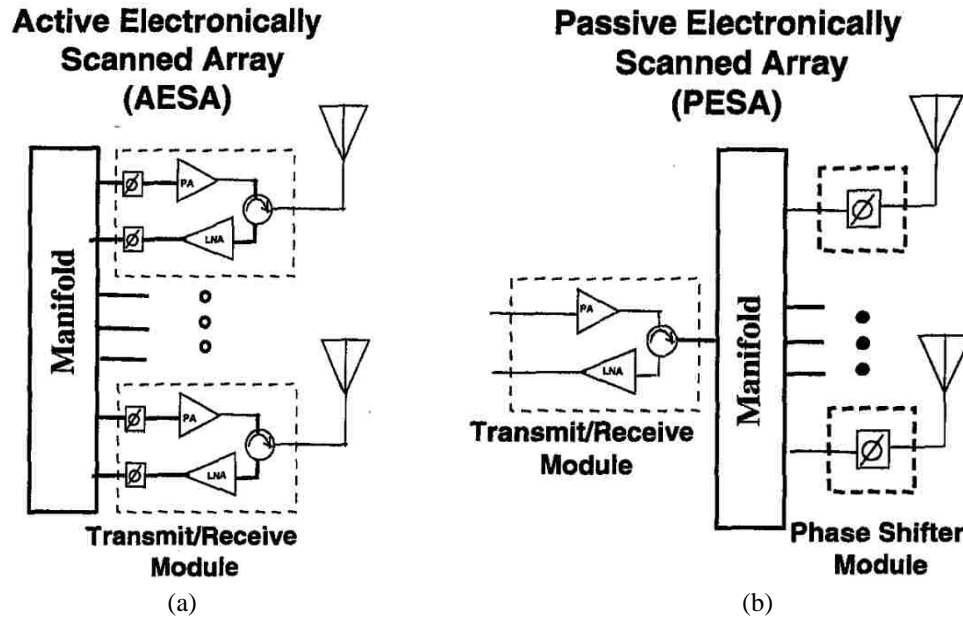
Fig. 1-1   Block diagram of a low-cost phased array in which a transmit/receive electronic module drives several integrated phase shifters and antenna elements [2].

[2]. In turn, this will allow the phase shifter to be integrated with the antenna on low-loss, low-cost insulators such as ceramics or plastics (as opposed to expensive semiconductors) for compact, light and conformal arrays that are ideally suited for aerospace platforms [3].

1.1 Phase Shifter Background

Phase shifters are two-port passive microwave devices that allow adjustable transmission phase angle (phase of S_{21}) of the incoming RF signal at the output port. Both the input and output ports should be perfectly impedance matched to result, ideally, in

5

zero attenuation of the outgoing signal and to obtain the best performance. Four important design criteria of a phase shifter are insertion loss, signal amplitude across states, reciprocity and phase flatness. Ideally, phase shifters provide low insertion loss in all phase states. While the loss of a phase shifter is often overcome using an amplifier stage, lower insertion loss phase shifters require less amplification and lower power to overcome the losses. The second important characteristic is phase shifters have equal amplitude for all phase states. Many systems using phase shifters must not experience amplitude changes in signal level as phase states are changed. The third important characteristic is that most phase shifters are reciprocal networks. This means they work effectively on signals passing through them in either direction. These three characteristics are used to describe the electrical performance of phase shifters. The fourth characteristic is whether they provide flat phase versus frequency, or true time delay [4]-[8].

Early on, phase shifting of the RF signal was obtained by mechanical adjustment of motors, which exhibited robust construction, consumed immense space, and were prone to aging and mechanical wear and tear. With the advent of microtechnology, however, mechanical adjustments were gradually replaced by electronic components such as PIN diodes, FET switches, and ferrite-type components, which could address all these issues

and, in addition, enhanced phase shift accuracy. The most important application of phase shifters is in radar and communication systems where they form an integral component in phased-array radar systems. Phased-array radars comprise an array of radiating elements that allow the radiated beam to be directed through desired angles in space. This beam scanning can be electronically controlled by varying the phase shift of multiple phase shifters connected in the feed network of each antenna element. Therefore, the number of phase-shift elements required for beam-scanning operations, occupy relatively less space and are easily integrable in the form of monolithic microwave ICs (MMICs).

1.2 Various Electronic Implementations of Phase Shifters

As stated in the above section, electronic phase shifters can be implemented with different electronic switch technologies such as PIN diodes, FET switches, and ferrite-type components. Table 1-1 compares the varied performances exhibited by PIN diodes, FET switches, ferrite-based devices, MMIC-based switches, and RF MEMS-based switching elements [9]. RF MEMS-based devices are reported to exhibit low-loss performance up to terahertz frequency ranges, thus aiding in the removal of quite a few amplifier stages commonly employed in standard radar modules.

Table 1-1   A Performance Comparison of Various Developing Phase Shifter Components

Parameters	PIN Diode	FET	Ferrite	MMIC	RF MEMS
Weight (OZ)	Light (0.5-1)	Light (<1)	Heavy (1-9)	Light (~ 0.01)	Light
Size (mm^2)	Small (1–5)	Small (0.1)	Large (~ cm)	Small (2–3)	Small
Cost	Low	Low	Very high	Low	High
Fabrication complexity	Commercially available	Commercially available	Complex in realization	Low complexity	Low complexity
High-frequency operation	L- to Q-band	L- to X-band	L- to W-band	L- to C-band	L-band to submm
Voltage (V)	±3–5	3–50	n/a	2–5	20–80
Current (mA)	3–20	0	10–100	0.15-1	0
Switching time (µs)	0.2-0.8	0.001-0.1	1-20	0.025-0.1	1-300
DC power consumption (mW)	5–100	0.05–0.1	10–50 W	0.05–0.1	0.05–0.1
Insertion loss @1 GHz (dB)	0.3–1.2	0.4–2.5	0.5–1.5	0.8–2	0.05–0.2
Isolation @1 GHz (dB)	20	20–40	40	40	>40
Power-handling (W)	~kW pulse; ~200 W CW	<10	>100	<1	<1
Figure-of-merit (GHz)*	1,500–2,000	300–400	n/a	n/a	>3,000

*Figure-of-merit (FOM) calculation: - $1/(2\pi R_{on}C_{off})$, where, R_{on} = on-state resistance and C_{off} = off-state capacitance. CW: continuous wave.

Ferrite-based devices exhibit moderate switching speed (~a few µs), low dc power consumption, and compatibility for MMIC integration. However, higher cost, fabrication

complexity, and frequency limitations have curtailed their use in wireless communications and rendered them impractical for mobile satellite communication devices. Unlike ferrites, semiconductor phase shifters using PIN diodes and FETs are inexpensive, smaller, and commercially available in packaged and ready-to-use forms. However, their applications are limited because of the significant insertion loss incurred at higher frequency ranges and their poor power-handling capability. PIN-diode phase shifters consume more dc power (3–10 mW per diode) than their FET-based equivalents but provide low-loss performance at X-band. While FET switches may have lower power handling, PIN diodes are known to handle multikillowatt power levels in pulsed-mode operation in radars. The advantage of FET-based phase shifters is that they consume virtually zero dc power and can promote on-chip integration with low noise, thereby reducing the expense associated with subsystem assembling in phased-array radar systems. However, FET-based designs introduce a significant amount of loss in the front end, around 4–6 dB at 12–18 GHz [10], [11] and 8–9 dB at 35 GHz for higher bit designs [12], [13].

1.3 RF MEMS Phase Shifters

Based on the comparisons in Table 1-1, we can infer that RF MEMS devices, in general, outperform conventional semiconductor-based modules. Therefore, the new technology of RF MEMS used for the development of microwave and millimeter-wave circuits can replace the semiconductor switching elements currently employed in various application areas, including: phased-array radar systems. A typical phased-array radar system consists of three major components: 1) the antenna array, 2) the phase shifter modules, and 3) a feed network or a power divider network. The radar detects a target by scanning the field of view with a directive beam. Scanning is done electronically, through shifting the beam of an antenna array by means of phase shifter modules. RF MEMS phase shifters promote electronic antenna beamscanning ability, which offers low-loss performance, light weight, and an exceedingly low cost compared to an entire antenna system being physically rotated by means of mechanical motors.

The advantages offered by RF MEMS technology can be briefly summarized as follows [11]-[13], [14]:

1) low-loss performance at high frequency ranges, 2) enhanced isolation, 3) wide-band performance, 4) minimal dc power consumption (when the switch is in the OFF state), 5)

high linearity, 6) high power-handling capacity, 7) low parasitic effects. RF MEMS-based switches provide low-loss performance in phase shifters over a wide range of frequencies (10–120 GHz). The worst-case insertion loss of the present state-of-the-art five-bit MEMS phase shifters is -1 dB at 10–35 GHz, which represents a 5–6 dB improvement over contemporary on-wafer designs using FET switches or PIN diodes[15]. This, in turn, results in a 10–12dB improvement (2-way) in phased-array radar systems, and so several amplifier stages can be eliminated in the radar transmit/receive module as shown in Fig. 1-1, rendering dc power reduction of 20–100 mW per element within the X- to V-band frequency ranges [15]. In addition, MEMS switches can be fabricated directly with the antenna element on ceramic, quartz, glass, or high-resistivity silicon substrates, potentially resulting in relatively low-cost phased arrays, especially in millimeter-wave reflect-array systems. The switching of MEMS switches is slow, on the order of 1–20 μs, which allows them to be used in virtually all systems except for fast airborne or transmit/receive applications. The present state-of-the art reports show that the lifetime of RF MEMS capacitive switches has exceeded 100 billion cycles [16] without failure, which suggests the suitability of RF MEMS-based devices in airborne, satellite, and communication application areas.

1.4 RF MEMS Phase Shifter Implementations
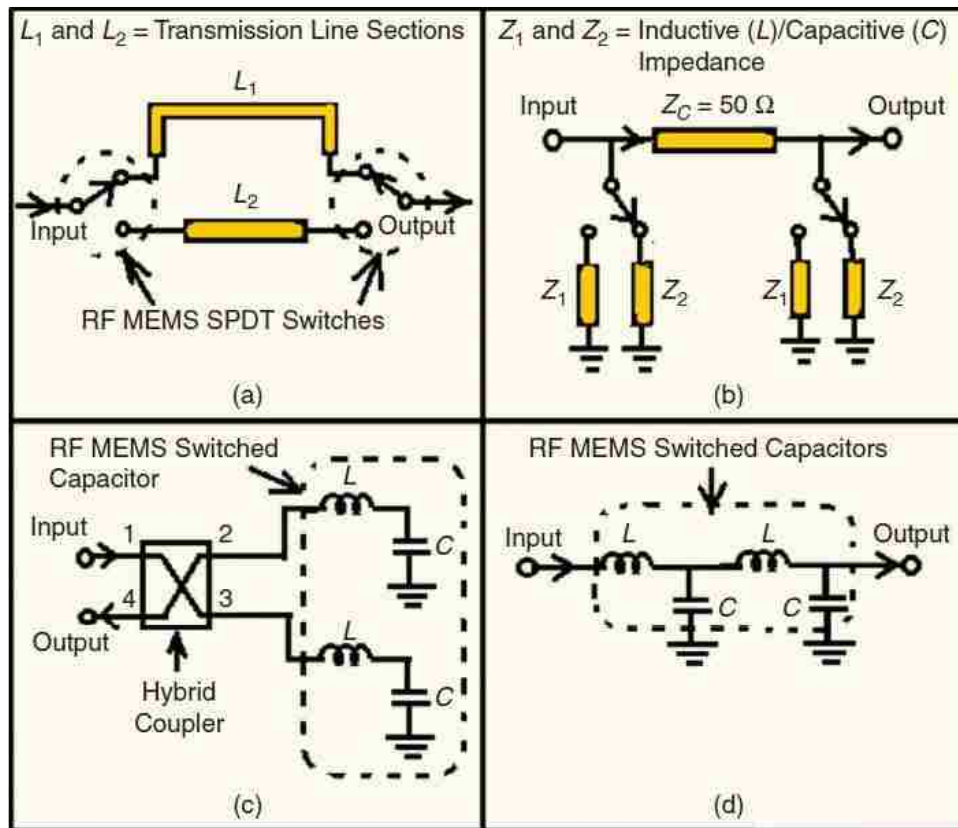
Fig. 1-2   The schematic layouts of (a) switched-line, (b) loaded-line, (c) reflection, and (d) distributed-line RF MEMS phase shifter design implementations. SPDT: single-pole double-throw.

Fig. 1-2 depicts the most common phase shifter implementations by RF MEMS switches. The switched-line implementation involves switching between two transmission line sections of unequal lengths to introduce the desired amount of phase shift [14]. The basic idea governing the operation of a loaded-line phase shifter [17][19] is to load a transmission line with two different reactive impedance networks. A central

line segment connecting the two networks may be utilized as a matching network to maintain input and output impedances close to 50 Ω [14].

In contrast to the previously described switched-line and loaded-line phase shifter implementations, reflection phase shifters use 3-dB hybrid couplers as one of their major components. The reflection-type N-bit phase shifter can be implemented by two different techniques employing a succession (say, "N") of MEMS series or shunt switches on a transmission line. Such a phase shifter results in narrow bandwidth output for an N-bit design and is dependent on the phase delay [20].

Distributed-line—or, more precisely, distributed MEMS transmission line (DMTL)—phase shifters are by far the most popular of all RF MEMS-based phase shifters. Their operating principle is based on the concept of periodically loading a transmission line, i.e., a CPW or microstrip line, by passive components such as switched capacitors or varactors. These varactors are realized by mechanical bridge/beam-like structures permanently anchored at one or more terminations (cantilever or fixed beam type) with the ground planes of chosen transmission line networks. Such periodic structures exhibit slow wave-behavior ($v_p \ll c$, v_p = phase velocity, c = speed of light in a vacuum) characteristics. These types of circuits are often referred to as synthetic line,

13

slow wave, or distributed transmission line phase shifters [9].

1.5 *Metamaterial-based Phase Shifter Design*

A metamaterial proposed by Victor Veselago is an engineered material which have a

property that is not found in nature [21]. A media with metamaterial characteristics can be

obtained by developing circuits which, under certain conditions, model metamaterial

properties. Using different lattice structures or periodic repetition of unit cells, different

types of two-dimensional metamaterials have been suggested [22]. Recent advances in

metamaterials allow, for the first time, non-dispersive phase shifters to be realized, which

may greatly simplify the operation of frequency-agile and broadband-modulated

phased-array radar and communications systems. Conventional true-time-delay phase

shifters are dispersive, so that their phases typically vary linearly with frequency. By

judiciously combining right-handed natural materials and left-handed metamaterials with

different dispersion characteristics, a phase shifter can be constructed with a constant

phase shift across a wide bandwidth [23].

As shown in Fig. 1-3(a), dispersion is a natural phenomenon where the phase of a

normal   (right-handed)   transmission   line   increases   with   increasing
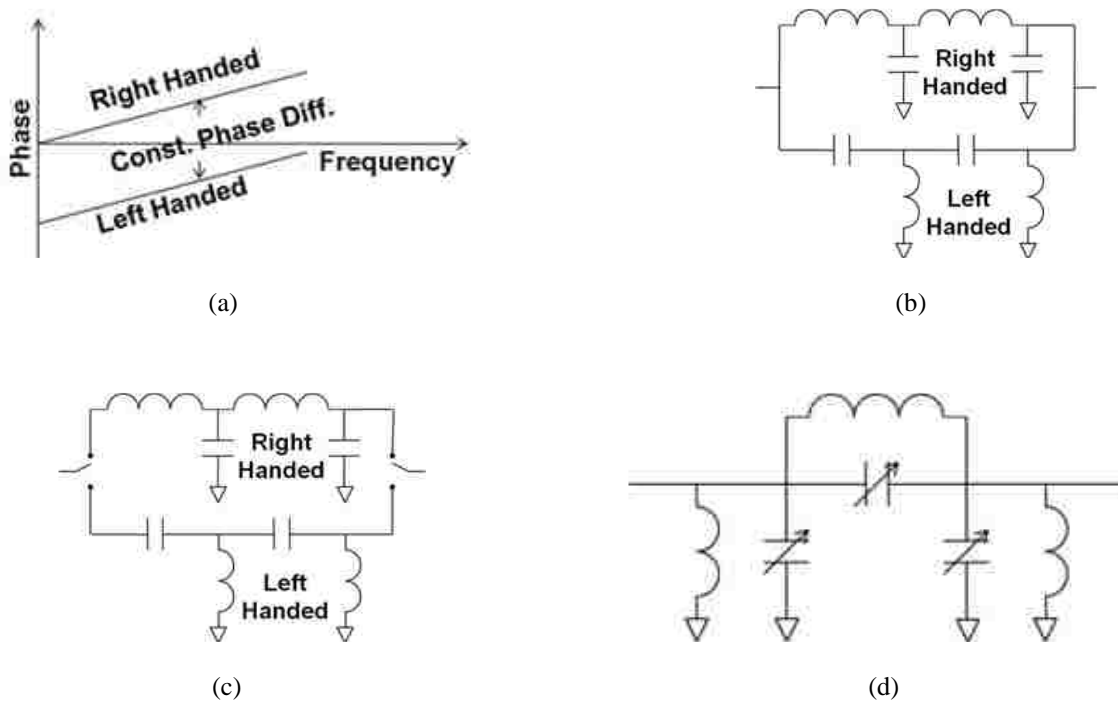
Fig. 1-3   (a) Opposite dispersion characteristics of right- and left-handed transmission lines, (b) composite right-/left-handed (CRLH) transmission line, (c) switchable CRLH transmission line, and (d) dual CRLH transmission line.

frequency. Alternatively, the absolute magnitude of phase for left-handed transmission lines decreases with increasing frequency; the phase increases (becomes less negative) in a relative sense with increasing frequency. Thus, when using a phase shifter to switch between right- and left-handed modes, the resulting phase shift can be constant over a wide bandwidth.

Fig. 1-3(b) illustrates a composite right/left-handed (CRLH) transmission line [24]-[25]. The right-handed transmission line resembles a distributed low-pass filter of

15

series inductors (*L*) and shunt capacitors (*C*); the left-handed transmission line resembles a distributed high-pass filter of series *C*s and shunt *L*s. Therefore, the CRLH structure behaves like a right- and left-handed transmission line at low and high frequencies, respectively. Fig. 1-3 (c) shows that two switches can be added so that the CRLH transmission line can switch between right- and left-handed modes at the same frequency, although such a switchable CRLH transmission line tends to be bulky. Fig. 1-3(d) shows that three fixed inductors and three variable capacitors can form a dual CRLH transmission line in a more compact manner [26]. When the series capacitance is small and the shunt capacitances are large, the transmission line is right-handed. When the series capacitance is large and the shunt capacitances are small, the transmission line is left-handed. Such a dual CRLH transmission line can be used to realize non-dispersive phase shifters that are compact and low loss.

CRLH devices have been demonstrated in the literature, such as leaky-wave antennas [27], and phased shifters for series-fed network of antenna arrays [28]-[30], or compact dual-band couplers [31]. However, most of these designs are either narrowband designs based on *L-C* resonances or bulky layouts based on surface-mount components.

One of the most common designs for compact low-dispersion phase shifters is based

on high/low-pass *LC* filters to create insertion phase advances (with high-pass) and delays (with low-pass) [32]. The main difference between true-time-delay and low-dispersion phase shifters is that the first one possesses linear dispersion while the second one can be designed to achieve a constant phase shift over a wide bandwidth in mm-wave frequencies by switching between low-pass and high-pass states [33]-[35].

Micro-electromechanical (MEM) capacitive switches [36], as variable capacitors can be monolithically integrated in slow-wave structures to form dual CRLH transmission line, thereby realizing low-dispersion phased shifters that are compact, lightweight, low cost and low power consumption [37]-[44]. Conventional diode- or transistor-based 4-bit phase shifters typically have 5-10 dB loss in the Ka-band. The present design together with previous RF MEMS phase shifter designs show that replacing the diode or transistor switches with MEMS switches, phase shifters can have 1-3 dB loss in the Ka-band.

Further innovation can be done by tightly wrapping a slow-wave structure around a small number of closely spaced MEMS switches and by incorporating a defected ground structure in some of the MEMS switches. The additional degrees of freedom afforded by the MEMS switches allow the slow-wave structure to be impedance matched over a wide frequency band. These innovations will make the phase shifters even more compact,

lower loss, and lower cost, in addition to having a constant phase shift across a wide bandwidth.

However, the implementation of low-dispersion phase shifters with micro-electromechanical systems (MEMS) switches has been challenging. The designs to date are either too lossy to be competitive to purely electronic phase shifters [48] or dispersive [33], [49]. Particularly, they all occupy a large area and use a large number of MEMS switches, which negatively impact the yield, especially because of the relatively immature MEMS fabrication and reliability.

1.6 Organization of the Dissertation

After introducing phase shifters and associated significant topics in Chapter 1, the compact, low-dispersion, metamaterial-based MEMS phase shifter design and simulation are discussed in Chapter 2, where simulation helped to optimize the circuit performance in terms of insertion loss and RMS phase error. Following the simulation, Chapter 3 presents the initial measured results of the fabricated MEMS phase shifter circuit with real MEMS switches. All designed switches, unit cells and multi-bit phase shifters have been characterized experimentally. After characterizing the design, experimental

18

demonstration of MEMS phase shifter with faux switches (switches with membrane deposited in actuated state) is presented in Chapter 4, where the source of extra insertion loss has been experimentally examined. Finally, the conclusions of this dissertation and recommendations for future research are presented in Chapter 5.

References

[1] My Inventions: The Autobiography of Nikola Tesla, Hart Brothers, 1982, Ch. 5, ISBN 0-910077-00-2.

[2] B. R. Norvell, R. J. Hancock, J. K. Smith, M. L. Pugh, S. W. Theis, and J. Kviatkofsky, "Microelectromechanical switch (MEMS) technology applied to electronically scanned arrays for space based radar," in *IEEE Aerospace Conf. Proc.*, 1999, pp. 239–247.

[3] J. C. Rock. T. D. Hudson, B. Wolfson, D. Lawrence, B. Pillans, A. R. Brown, L. A. Coryell, and R. A. Milburn, "Design, fabrication and evaluation of a MEMS-based Ka-band, 16-element subarray," *U. S. Army RDECOM Technical Report RDMR-WD-09-24*, Nov. 2009.

[4] Antenna Engineering Handbook, 4th Ed., by John Volakis, McGraw-Hill, 2007 (Chapter 21).

[5] Phased Array Antennas, 2nd Ed., by R. C. Hansen, John Wiley & Sons, 1998.

[6] Phased Array Antenna Handbook, 2nd Ed., by Robert Mailloux, Artech House, 2005.

[7] Phased Array Antennas by Arun K. Bhattacharyya, John Wiley & Sons, 2006.

[8] Microwave Solid State Circuit Design, 2nd Ed., by Inder Bahl and Prakash Bhartia, John Wiley & Sons, 2003 (Chapter 12).

[9] A. Chakraborty and B. Gupta, "Paradigm Phase Shift," *IEEE Microwave Mag. 18*, no. 1, pp. 22−41, 2017.

[10] J. Wallace, H. Redd, and R. Furlow, "Low cost MMIC DBS chip-sets for phased array applications," *IEEE MTT-S Int. Microwave Symp. Dig.*, Anaheim, CA, 1999, pp. 677−680.

[11] C. F. Campbell and S. A. Brown, ″A compact 5-bit phase-shifter MMIC for K-band satellite communication systems,″ *IEEE Trans. Microwave Theory Tech.*, vol. 48, no. 12, pp. 2652−2656, 2000.

[12] M. J. Schindler and M. E. Miller, ″A 3-bit K/Ka band MMIC phase shifter,″ *IEEE MTT-S Int. Microwave Symp. Dig.*, 1988, pp. 95−98.

[13] K. Maruhashi, H. Mizutani, and K. Ohata, ″A Ka-band 4-bit monolithic phase shifter using unresonated FET switches,″ *IEEE MTT-S Int. Microwave Symp. Dig.*, 1998, pp. 51−54.

[14] D. Uttamchandani, *Handbook of MEMS for Wireless and Mobile Applications.* Cambridge, U.K.: Woodhead, 2013, pp. 136–175.

[15] G. M. Rebeiz, G. L. Tan, and J. S. Hayden, "RF MEMS phase shifters: Design and applications," *IEEE Microwave Mag.*, vol. 3, no. 2, pp. 72–81, 2002.

[16] C. L. Goldsmith, D. I. Forehand, Z. Peng, J. C. M. Hwang, and J. L. Ebel, "High-cycle life testing of RF MEMS switches," in *IEEE Int. Microwave Symp*. Dig., 2007, pp. 1805–1808.

[17] H. A. Atwater, "Circuit design of the loaded-line phase shifter," *IEEE Trans. Microwave Theory Tech.*, vol. 33, no. 7, pp. 626–634, 1985.

[18] W. A. Davis, "Design equations and bandwidth of loaded-line phase shifter," *IEEE Trans. Microwave Theory Tech.*, vol. 22, no. 5, pp. 561–563, 1974.

[19] F. L. Opp and W. F. Hoffman, "Design of digital loaded-line phase-shift networks for microwave thin-film applications," *IEEE Trans. Microwave Theory Tech.,* vol. 16, no. 7, pp. 462–468, 1968.

[20] G. M. Rebeiz, RF MEMS: *Theory, Design, and Technology*. New York: Wiley, 2003, pp. 259–325.

[21] V.G. Veselago, "The electrodynamics of substances with simultaneously negative values of ε and μ," *Sov. Physics – Usp.*, vol.47, January-February 1968, pp. 509–514.

[22] C. Caloz, and T. Itoh, "Positive/negative refractive index anisotropic 2-D metamaterials," *IEEE Microwave and Wireless Components Letters*, Vol.13, No.12, pp. 547–549, Dec. 2003.

[23] J. Perruisseau-Carrier, T. Lisec, and A. Skrivervik, ″Circuit model and design of siliconintegrated CRLH-TLs analogically controlled by MEMS,″ *Microwave Optical Technology Lett.,* vol. 48, pp. 2496–2499, Dec. 2006.

[24] C. Caloz and T. Itoh, Electromagnetic Metamaterials Transmission Line Theory Microwave Applications. Hoboken, NJ: Wiley - IEEE Press, 2005.

[25] G. Eleftheriades and K. Balmain, Negative-Refraction Metamaterials Fundamental Principles Applications. Hoboken, NJ: Wiley - IEEE Press, 2005.

[26] C. Caloz, "Dual composite right/left-handed (D-CRLH) transmission line metamaterials," *IEEE Microwave Wireless Components Lett.*, vol. 16, pp. 585–587, Nov. 2006.

[27] A. Grbic, and G. Eleftheriades, "Experimental verication of backward-wave radiation from a negative refractive index metamaterial," *J. Applied Physics*, vol. 92, pp. 5930–5935, Nov. 2002.

[28] M. Antoniades, and G. Eleftheriades, "Compact linear lead/lag metamaterial phase shifters for broad-band applications," *IEEE Antennas Wireless Propagation Lett.*, vol. 2, no. 7, pp. 103–106, 2003.

[29] Z. Qi, Z. Zhongxiang, X. Shanjia, and D. Wenwu, "Millimeter wave microstrip array design with CRLH-TL as feeding line," in *IEEE Antennas Propagation Soc. Int. Symp.*, vol. 3, 2004, pp. 3413–3416.

[30] J. Perruisseau-Carrier, and A. Skrivervik, "Composite right/left handed transmission line metamaterial phase shifters (MPS) in MMIC technology," *IEEE Trans. Microwave Theory Tech.*, vol. 54, pp. 1582–1589, Apr. 2006.

[31] I.-H. Lin, M. DeVincentis, C. Caloz, and T. Itoh, "Arbitrary dual-band components using composite right/left-handed transmission lines," *IEEE Trans. Microwave Theory Tech.*, vol. 52, pp. 1142–1149, Apr. 2004.

[32] Stepan Lucyszyn, *Advanced RF MEMS,* Cambridge University Press, 2010 (Chapter 11).

[33] R. V. Garver, "Broad-band diode phase shifters," *IEEE Trans. Microw. Theory Techn.*, vol. 20, no. 5, pp. 314−323, May 1972.

[34] J. Perruisseau-Carrier, T. Lisec, and A. Skrivervik, "Circuit model and design of silicon integrated CRLH-TLs analogically controlled by MEMS," *Microwave Optical Technology Lett.,* vol. 48, pp. 2496−2499, Dec. 2006.

[35] D. Kuylenstierna, A. Vorobiev, P. Linner and S. Gevorgian, "Composite right/left handed transmission line phase shifter using ferroelectric varactors," *IEEE Microw. and Wireless Components Lett.,* vol. 16, no. 4, pp. 167–169, April 2006.

[36] C. Goldsmith, et al, "Micromechanical microwave switching," US Patent No. 5,619,061, Apr. 8, 1997.

[37] C. Palego, Y. Ning, V. Gholizadeh, X. Luo, J. C. M. Hwang, and C. L. Goldsmith, "Compact, wideband, low-dispersion, metamaterial-based MEMS phase shifters," in *IEEE MTT-S Int. Microwave Symp. Dig.*, Jun. 2014, pp. 1–4.

[38] B. Lakshminarayanan and T. M. Weller, "Design and modeling of a 4-bit slow-wave phase shifter," *IEEE Trans. Microwave Theory Techniques*, vol. 54, no. 1, pp. 120−127, Jan. 2006.

[39] B. Lakshminarayanan and T. M. Weller, "Optimization and implementation of impedance-matched true-time-delay phase shifters on quartz substrate," *IEEE Trans. Microwave Theory Techniques*, vol. 55, no. 2, pp. 335−342, Feb. 2007.

[40] M. Bakri-Kassem, R. Mansour, and S. Safavi-Naeini, "Novel millimeter-wave slow-wave phase shifter using MEMS technology," in *Proc. European Microwave Conf.,* Oct. 2011, pp. 1079−1082.

[41] M. Bakri-Kassem and R. Mansour, "A novel self collapsed corrugated MEMS phase shifter," in *Proc. European Microwave Conf.,* Oct. 2013, pp. 360−363.

[42] C. Palego, Z. Peng, J. C. M. Hwang, D. Scarbrough, D. I. Forehand, and C. L. Goldsmith, "Compact Ka-band phase shifters using MEMS capacitive switches," in *Proc. European Microwave Conf.,* Sep. 2009, pp. 1864−1867.

[43] J. C. M. Hwang, and C. L. Goldsmith, ″Robust RF MEMS switches and phase shifters for aerospace applications,″ in *Proc. IEEE Radio-Frequency Integration Technology Symp.,* Dec. 2009, pp. 245−248.

[44] C. Palego, Z. Peng, J.C.M Hwang, D. Scarbrough, C.L. Goldsmith, ″Novel Ka-band phase shifters using MEMS capacitive switches,″ *2010 IEEE 11th Annual Wireless and Microwave Technology Conference (WAMICON),* 12−13 April 2010.

[45] G. M. Rebeiz, G.-L. Tan, and J. S. Hayden, "RF MEMS phase shifters: design and applications," *IEEE Microwave Mag.*, pp. 72−81, June 2002.

[46] M. Kim, J. B. Hacker, R. E. Mihailovich, and J. F. DeNatale, "A DC-to-40 GHz four-bit RF MEMS true-time delay network," *IEEE Microwave Wireless Components Lett*., vol. 11, pp. 56−58, Feb. 2001.

[47] N. S. Barker, and G. M. Rebeiz, "Optimization of distributed MEMS transmission-line phase shifters—U-band and W-band designs," *IEEE Trans. Microwave Theory Techniques*, vol. 48, pp. 1957−1966, Nov. 2000.

[48] M. A. Morton and J. Papapolymerou, "A packaged MEMS-based 5-bit X-Band high-pass/low-pass phase shifter," *IEEE Trans. Microwave Theory Tech.*, vol. 56, no. 9, pp. 2025−2031, Sep. 2008

[49] V. Gholizadeh, Y. Ning, X. Luo, C. Palego, J. C. M. Hwang, and C. L. Goldsmith, "Improved Compact, Wideband, Low-dispersion, Metamaterial-based MEMS Phase Shifters," in *IEEE Int. Wireless Symp. Dig.*, Shenzhen, China, Mar. 2015, pp. 1−4.

[50] V. Gholizadeh, M. J. Asadi, Y. Ning, C. Palego, J. C. M. Hwang, D. Scarbrough, and C. L. Goldsmith, "Low-dispersion metamaterial-based phase shifters with reduced size and number of MEMS switches," in *IEEE MTT-S Int. Wireless Symp. Dig.,* Shanghai, China, Mar. 2016, pp. 1−4.

[51] V. Gholizadeh, M. J. Asadi, Y. Ning, C. Palego, J. C. M. Hwang, D. Scarbrough, and C. L. Goldsmith, "Low-dispersion 180° phase shifter using two synchronized MEMS switches," in *Lester Eastman Conference,* Bethlehem, PA, 2016, pp. 35−37.

Chapter 2 Design of Metamaterial-based MEMS Phase Shifter

The most critical aspect in design of the low-loss digital MEMS phase shifter is to increase the phase shift of the most significant bit (MSB) to 180° while limiting its insertion loss. While low dispersion phase shifters have been designed using PIN diodes several decades ago [1], their implementation using micro-electromechanical systems (MEMS) capacitive switches is rather recent [2]-[3]. However, the implementation of low-dispersion phase shifters with MEMS switches has been challenging. The designs to date are either too lossy to be competitive to purely electronic phase shifters [2] or dispersive [3][5]. Particularly, because of their limited MSB phase shift (45°), they all occupy a large area and use a large number of MEMS switches, which negatively impact the yield, especially because of the relatively immature MEMS fabrication and reliability. The novelty of the present design of metamaterial-based MEMS phase shiter lies in a 4X increase of the phase shift of MSB to 180° using only two MEMS switches so a 3-bit phase shifter could be realized by using only six MEMS switches[6]-[7]. This not only shrinks the circuit footprint but also reduces the loss and improves the yield. Moreover, this design is based on a temperature independent MEMS switch which uses geometrical approach to overcome the thermal and residual stress in the membrane [8]-[11].

In this chapter, we will first briefly go through the principles of the CRLH transmission line and low-dispersion phase shifter. Then we will introduce the temperature independent switch that we have developed. Following switch introduction and simulation results, we will introduce the novel phase shifter unit cell and it's circuit model. After that we will also show how the previously designed unit cells with smaller phase shifts were adapted in to our design. Finally, the simulation results of the cascaded multi-bit phase shifters with 2, 3 and 4 unit cells will be presented, where optimization of the whole circuit will be explored to minimize the coupling between neighboring unit cells.

2.1 Right-Handed, Left-Handed and CRLH Transmission Lines

Practical transmission lines (microstrip, CPW etc.) are homogenous transmission media. The theory of operation for these transmission lines can be explained using distributed equivalent circuits that are obtained by cascading a large number of cells (such that the length of a cell becomes much shorter in comparison to the wavelength) [12]-[14]. Fig. 2-1(a) and 2-1(b) show the equivalent circuits of a loss-less unit cell for RH-TL and LH-TL, respectively. In these circuits, L_R, C_R and L_L, C_L are the distributed

27
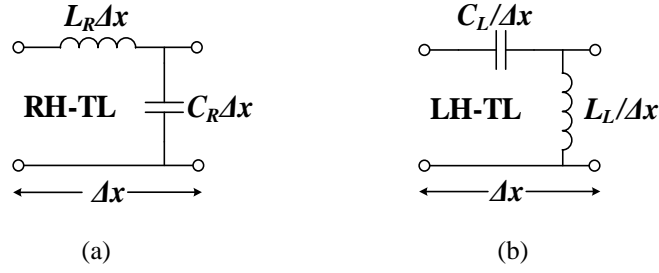
Fig. 2-1 Equivalent circuits with distributed elements, for a cell of (a) RH-TL and (b) LH-TL.

per-unit length inductance and capacitance for RH-TL and LH-TL respectively. The

propagation constant and the characteristic impedance of a TL are given by:

$$\gamma = \sqrt{Z(\omega)Y(\omega)} = \alpha + j\beta \quad \text{and} \quad Z_0 = \sqrt{\frac{Z(\omega)}{Y(\omega)}}, \qquad (2\text{-}1a,b)$$

respectively, where $Z(\omega)$ and $Y(\omega)$ are the per-unit length impedance of the series branch

and the admittance of the parallel branch in Fig. 2-1(a) and Fig. 2-1(b), α is the

attenuation constant and β is the phase constant. In the case of Fig. 2-1(a) and Fig. 2-1(b)

where the line is loss-less $\alpha = 0$, the propagation constant is pure imaginary, while the

impedance is pure real. From Fig. 2-1(a), for RH-TL we can write:

$$Z(\omega) = j\omega L_R \quad \text{and} \quad Y(\omega) = j\omega C_R. \qquad (2\text{-}2 \text{ a,b})$$

Plugging equation (2-2) in equation (2-1) gives:

$$\beta_{RH-TH} = \omega\sqrt{L_R C_R} \quad \text{and} \quad Z_{0,RH-TL} = \sqrt{\frac{L_R}{C_R}}. \qquad (2\text{-}3 \text{ a,b})$$

28
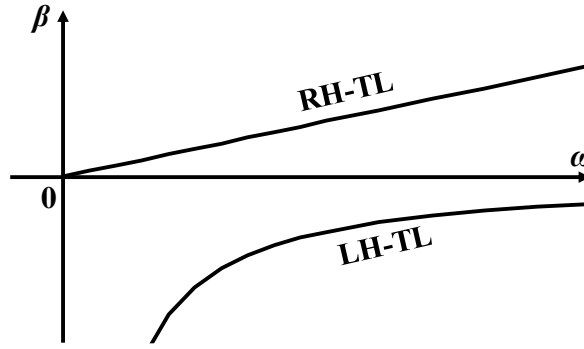
Fig. 2-2   Graphic representation of the dispersion equations for lossless RH-TL and LH-TL.

Similarly, from Fig. 2-1(b), for LH-TL we can write:

$$Z(\omega) = \frac{1}{j\omega C_L} \quad \text{and} \quad Y(\omega) = \frac{1}{j\omega L_L}. \tag{2-4 a,b}$$

Plugging equation (2-4) in equation (2-1) gives:

$$\beta_{LH-TH} = -\frac{1}{\omega\sqrt{L_L C_L}} \quad \text{and} \quad Z_{0,LH-TL} = \sqrt{\frac{L_L}{C_L}}. \tag{2-5 a,b}$$

The equations (2-3 a) and (2-5 a) are the dispersion equations for RH-TL and LH-TL, respectively. The qualitative graphic representation of these equations is given in Fig. 2-2. It is evident from Fig. 2-2 that the phase velocity, $V_p = \dfrac{\omega}{\beta}$ is positive for RH-TL and negative for LH-TL. The group velocity, $V_g = \dfrac{1}{\dfrac{\partial \beta}{\partial \omega}}$, is positive for both RH-TL and LH-TL since the dispersion slope is the same for both. Therefore, the energy transport is, from generator to load in both cases, but since the phase velocity is negative for LH-TL,

29
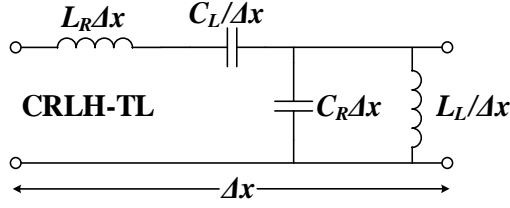
Fig. 2-3   The distributed equivalent circuit for a cell of CRLH-TL.

the wave is propagated backwards (from load to generator).

The pure LH structure as shown in Fig. 2-1(b) is not practically possible because of unavoidable RH parasitics. Therefore, a CRLH structure is the most general form of a structure with LH behavior. The equivalent circuit of a loss-less CRLH-TL is a combination of the equivalent circuits for RH-TL and LH-TL as shown in Fig. 2-3. Like RH-TL and LH-TL, Δx must be small enough compared to the wavelength. From Fig. 2-3, for loss-less CRLH-TL we can write:

$$Z(\omega)= j\left(\omega L_R - \frac{1}{\omega C_L}\right) \quad \text{and} \quad Y(\omega)= j\left(\omega C_R - \frac{1}{\omega L_L}\right). \tag{2-6 a,b}$$

Plugging equation (2-6) in equation (2-1 a) and $\alpha = 0$ (lossless circuit) gives:

$$\beta_{CRLH-TL} = \sqrt{-\left(\omega L_R - \frac{1}{\omega C_L}\right)\left(\omega C_R - \frac{1}{\omega L_L}\right)}$$

$$= s(\omega)\sqrt{\omega^2 L_R C_R + \frac{1}{\omega^2 L_L C_L} - \left(\frac{L_R}{L_L} + \frac{C_R}{C_L}\right)} \tag{2-7}$$

where

30

$$s(\omega) = \begin{cases} -1 & \text{if } \omega < \omega_{\Gamma_1} = min\left(\dfrac{1}{\sqrt{L_R C_L}}, \dfrac{1}{\sqrt{L_L C_R}}\right) \\[2em] +1 & \text{if } \omega > \omega_{\Gamma_2} = max\left(\dfrac{1}{\sqrt{L_R C_L}}, \dfrac{1}{\sqrt{L_L C_R}}\right) \end{cases} \qquad (2\text{-}8)$$

For $\omega \in (\omega_{\Gamma_1}, \omega_{\Gamma 2})$, the phase constant, β, is an imaginary number, therefore the propagation constant, γ, is a real number, which means that the signal on the line is attenuated. Therefore, for $\omega \in (\omega_{\Gamma_1}, \omega_{\Gamma 2})$ the circuit behaves as a band-stop filter. If $\omega_{\Gamma_1} = \omega_{\Gamma 2}$ then there is no stop-band. The circuit with $\omega_{\Gamma_1} \neq \omega_{\Gamma 2}$ is called an unbalanced circuit, while the circuit with $\omega_{\Gamma_1} = \omega_{\Gamma 2}$ is called a balanced circuit. By considering the equations (2-8), we get that the circuit is balanced, i.e. $\omega_{\Gamma_1} = \omega_{\Gamma 2}$, when:

$$L_R C_L = L_L C_R. \qquad (2\text{-}9)$$

In this case, we represent the frequencies ω_{Γ_1} and $\omega_{\Gamma 2}$ with a new frequency called ω_0 which is derived as

$$\omega_0 = \frac{1}{\sqrt{L_R C_L}} = \frac{1}{\sqrt{L_L C_R}} = \frac{1}{\sqrt[4]{L_R C_L L_L C_R}}. \qquad (2\text{-}10)$$

From the equations (2-7) and (2-10), for the balanced circuit, $\beta = 0$ at ω_0. The dispersion equations (2-7) shows that for $\omega < \omega_{\Gamma_1}$ (or $\omega < \omega_0$, for the balanced circuit), the line behaves like a LH-TL, while for $\omega > \omega_{\Gamma 2}$ (or $\omega > \omega_0$, for the balanced circuit),
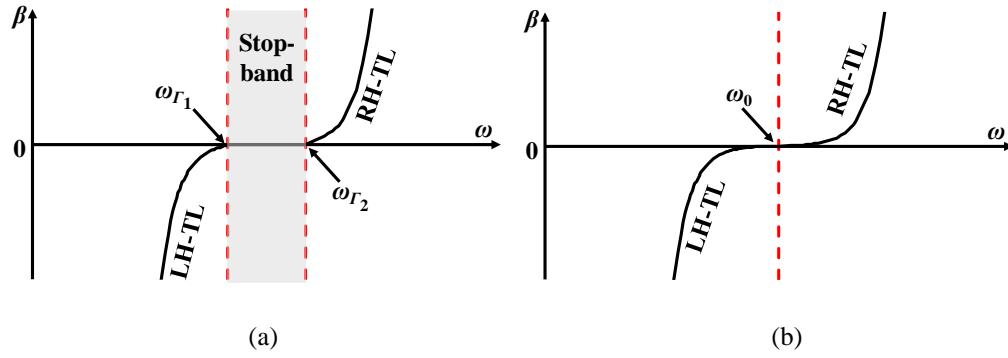
Fig. 2-4   Graphic representation of the dispersion equations for loss-less CRLH-TL, for (a) unbalanced and (b) balanced cases.

the line behaves as a RH-TL. The qualitative graphic representations of the dispersion equation (2-7), for the unbalanced and balanced circuits, are shown in Fig. 2-4(a) and Fig. 2-4(b), respectively.

The characteristic impedance of the unbalanced CRLH-TL is obtained by plugging equation (2-6 a,b) in equation (2-1 b) as:

$$Z_{0,CRLH-TL} = \sqrt{\frac{L_L}{C_L}} \sqrt{\frac{\omega^2 L_R C_L - 1}{\omega^2 L_L C_R - 1}}. \tag{2-11}$$

Applying equation (2-9) in equation (2-11) results in the characteristic impedance of the balanced CRLH-TL as:

$$Z_{0,CRLH-TL} = \sqrt{\frac{L_L}{C_L}} = \sqrt{\frac{L_R}{C_R}} \tag{2-12}$$

or, with the values (2-3 b) and (2-5 b), as

$$Z_{0,CRLH-TL} = Z_{0,LH-TL} = Z_{0,RH-TL}.$$ (2-13)

According to equation (2-12) the impedance matching conditions can be easily fulfilled for a balanced CRLH-TL over a wide frequency range. For the balanced circuit, plugging equation (2-9) in equation (2-7), leads to:

$$\beta_{CRLH-TL} = \frac{\omega^2 L_R C_L - 1}{\omega \sqrt{L_L C_L}} = \omega \sqrt{L_R C_R} - \frac{1}{\omega \sqrt{L_L C_L}}.$$ (2-14)

From the above equation, it can be noticed that for $\omega > \omega_0$, $\beta_{CRLH-TL} > 0$, while for $\omega > \omega_0$, $\beta_{CRLH-TL} < 0$, where ω_0 is given in (2-10). Using (2-3 a) and (2-5 a), the dispersion equation (2-14) can be written as follows:

$$\beta_{CRLH-TL} = \beta_{RH-TL} - \beta_{LH-TL}.$$ (2-15)

From (2-13) and (2-15), the equivalent circuit for a balanced CRLH-TL can be drawn by connecting in cascade the equivalent circuits for RH-TL and LH-TL, given in Fig. 2-1(a) and Fig. 2-1(b).

On the other hand, to show that the CRLH-TL is a metamaterial, we can use the analogy between Maxwell equations and the dispersion equations in (2-1) to show that the CRLH-TL indeed has negative permittivity and permeability. A homogenous medium, characterized by ε and μ (usually complex values, but real for lossless media),

has the phase constant, β, and the characteristic impedance, Z_0, as:

$$\beta = \omega\sqrt{\varepsilon\mu} \quad \text{and} \quad Z_0 = \sqrt{\frac{\mu}{\varepsilon}}, \tag{2-16}$$

respectively. From (2-16 a,b) and (2-1 a,b), for a lossless medium ($\alpha = 0$), we get:

$$\varepsilon = -j\frac{Y(\omega)}{\omega} \quad \text{and} \quad \mu = -j\frac{Z(\omega)}{\omega}. \tag{2-17}$$

For a homogenous medium which may be modeled by a RH-TL equivalent circuit, inserting the equations (2-2 a,b) in (2-17 a,b), we get:

$$\varepsilon = C_R \quad \text{and} \quad \mu = L_R. \tag{2-18}$$

For a homogenous medium which may be modeled by a LH-TL equivalent circuit, inserting the equations (2-4 a,b) in (2-17 a,b), we get:

$$\varepsilon = -\frac{1}{\omega^2 L_L} \quad \text{and} \quad \mu = -\frac{1}{\omega^2 C_L}. \tag{2-19}$$

Likewise, for a homogenous medium, which may be modeled by a CRLH-TL equivalent circuit, inserting the equations (2-6 a,b) in (2-17 a,b), we get the following result:

$$\varepsilon = C_R - \frac{1}{\omega^2 L_L} \quad \text{and} \quad \mu = L_R - \frac{1}{\omega^2 C_L}. \tag{2-20}$$

By analyzing the equations (2-18 a,b) and (2-19 a,b) it is useful to observe that ε and μ are positive for RH-TL and negative for a LH-TL, respectively. The equations (2-18 a,b)

and (2-19 a,b) are particular cases of the equations (2-20 a,b), for high enough frequencies, respectively for low enough frequencies. The values of ε and μ for CRLH-TL can take either positive or negative values, depending on the frequency. The following conclusions can be drawn by analyzing the relations (2-20 a,b) and (2-8 a,b):

$$\text{if} \quad \omega < \omega_{\Gamma_1}, \quad \text{then} \quad \varepsilon < 0 \quad \text{and} \quad \mu < 0 \tag{2-21}$$

$$\text{if} \quad \omega > \omega_{\Gamma 2}, \quad \text{then} \quad \varepsilon > 0 \quad \text{and} \quad \mu > 0 \tag{2-22}$$

$$\text{if} \quad \omega \in \left(\omega_{\Gamma 1}, \omega_{\Gamma 2} \right), \quad \text{then} \quad \begin{cases} \varepsilon < 0, \quad \mu > 0 \quad \text{if} \quad \dfrac{1}{\omega\sqrt{L_L C_R}} > \dfrac{1}{\omega\sqrt{L_R C_L}} \\[4mm] \varepsilon > 0, \quad \mu < 0 \quad \text{if} \quad \dfrac{1}{\omega\sqrt{L_L C_R}} < \dfrac{1}{\omega\sqrt{L_R C_L}} \end{cases} \tag{2-23}$$

where ω_{Γ_1} and ω_{Γ_2} are given in (2-8 a,b). For the case when the circuit is balanced, if $\omega_{\Gamma_1} = \omega_{\Gamma_2} = \omega_0$ (see equation (2-10)), the following equations can be obtained:

$$\text{if} \quad \omega < \omega_0, \quad \text{then} \quad \varepsilon < 0 \quad \text{and} \quad \mu < 0 \tag{2-24}$$

$$\text{if} \quad \omega > \omega_0, \quad \text{then} \quad \varepsilon > 0 \quad \text{and} \quad \mu > 0. \tag{2-25}$$

The propagation medium is called metamaterial, if $\varepsilon < 0$ and $\mu < 0$, inequalities which are valid for low enough frequencies - see (2-21) for unbalanced CRLH-TL and (2-24) for balanced CRLH-TL.

2.2 Design Principle of MEMS Metamaterial-Based Phase Shifter

In most of MEMS phase shifters [15]-[24], the phase shift is achieved by turning on the capacitive switches, which increases unit-length capacitance, C of the line without significantly affecting its unit-length inductance L. This results in higher phase constant $\beta = \omega\sqrt{LC}$ but lower characteristic impedance $Z = \sqrt{\dfrac{L}{C}}$, where ω is the angular frequency. Therefore, it is challenging for capacitively loaded MEMS phase shifters to maintain impedance match in both through and delayed states.

A phase shifter consisting of cascadable transmission line sections was reported in [25], using five MEMS ohmic switches for each section, its capacitance and inductance can be increased simultaneously at a constant ratio, thereby achieving large phase shift without affecting impedance match. Impressive figures of merit such as 257° of phase shift per dB of insertion loss and greater than 19 dB return loss in both through and delayed states were demonstrated up to 50 GHz. However, the 3-bit phase shifter employs as many as 50 ohmic switches and, despite the high-resistance bias lines used, each switch can consume on the order of 100 mW standby power. This reduces the yield and advantage of the phase shifter.

Following similar method, a compact phase shifter was designed at Lehigh University [5] that employs tightly wrapped slow-wave structure around three closely spaced MEMS capacitive switches. A 90° unit cell was designed with 94° phase shift, 0.27 dB insertion loss, and > 20 dB return loss at 25.75 GHz. The corresponding figures of merits were 350°/dB and 120°/mm. However, the phase shifter circuit was bulky and dispersive.

2.2.1   Low-dispersion MEMS Phase Shifter

Fig. 2-5 shows the layout and equivalent circuit of the low-dispersion MEMS phase shifter basic cell, which employs a coplanar slow-wave structure with defected ground and comprises two single-pole-single-throw (SPST) MEMS capacitive switches in series and parallel configurations, respectively, to switch between right-handed (low-pass) and left-handed (high-pass) states for the specified phase shift. The stationary electrode of the switches is covered by a thin layer of dielectric, so that when the membrane or movable electrode is pulled in to contact the stationary electrode, a high-resistance high-capacitance contact is made. The stationary electrodes of the center switch have a gap in the middle, which allows more design freedom through the switchable series capacitance C_s.

The circuit is a CRLH circuit (band-stop filter) that is sandwiched between two
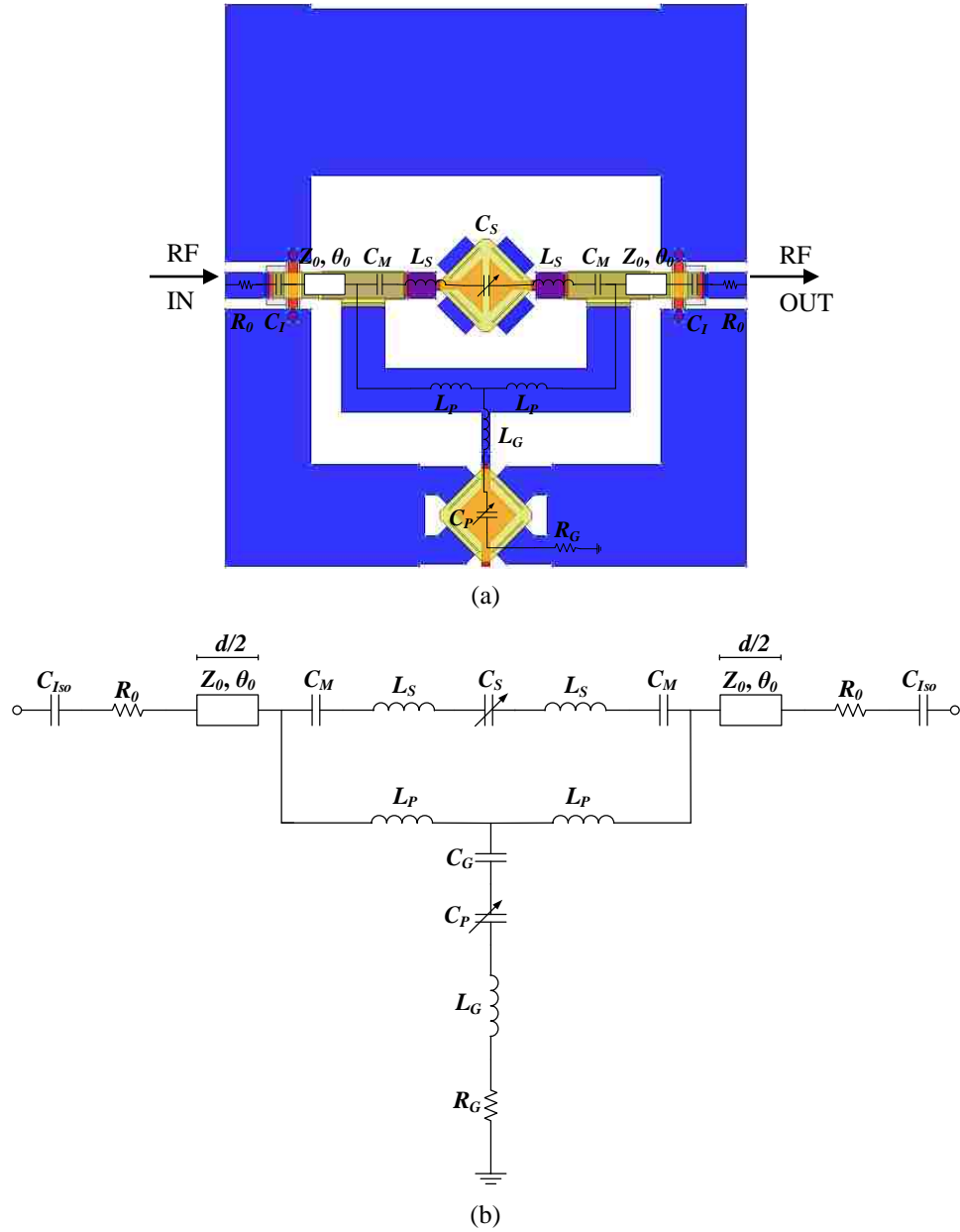
Fig. 2-5 (a) Layout and (b) equivalent circuit of the present low dispersion phase-shifter unit cell.

high-impedance transmission lines and isolation capacitors. When the series switch is

actuated, C_S is large, most of the RF signal passes directly under the movable electrode of

the series switch, while a small fraction of the signal detours along the shunt inductors of

L_P. This adds some slow-wave characteristic to the through state and limits the phase

shift between through and delayed states. To solve the limited phase shift problem, two

fixed metal-isolator-metal (MIM) capacitors of C_M are added to increase the phase shift.

In the delayed state, the center switch is unactuated, C_S is small and the trough path has

high impedance. In this case, most of the RF signal passes along the longest path around

shunt inductors of L_P for a phase shift with respect to that of the through state.

The design principle of the above-described phase shifter is best understood through

the equivalent circuit shown in Fig. 2-5(b). The equivalent circuit contains a lumped

bridged-T [26] section sandwiched between two distributed sections. The distributed

sections have fixed impedance to account for the access lines and other microstrip

sections with characteristic impedance Z_0, propagation constant γ_0, and physical length

$d/2$. The line and switch losses are lumped into a series resistance R_0 and a parallel

resistance R_G. The parallel capacitor C_P accounts for the capacitance between the

movable and stationary electrode, as well as the fringing capacitance between the

movable electrode and the surrounding ground plane of the slow-wave structure. L_S

accounts for the series inductance of the lumped section including the discontinuity at the

39

adjoining distributed sections. The fixed MIM capacitors of C_M and C_G are for matching

and tuning, respectively. L_P accounts for the inductance of slow-wave section while L_G

represents the inductance of shunt switch movable electrode as well as the discontinuity

at the adjoining distributed sections between shunt switch and slow-wave section. Fixed

MIM capacitors of C_{Iso} are responsible for not only the DC isolation between neighboring

basic cells but also impedance match.

By simultaneously solving for the propagation constant and input impedance of the

equivalent circuit, the optimum phase shift and impedance match can be derived. The

unit cell in Fig. 2-5(b) can be conveniently modeled by cascading the transmission

matrices T_T, T_U and T_I for the lumped, distributed and isolation sections, respectively.

Without assuming low frequency or low loss [27] :

$$T = \begin{bmatrix} A & B \\ C & D \end{bmatrix} = T_I . T_U . T_T . T_U . T_I$$

$$T_I = \begin{bmatrix} A_I & B_I \\ C_I & D_I \end{bmatrix} = \begin{bmatrix} 1 & Z_I \\ 0 & 1 \end{bmatrix}$$

$$T_U = \begin{bmatrix} A_U & B_U \\ C_U & D_U \end{bmatrix} = \begin{bmatrix} \cosh \gamma_0 \dfrac{d}{2} & Z_0 \sinh \gamma_0 \dfrac{d}{2} \\ Y_0 \sinh \gamma_0 \dfrac{d}{2} & \cosh \gamma_0 \dfrac{d}{2} \end{bmatrix} \tag{2-26}$$

$$T_T = \begin{bmatrix} A_T & B_T \\ C_T & D_T \end{bmatrix} = \begin{bmatrix} 1 + \dfrac{Z_{LP}Z_S}{Z_{LP}^2 + 2Z_{LP}Z_G + Z_S Z_G} & \dfrac{Z_{LP}Z_S}{2Z_{LP} + Z_S}\left(2 + \dfrac{Z_{LP}Z_S}{Z_{LP}^2 + 2Z_{LP}Z_G + Z_S Z_G} \right) \\ \dfrac{2Z_{LP} + Z_S}{Z_{LP}^2 + 2Z_{LP}Z_G + Z_S Z_G} & 1 + \dfrac{Z_{LP}Z_S}{Z_{LP}^2 + 2Z_{LP}Z_G + Z_S Z_G} \end{bmatrix},$$

where Z_S, Z_{LP} and Z_G are the bridged-T section series impedance, slow-wave section

inductors impedance and shunt switch impedance, respectively, and $Y_0 = \dfrac{1}{Z_0}$ is the

unloaded line admittance, and Z_I is the isolation impedance.

$$\begin{cases} Z_G = R_G + j\omega L_G + \dfrac{1}{j\omega C_P} + \dfrac{1}{j\omega C_G} \\[2mm] Z_S = 2\,j\omega L_S + \dfrac{1}{j\omega C_S} + \dfrac{2}{j\omega C_M} \\[2mm] Z_{LP} = j\omega L_P \\[2mm] Z_I = R_0 + \dfrac{1}{j\omega C_{Iso}}. \end{cases} \qquad (2\text{-}27)$$

The eigenvalues of the basic-cell matrix can be solved by taking advantage of the

symmetry $(A = D)$ and reciprocity $(AD - BC = 1)$ of the unit cell:

$$\gamma d = \pm \cosh^{-1} A = \pm \cosh^{-1}\left(M \cosh \gamma_0 d + N \sinh \gamma_0 d + O\right) \qquad (2\text{-}28)$$

where,

$$\begin{cases} M = A_T + B_T \dfrac{Z_I}{2Z_0^2} + C_T \dfrac{Z_I}{2}, \qquad N = A_T \dfrac{Z_I}{Z_0} + B_T \dfrac{1}{2Z_0} + C_T \dfrac{Z_0}{2} \\[3mm] O = -B_T \dfrac{Z_I}{2Z_0^2} + C_T \dfrac{Z_I}{2}. \end{cases} \qquad (2\text{-}29)$$

Similarly, the input impedance of the unit cell can be derived as:

$$Z_{IN} = \pm\sqrt{\dfrac{B}{C}} = \pm\sqrt{\dfrac{P \cosh \gamma_0 d + Q \sinh \gamma_0 d + R}{S \cosh \gamma_0 d + T \sinh \gamma_0 d + U}} \qquad (2\text{-}30)$$

where,

41

$$\begin{cases} P = 2A_T Z_I + \left(\dfrac{B_T}{2Z_0^2} + \dfrac{C_T}{2} \right)\left(Z_I^2 + Z_0^2 \right), \qquad Q = \dfrac{A_T}{Z_0}\left(Z_I^2 + Z_0^2 \right) + B_T \dfrac{Z_I}{Z_0} + C_T Z_0 Z_I \\[4mm] R = \left(-\dfrac{B_T}{2Z_0^2} + \dfrac{C_T}{2} \right)\left(Z_I^2 - Z_0^2 \right), \qquad S = \left(\dfrac{B_T}{2Z_0^2} + \dfrac{C_T}{2} \right) \\[4mm] T = \dfrac{A_T}{Z_0}, \qquad U = -\dfrac{B_T}{2Z_0^2} + \dfrac{C_T}{2}. \end{cases} \qquad (2\text{-}31)$$

The resonance frequency at which the circuit changes the state from low-pass to high-pass or right-handed to left-handed can be obtained as:

$$F_{0\_through} = \frac{1}{2\pi}\sqrt{\frac{C_M + 2C_S}{2C_M C_S \left(L_S + L_P \right)}}, \qquad (2\text{-}32)$$

$$F_{0\_delayed} = \frac{1}{2\pi} min\left\{ \sqrt{\frac{C_M + 2C_S}{2C_M C_S \left(L_S + L_P \right)}}, -\frac{R_P}{2L_G} \pm \frac{1}{2L_G}\sqrt{\frac{R_P^2 C_P C_G - 4L_G\left(C_P + C_G \right)}{C_P C_G}} \right\} \quad (2\text{-}33)$$

Basic phase shifter unit cells can then be designed by equating (2-30) to 50Ω and allowing the difference between through and delayed states of (2-28) to be constant across the frequencies of interest. Table 2-1 lists the equivalent circuit parameters of the basic cells shown in Fig. 2-5(b) for a flat phase response in the frequency range of 24-28 GHz. Note that 180° and 90° basic cells require synchronous actuation of MEMS switches while 45° and 22.5° unit cells require asynchronous actuation of MEMS switches to switch between through and delayed states.

Fig. 2-6(a) and Fig. 2-6(b) show the difference between the negative solutions of

Table 2-1　　Unit-Cell Equivalent-Circuit Parameter Values

Symbol	22.5°		45°		90°		180°	
	Through	Delayed	Through	Delayed	Through	Delayed	Through	Delayed
C_I (fF)	850		1110		250		340	
R_0 (Ω)	1.6		1.4		0.6		0.6	
Z_0 (Ω)	48		47		44		54	
θ_0 (°)	57@25 GHz		61@25 GHz		44@25 GHz		30@25 GHz	
C_M (fF)	---		---		1150		300	
L_S (pH)	62		62		90		90	
C_S (fF)	300	16	300	14	295	11	305	16
L_P (pH)	75		115		115		205	
C_P (fF)	51	1150	50	1150	1110	101	1100	120
C_T (fF)	39		67		---		---	
L_G (pH)	165		280		190		55	
R_G (Ω)	1.2		0.9		1.4		0.9	

(2-28) for through and delayed states, as functions of frequency over wide frequency ranges and that of the frequencies of interest, respectively. Plugging the equivalent circuit parameters into (2-32) leads to the through-state notch frequencies at 20.5, 17.8, 15.5, 17.5 GHz for 180°, 90°, 45° and 22.5° unit cells, respectively. According to (2-32), part of RF signal detours along slow-wave structure, L_P, which causes the dispersion between through and delayed states. This can be improved by using different switches with different on/off capacitance ratios which then reduce the reliability.

Fig. 2-6(c) and Fig. 2-6(d) show the real part of the positive solutions of (2-30),
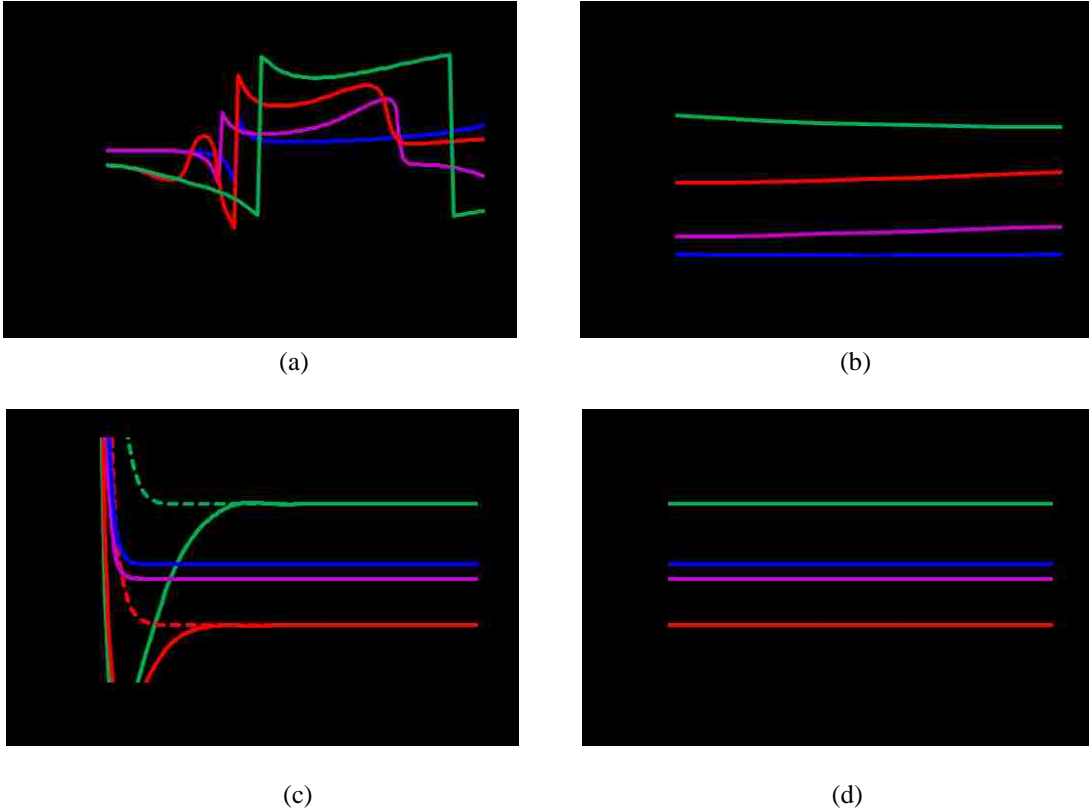
Fig. 2-6   Imaginary part of propagation constant difference between through and delayed state over (a) wide frequency range, (b) frequencies of interest. Real part of input impedance over (c) wide frequency range, and (d) frequencies of interest. Solid and dashed lines indicate through and delayed states, respectively.

over wide band of frequencies and that for the frequencies of interest, respectively. As it can be seen the impedance for the through and delayed states remain the same for each basic unit cell across the frequencies of interest but it changes from one basic cell to the other. If we want to keep perfect impedance match for each basic unit cell while having the constant phase, we should use different switches with different on/off ratios for each

44

cell. Considering that the MEMS switches will be monolithically fabricated on the design, this can reduce the yield and reliability. So, we decided to use the same kind of switches in the present basic unit cells.

The only variables in the equivalent circuit of Fig. 2-5(b) are the two MEMS switches capacitances of C_S and C_P. It is usually difficult to control the unactuated-state capacitance due to process tolerances such as residual stress. The actuated-state capacitance of the switches can be easily influenced by not only the process tolerances but also the applied DC bias voltage. In order to estimate the impact of the MEMS capacitance tolerances on the designed phase shifter unit cells, we performed the sensitivity analysis. Circuit sensitivity can be mathematically obtained as:

$$S_x^y = \frac{x}{y} \frac{\partial y}{\partial x} \tag{2-34}$$

where S is the sensitivity, x is the changing variable and y is the circuit characteristic that we wish to evaluate as x is changed. Applying (2-33) to (2-28) and (2-30), allows us to quantify the sensitivity of the propagation constant or ultimately insertion phase and input impedance of each basic cell as a function of frequency when either C_S or C_P is variable.

Fig. 2-7 shows that the through-state insertion phase in general is sensitive to series
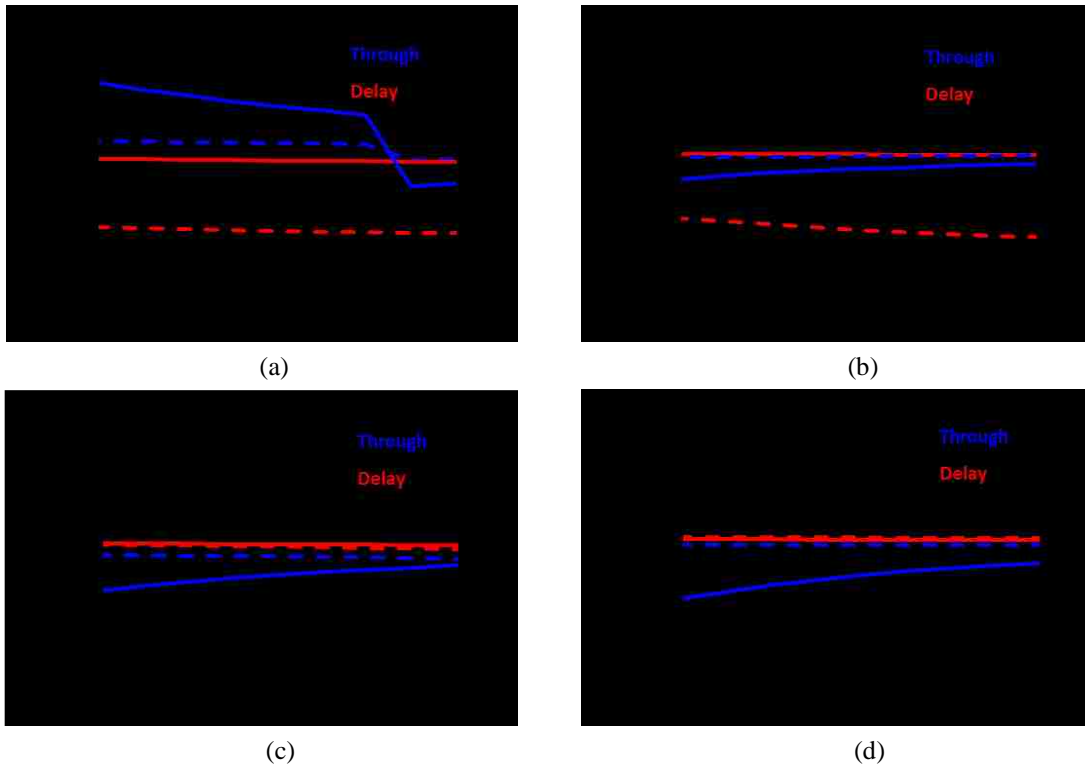
Fig. 2-7   Sensitivity of imaginary part of the propagation constant of (a) 180°, (b) 90°, (c) 45°, (d) 22.5° unit cells to MEMS switch capacitance. Sensitivity related to series switch capacitance, C_S (solid line) and that of related to shunt switch capacitance, C_P (dashed line).

switch capacitance, C_S, while the delayed-state insertion phase is sensitive to the shunt switch capacitance, C_P. The same is also true for input impedance according to Fig. 2-8. The reason for this sensitivity is clear because in through state most of RF signal paths through the series capacitance while in the delayed state most of the RF signal detours around the slow-wave structure which is loaded by shunt capacitance. Also, insertion phase is more sensitive than impedance to the capacitance change which is mainly

46
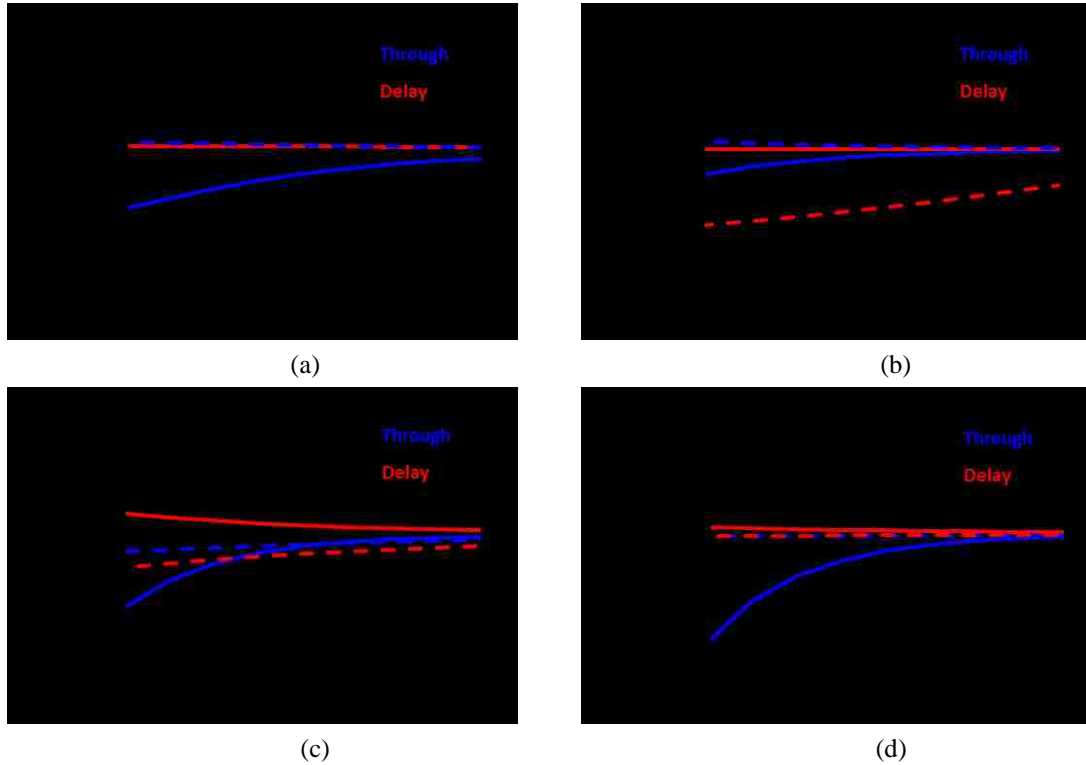
Fig. 2-8　Sensitivity of real part of input impedance of (a) 180°, (b) 90°, (c) 45°, (d) 22.5° unit cells related to MEMS switch capacitance. Sensitivity related to series switch capacitance, C_S (solid line) and that of related to shunt switch capacitance, C_P (dashed line).

because of the fact that the impedance is largely influenced by the distributed section while the phase is related mainly to the compact section. Further, the 180° unit cell is very sensitive to the change of MEMS switch capacitance mainly because of the fact that it is designed in the ultimate limit of the circuit and it has greater phase dispersion. This problem can be fixed by using switches with different on/off ratio.

47

2.3 Implementation

2.3.1   Temperature Independent Switch Design (Geometrical Approach)

MEMtronics' switch technology was used in this project to realize the metamaterial-based phase shifters [28]-[32]. The initial switch had a "figure-8" molybdenum membrane and gold stationery electrode that was covered by silicon dioxide [4], [5]. The fabrication of these MEMS switches produced results that demonstrated significant variation in membrane flatness and actuation voltage due to insufficient residual stress and a sensitivity to stress gradients in the "figure-8" layout of the switch. Part of this shortcoming was because of insufficient numbers of MEMS fabrication runs through the fab that use molybdenum as a mechanical material.

To overcome this obstacle and move forward with the innovative phase shifter designs, we decided to redesign the switch membrane construction and layout to achieve a more repeatable mechanical performance. Material and geometrical approaches were evaluated and it was decided to focus on a geometrical design approach which would provide the desired performance in a robust manner. Geometrical approach utilizes a geometry-based method to design the MEMS membrane such that the resulting switch is
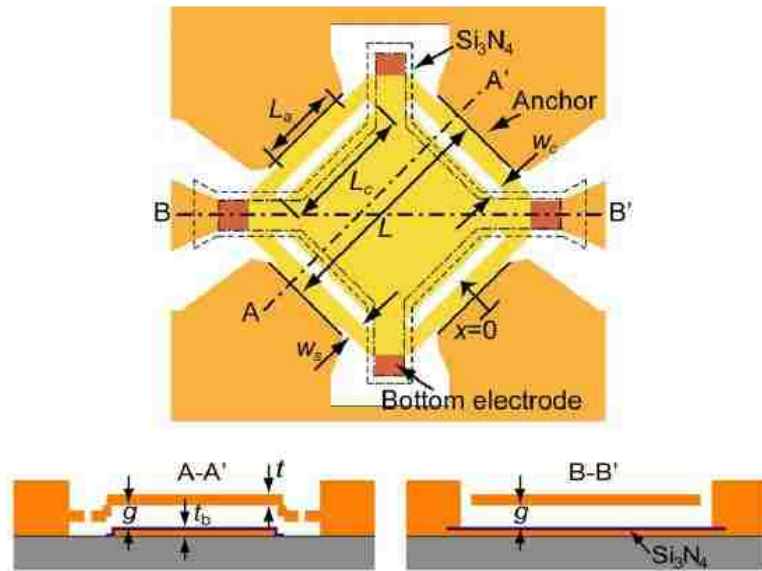
Fig. 2-9 Geometrical design-based approach for achieving temperature stable MEMS membranes [8].

stable over temperature and insensitive to stress gradients. This approach has been well

publicized by Rebeiz [9]-[11].

As shown in Fig. 2-9, the geometry incorporates a square shape, four anchors, and

four slots to decouple film stress and gradients from impacting the actuation voltage of

the switch over temperature. This is achieved by designing a membrane shape which

minimizes the reaction forces from the anchors due to thermal expansion. This technique

was demonstrated with a 8000Å thick gold film, achieving < 50 mV/°C variation in

voltage over the 25°C to 125°C temp range [8]. The geometry of the mechanical beams

created by the slots in the membrane determine the sensitivity (insensitivity) to residual

49

| (a) | (b) |
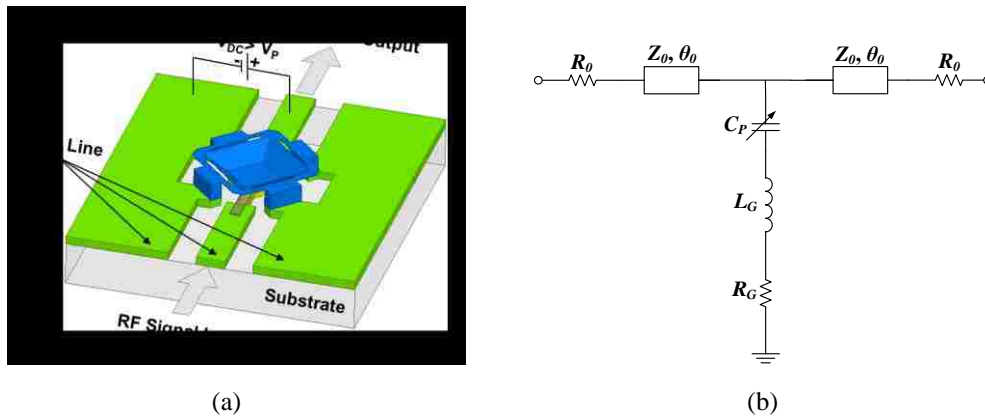
Fig. 2-10   (a) Layout for simulating electrical/RF performance, and (b) equivalent circuit of the temperature independent shunt MEMS switch.

Table 2-2   Layer Information of Temperature Independent Switch

Layer	Material	Thickness (um)
Transmission Line	Copper	3.1
Bottom Electrode	Gold	0.6
Dielectric	Silicon Dioxide	0.3
Airgap	air	2.2
Membrane	Gold	0.8
Substrate	Sapphire	600

stress, stress gradients, and expansion of the film over temperature. An advantage is that

this approach is design-oriented and would not likely require much in the way of new

process development.

Initial electrical models of the switch were constructed using HFSS 3D

electromagnetic simulator to evaluate the RF performance of the switch as shown in Fig.

50

(a)   (b)
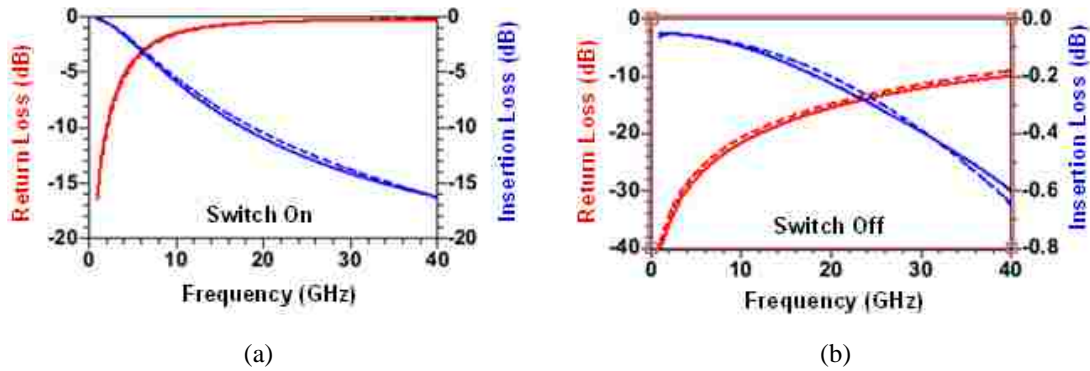
Fig. 2-11   HFSS-simulated (solid) and modeled (dashed) return and insertion losses ($|S_{11}|$ and $|S_{21}|$) of the new switch when switch is (a) on, and (b) off.

Table 2-3   Equivalent-Circuit Parameter Values of the MEMS Switch

Parameter	F_0 (GHz)	Z_0 (Ω)	θ_0 (°)	R_0 (mΩ)	R_G (mΩ)	L_G (pH)	C_{ON} (fF)	C_{OFF} (fF)
Value	25	54	11	300	100	2	1000	66

2-10(a). Table 2-2 lists different layers' information of the temperature independent switch that used in the electromagnetic simulations. The electromagnetic simulation results were modeled by using the equivalent circuit model shown in Fig. 2-10(b) to extract the on/off ratio of the switch. Fig. 2-11 compares the scattering parameters of the electromagnetic-simulated and ADS-modeled switch. Corresponding values of the equivalent circuit parameters are listed in Table 2-3. We can see that the capacitance ratio is greater than 15, however the off capacitance of the switch is a bit higher than the previous design but it is expected that these extra parasitics can be absorbed into the

51
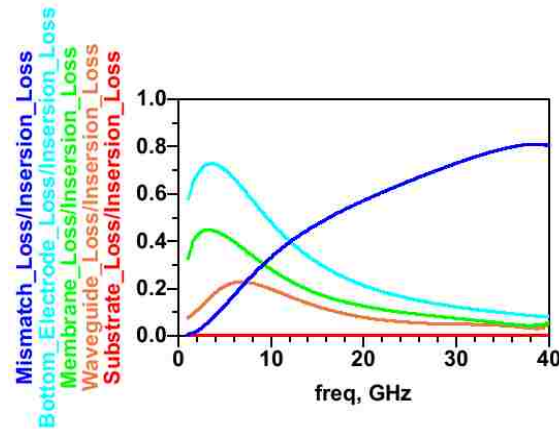
Fig. 2-12   Different loss components of the new switch related to insertion loss in up-state.

Ka-band phase shifter designs.

Fig. 2-12, shows the different loss factors of the switch in the unactuated state. As it

is evident from Fig. 2-12, at lower frequencies up to 13 GHz, material loss especially the

loss associated with bottom electrode is the dominant loss component, while at higher

frequencies beyond 13 GHz, mismatch loss becomes dominant. Since our goal is to use

this switch to design Ka band (24 – 27 GHz) phase shifter, we should optimize the switch

in terms of mismatch loss. The mismatch loss is also related to the off capacitance of the

switch such that smaller off capacitance leads to better matching. This can be resolved by

shrinking the bottom electrode, however it needs to be done by considering lots of other

parameters including, pull-in voltage, on-off ratio, parasitics and actuation contact area.

Furthermore, in the simulations provided so far, we supposed that the membrane is

52
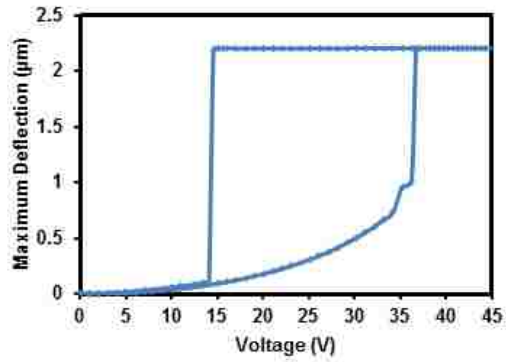
Fig. 2-13 Electromechanical simulation of the maximum deflection of the MEMS shunt switch under different bias voltages.

Table 2-4   Geometry and Mechanical Parameters of the Shunt Switch

Parameter	Value
Membrane Thickness	0.8 μm
Bottom Electrode Thickness	0.6 μm
Air Gap	2.4 μm
Young's Modulus of Gold	57 GPa
Poisson's Ratio of Gold	0.35
Membrane Residual Stress	0 MPa

contacting the stationary electrode flatly resulting in a sharp actuation however this assumption is ideal and not happening in practice.

As part of implementing a new, temperature-independent switch into the MEMS phase shifter, by using Ansys Multiphysics, electromechanical models have been created to verify the published results, and to serve as the basis for making changes and improvements. Table 2-4 lists the parameter values used by the ANSYS Multiphysics
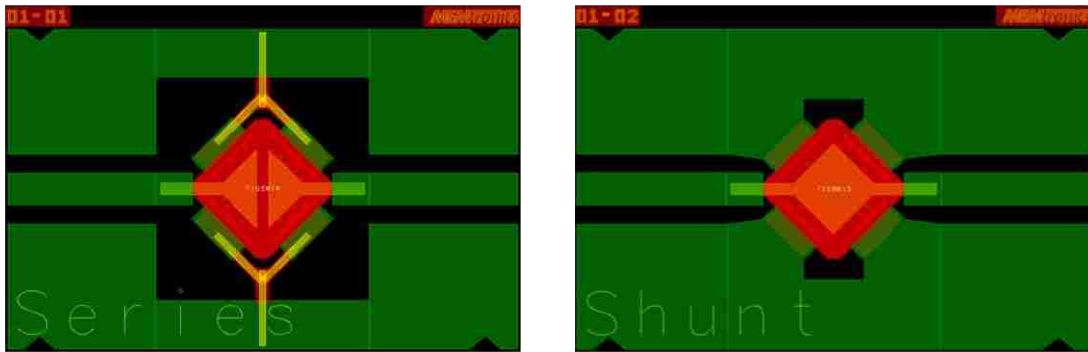
| (a) | (b) |

Fig. 2-14   Details of (a) series and (b) shunt MEMS switches used in each unit cell. The movable electrode of each switch is made of gold and is approximately 165 µm × 165 µm.

electromechanical simulator to have better understanding of the membrane deflection under applied DC voltage which helps us to better optimize the switch. Fig. 2-13 shows the simulated membrane deflection under different bias voltages. The actuation voltage is 36 V while the release voltage is 14 V.

After careful considerations of the requirements for basic phase shifter unit cells as well as DC pull-in voltages, the series and shunt MEMS switches were laid out as shown in Fig. 2-14. It can be seen that the series switch differs from the shunt switch mainly by splitting the stationary electrodes into two halves, which are DC connected but RF isolated unless the movable electrode is pulled in on top of them. This resulted in approximately 25% smaller stationary electrode and 5-V higher actuation voltage (33 V vs. 28 V) than that of the shunt switch. Although this difference in actuation voltage is

54

tolerable as all switches are overdriven at 40 V, the layout of the series switch should be further optimized so that it has the same actuation voltage as the shunt switch.

2.3.2   Layout of Basic Phase Shifter Unit Cell

Following the above-described design approaches, the unit cells were laid out with their equivalent-circuit parameters optimized by using the HFSS 3D finite-element electromagnetic simulator as listed in Table 2-1 in the previous section. The small variations in the switch capacitance, whether in series or shunt configuration and whether actuated or unactuated, for each unit cell is because it includes the parasitic capacitance, which is different for different layout of each unit cell. This underscores the importance of absorbing all parasitics in the present compact design.

(a)   (b)
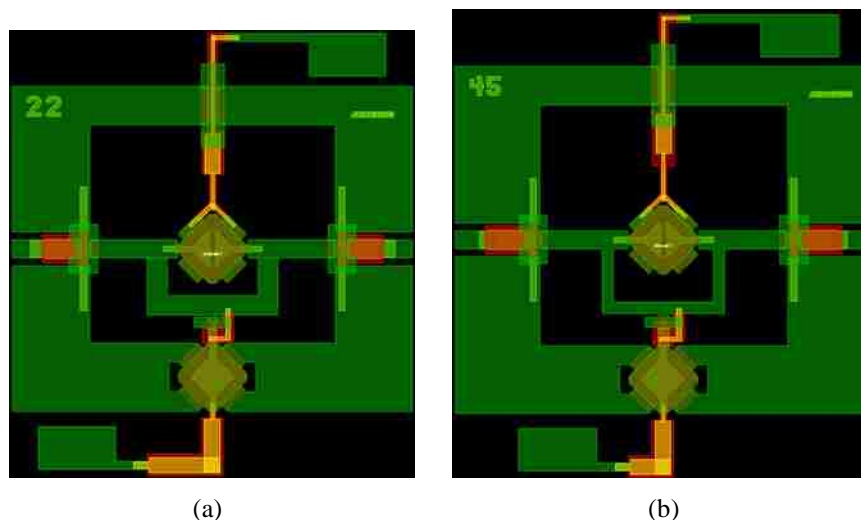
Fig. 2-15   Layout of (a) 22.5°and (b) 45°unit cells with chip sizes of 1.3 mm × 1.4 mm and 1.35 mm × 1.5 mm, respectively.

(a)   (b)
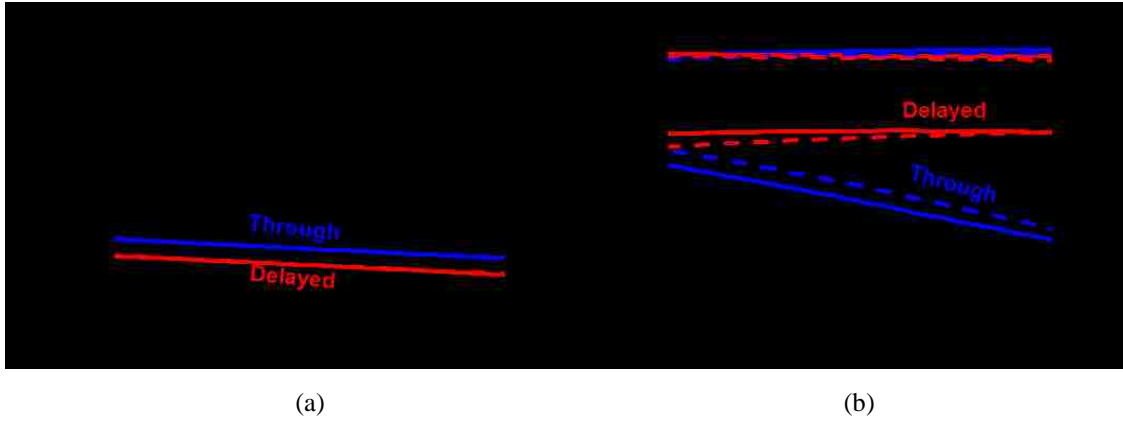
Fig. 2-16   Electromagnetics-simulated (solid) vs. equivalent-circuit-modeled (dashed) (a) insertion phase ($<S_{21}$) and (b) insertion loss ($|S_{21}|$) and return loss ($|S_{11}|$) of the new 22.5° phase-shifter unit cell with square gold switches.

(a)   (b)
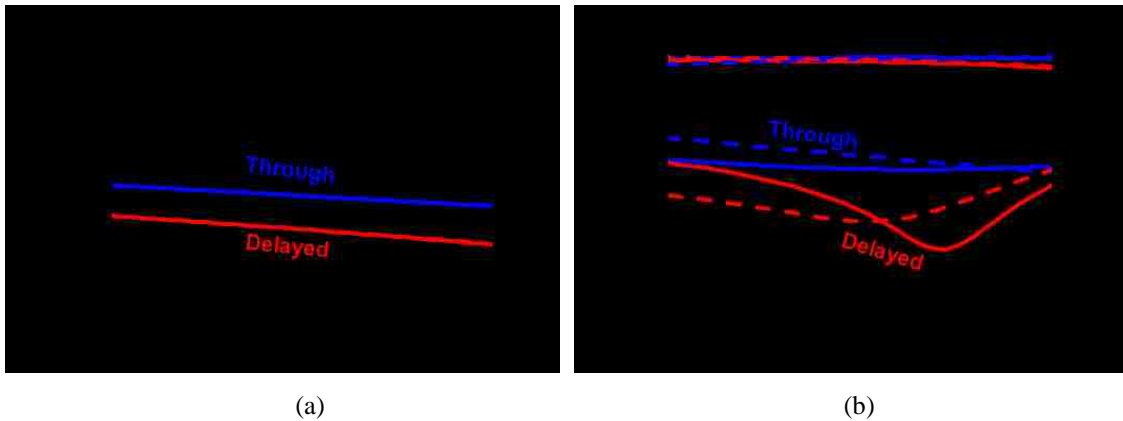
Fig. 2-17   Electromagnetics-simulated (solid) vs. equivalent-circuit-modeled (dashed) (a) insertion phase ($<S_{21}$) and (b) insertion loss ($|S_{21}|$) and return loss ($|S_{11}|$) of the new 45° phase-shifter unit cell with square gold switches.

Fig. 2-15 shows the layouts of 22.5° and 45° unit cells. In these layouts, series switches are actuated while the shunt switches are suspended in the through state, and vice versa in the delayed state. Figure 2-16 and figure 2-17 show the simulated (by HFSS) and modeled (by Agilent ADS) scattering parameters of the 22.5° and 45° unit
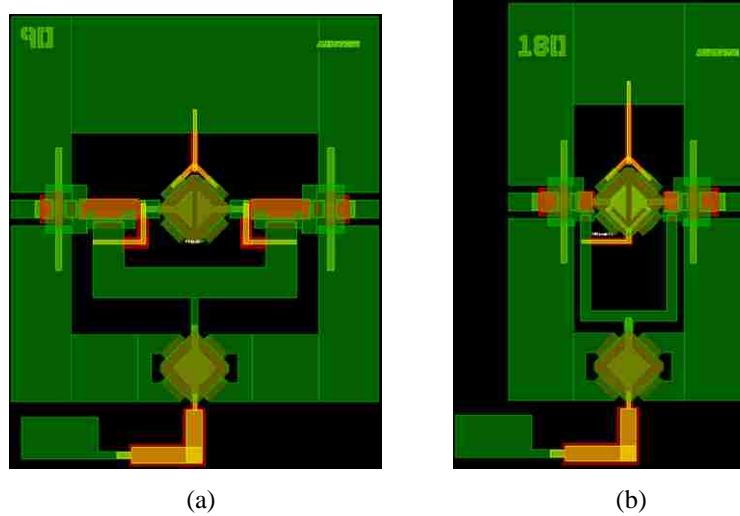
Fig. 2-18   Layout of (a) 90° and (b) 180° unit cells with chip sizes of 1.2 mm × 1.45 mm and 1 mm ×
1.5 mm, respectively.

cells, respectively. The 22.5° unit cell exhibits less than 0.4 dB insertion loss, greater than

15 dB return loss, and 22.5±0.25° phase shift between 24 GHz and 28 GHz. Across the

same frequency band, the 45° unit cell provides 47±5° phase shift with less than 0.5 dB

insertion loss and better than 19 dB return loss. Note that the 45° and 90° unit cells are

designed to have slightly greater phase shift to compensate for smaller phase shift of the

180° unit cell and to reduce the overall root-mean-square phase error of the 3-bit phase

shifter.

Fig. 2-18 shows the layouts of 90° and 180° unit cells, in which series and shunt

switches are simultaneously actuated in the through state, and are both suspended in the

delayed state. Fig. 2-19 and Fig. 2-20 show the simulated (by HFSS) and modeled (by
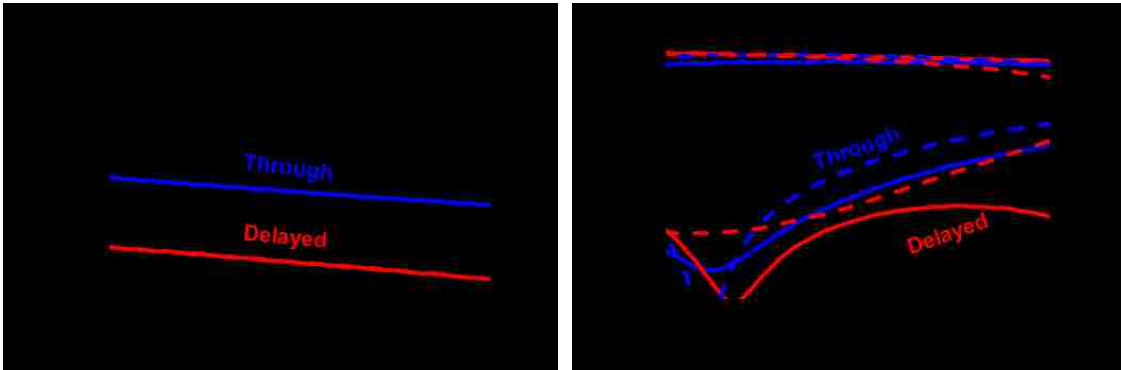
(a)   (b)

Fig. 2-19   Electromagnetics-simulated (solid) vs. equivalent-circuit-modeled (dashed) (a) insertion phase ($<S_{21}$) and (b) insertion loss ($|S_{21}|$) and return loss ($|S_{11}|$) of the new 90° phase-shifter unit cell with square gold switches.
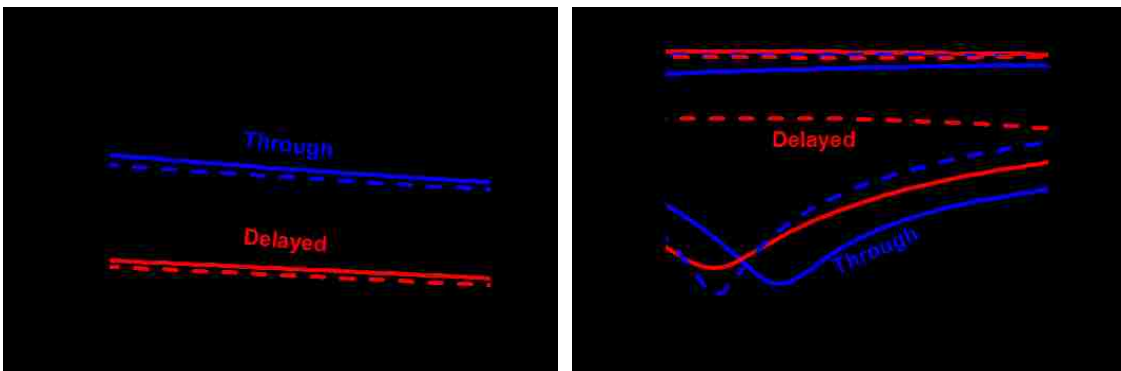
(a)   (b)

Fig. 2-20   Electromagnetics-simulated (solid curves) vs. equivalent-circuit-modeled (dashed curves) (a) insertion phase ($<S_{21}$) and (b) insertion ($|S_{21}|$) and ($|S_{11}|$) return losses of the new 180° phase-shifter unit cell with square switches.

Agilent ADS) scattering parameters of the 90° and 180° unit cells, respectively. The 90°

unit cell exhibits less than 0.5 dB insertion loss, greater than 16 dB return loss, and 98±3°

phase shift between 24 GHz and 28 GHz. Across the same frequency band, the 180°

unit cell provides 172±8° phase shift with less than 1 dB insertion loss, and better than 18

58

dB return loss.

2.3.3   Layout of Multi-bit Phase Shifter

The 90° and 180° unit cells were cascaded into a 2-bit phase shifter then optimized by using HFSS. There were only two ways to cascade these unit cells together: one way with the two cells orientated in same direction; the other way with the second cell flipped upside down as shown in Fig. 2-21. Although simulation showed little difference, the second way of cascading was chosen for the minimizing potential mode coupling between the cells. A 500-µm long 50-Ω coplanar waveguide was inserted between the two unit cells to further reduce any coupling effect and to improve impedance match. The simulated performance of the 2-bit phase shifter across the band of 24−28 GHz at all
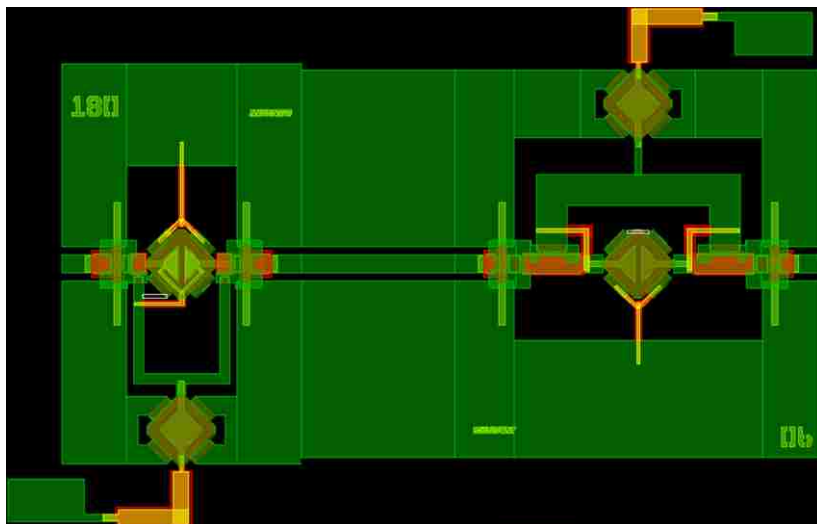
Fig. 2-21   Layout of the 2-bit phase shifter comprising the 180° and 90° unit cells. The chip size is 2.5 mm × 1.6 mm.
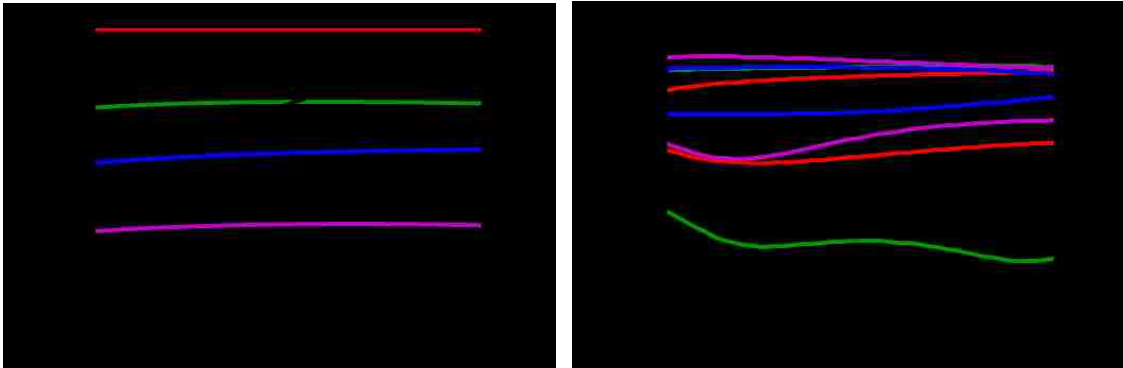
Fig. 2-22   Electromagnetics-simulated (a) phase shift and root-mean-square phase error and (b) insertion/return loss of all eight states of the 2-bit phase shifter.

four phase states is shown in figure 2-22. It can be seen that even in the worst case,   the

root-mean-square phase error is less than 11°, the insertion loss is less than 1.8 dB, and

the return loss is greater than 10 dB.

Following the same cascading approach, 45°, 90° and 180° unit cells were combined

into a 3-bit phase shifter then optimized by using HFSS. Table 2-5 compares the

simulated phase-shifter performance across the band of 24−28 GHz for three

permutations with the 180° unit cell at the beginning, middle and end, respectively. It can

be seen that the permutation with the 180° unit cell at the beginning is the best in terms of

phase error, insertion loss and return loss. This can be explained according to the different

input impedances of basic cells as shown in Fig. 2-6. The layout for this permutation is

shown in Fig. 2-23 and its simulated performance across the band at all eight phase states

Table 2-5   Effect of Unit-Cell Cascading Order

Order	180/90/45		90/180/45		90/45/180	
	In	Out	In	Out	In	Out
RMS Phase Error (°)	< 9	< 9	< 11	< 11	< 10	< 10
Insertion Loss (dB)	< 1.7	< 1.7	< 2.5	< 2.5	< 1.9	<1. 9
Return Loss (dB)	> 13	> 12	> 6	> 7	> 10	> 10
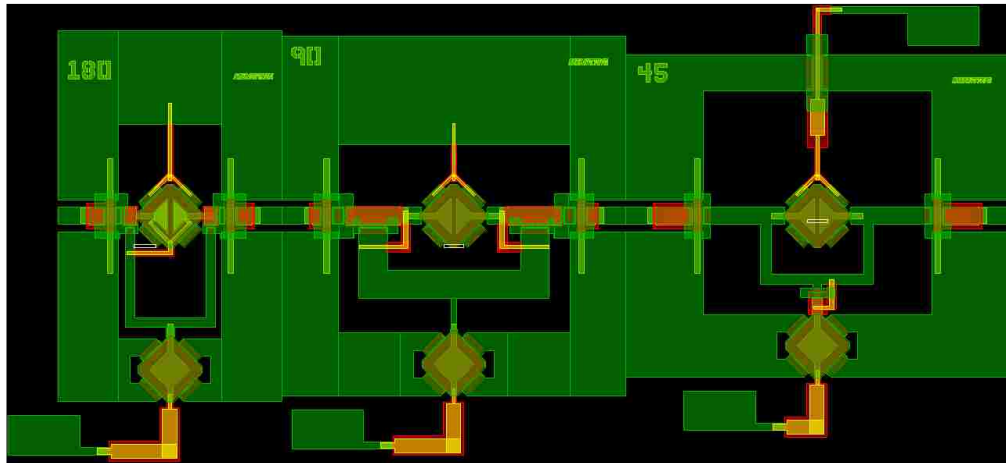
Fig. 2-23   Layout of the present 3-bit phase shifter comprising three unit cells with 180°, 90° and 45° phase shifts, respectively. The overall chip size is 3.3 mm × 1.6 mm.

is shown in 2-24 and Fig. 2-25. Although the layout is not symmetrical, the performance is essentially reciprocal. For example, the input/output return losses are very similar to each other, which implies that there is little difference in reversing the cascading order.

As shown in Fig. 2-24, even in the worst case across the band of 24−28 GHz, the root-mean-square phase error of the present 3-bit phase shifter is less than 9°, the insertion loss is less than 1.7 dB, and the return loss is greater than 13 dB. This suggests a
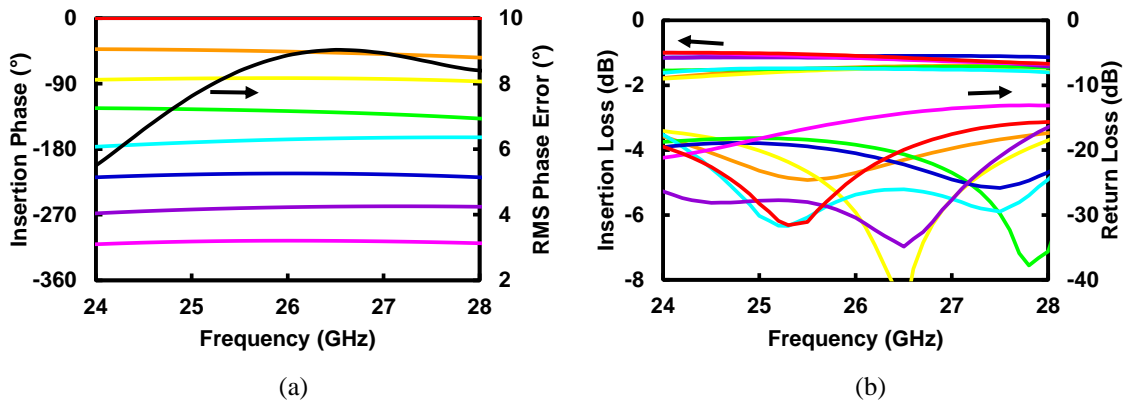
Fig. 2-24   Electromagnetics-simulated (a) phase shift and root-mean-square phase error and (b) insertion/return loss of all eight states of the input port of the 3-bit phase shifter.
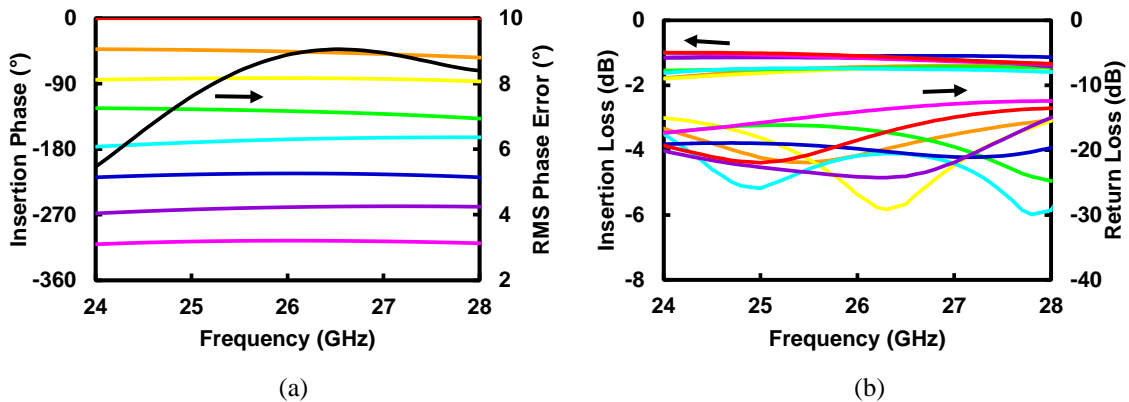
Fig. 2-25   Electromagnetics-simulated (a) phase shift and root-mean-square phase error and (b) insertion/return loss of all eight states of the output port of the 3-bit phase shifter.

significant improvement over the previous designs listed in Table 2-6 except that the

return loss needs to be improved by approximately 2 dB. The above results were all based

on simulation.

The performance of the 3-bit phase shifter as shown in figure 4 was evaluated for its

sensitivity to the variation in MEMS switch capacitance, considering the relatively

Table 2-6 Comparison of Low-Dispersion MEMS Phase Shifters

Year	2008	2014	2015	2016
Bandwidth (GHz)	8−12	12−14	22−26	24−28
Number of Bits	5	3	3	3
RMS Phase Error (°)	< 10	< 27	< 21	< 9
Insertion Loss (dB)	< 9	< 3	< 2	< 2
Return Loss (dB)	> 15	> 7	> 15	> 13
No. of Switches	20	14	8	6
Size (mm^2)	9	18	9	5
Reference	[2]	[4]	[5]	Present

Table 2-7 Sensitivity To MEMS Capacitance Variation

C_S (fF)	225	265	300	345	375
C_P (fF)	825	935	1100	1265	1375
RMS Phase Error (°)	< 12	< 6	< 9	< 13	< 14
Insertion Loss (dB)	< 2.4	< 2	< 1.7	< 1.7	< 1.7
Return Loss (dB)	> 11	> 13	> 13	> 13	> 14

immature manufacture of RF MEMS. Table 2-7 shows that the present design is rather

robust even when the actuated MEMS switch capacitances vary by ±15%.

63

References

[1] R. V. Garver, "Broad-band diode phase shifters," *IEEE Trans. Microw. Theory Techn.*, vol. 20, no. 5, pp. 314−323, May 1972.

[2] M. A. Morton and J. Papapolymerou, "A packaged MEMS-based 5-bit X-Band high-pass/low-pass phase shifter," *IEEE Trans. Microwave Theory Tech.*, vol. 56, no. 9, pp. 2025−2031, Sep. 2008.

[3] C. Palego, Z. Peng, J. C. M. Hwang, D. Scarbrough, D. I. Forehand, and C. L. Goldsmith, "Compact Ka-band phase shifters using MEMS capacitive switches," in *Proc. European Microwave Conf.,* Sep. 2009, pp. 1864−1867.

[4] C. Palego, Y. Ning, V. Gholizadeh, X. Luo, J. C. M. Hwang, and C. L. Goldsmith, "Compact, wideband, low-dispersion, metamaterial-based MEMS phase shifters," in *IEEE MTT-S Int. Microwave Symp. Dig.*, Tampa Bay, Florida, Jun. 2014, pp. 1−4.

[5] V. Gholizadeh, Y. Ning, X. Luo, C. Palego, J. C. M. Hwang, and C. L. Goldsmith, "Improved Compact, Wideband, Low-dispersion, Metamaterial-based MEMS Phase Shifters," in *IEEE Int. Wireless Symp. Dig.*, Shenzhen, China, Mar. 2015, pp. 1−4.

[6] V. Gholizadeh, M. J. Asadi, Y. Ning, C. Palego, J. C. M. Hwang, D. Scarbrough, and C. L. Goldsmith, "Low-dispersion metamaterial-based phase shifters with reduced size and number of MEMS switches," in IEEE MTT-S Int. Wireless Symp. Dig., Shanghai, China, Mar. 2016, pp. 1−4.

[7] V. Gholizadeh, M. J. Asadi, Y. Ning, C. Palego, J. C. M. Hwang, D. Scarbrough, and C. L. Goldsmith, "Low-dispersion 180° phase shifter using two synchronized MEMS switches," in *Lester Eastman Conference,* Bethlehem, PA, 2016, pp. 35−37.

[8] H. Nieminen, V. Ermolov, S. Silanto, K. Nybergh, and T. Ryhanen, "Design of a temperature-stable RF MEM capacitor," *J. Microelectromech. Syst.*, vol. 13, no. 5, pp. 705–714, Oct. 2004.

[9] I. Reines, B. Pillans, and G. Rebeiz, "Performance of Temperature Stable RF MEMS Switches under High RF Power Conditions, *IEEE 2010 Intl Microwave Symp Dig*, pp. 292-295, June 2010.

[10] R. Mahameed and G. Rebeiz, "Power Handling of Temperature-Stable Thin-Film MEMS Capacitive Switches," *40th European Microwave Conf*, pp. 97–100, 2010.

[11] R. Mahameed and G. Rebeiz, "RF MEMS Capacitive Switches for Wide Temperature Range Applications Using a Standard Thin-Film Process*," IEEE Trans Microwave Theory Tech*, vol. 59, no. 7, pp. 1746–1752, July 2011.

[12] A. Lai, T. Itoh, and C. Caloz, "Composite right/left-handed transmission line metamaterials," *IEEE Microw. Mag.,* vol. 5, no. 3, pp. 34–50, Sep. 2004.

[13] C. Caloz and T. Itoh, "Electromagnetic Metamaterials: Transmission Line Theory Microwave Applications," *Hoboken, NJ: Wiley - IEEE Press*, 2005.

[14] G. Eleftheriades and K. Balmain, "Negative-Refraction Metamaterials: Fundamental Principles Applications," *Hoboken, NJ: Wiley - IEEE Press*, 2005.

[15] Y. Liu, A. Borgioli, A. S. Nagra, and R. A. York, "K-band 3-bit low-loss distributed MEMS phase shifter," *IEEE Microwave Guided Wave Lett.*, vol. 10, no. 10, pp. 415–417, 2000.

[16] J. S. Hayden and G. M. Rebeiz, "A low-loss Ka-band distributed MEMS 2-bit phase shifter using metal-air-metal capacitors," *IEEE MTT-S Int. Microwave Symp. Dig.*, 2002, pp. 337–340.

[17] G. L. Tan, R. E. Mihailovich, J. B. Hacker, J. F. DeNatale, and G. M. Rebeiz, "A 2-bit miniature X-band MEMS phase shifter," *IEEE Microwave Compon. Lett.*, vol. 13, no. 4, pp. 146–148, 2003.

[18] J. S. Hayden and G. M. Rebeiz, "Very low-loss distributed X-band and Ka-band MEMS phase shifters using etal–air–metal capacitors," *IEEE Trans. Microwave Theory Tech.*, vol. 51, no. 1, pp. 309–314, 2003.

[19] J. J. Hung, L. Dussopt, and G. M. Rebeiz, "A low-loss distributed 2-Bit W-band MEMS phase shifter," in *Proc. 33rd European Microwave Conf.*, Munich, 2003, pp. 983–986.

[20] J. J. Hung, L. Dussopt, and G. M. Rebeiz, "Distributed 2- and 3-bit W-band MEMS phase shifters on glass substrates," *IEEE Trans. Microwave Theory Tech.*, vol. 52, no. 2, pp. 600–606, 2004.

[21] M. Unlu, S. Demir, and T. Akin, "A 15–40 GHz frequency reconfigurable RF MEMS phase shifter," *IEEE Trans. Microwave Theory Tech.*, vol. 61, no. 8, pp. 2865–2877, 2013.

[22] A. Chakraborty, B. Gupta, and B. K. Sarkar, "Design, fabrication and characterization of miniature RF MEMS switched capacitor based phase shifter," *Microelectron. J.*, vol. 45, no. 8, pp. 1093–1102, 2014.

[23] A. S. Abdellatif, A. A. Aziz, R. R. Mansour, and S. S. Naeini, "Low-loss compact MEMS phase shifter for phased array antennas," *Electron. Lett.*, vol. 51, no. 15, pp. 1142–1144, 2015.

[24] A. Chakraborty and B. Gupta, "Development of compact 180° phase shifters based on MEMS technology," *Sens. Actuators A: Phys.*, vol. 247, pp. 187–198, 15 Aug. 2016.

[25] B. Lakshminarayanan and T. M. Weller, "Design and modeling of a 4-bit slow-wave phase shifter," *IEEE Trans. Microwave Theory Techniques*, vol. 54, no. 1, pp. 120−127, Jan. 2006.

[26] Sulzer, Peter G. "A note on a bridged-T network," *Proceedings of the IRE,* vol. 39, no. 7, pp. 819−821,1951.

[27] C. Palego, Z. Peng, J.C.M Hwang, D. Scarbrough, C.L. Goldsmith, ″Novel Ka-band phase shifters using MEMS capacitive switches,″ *2010 IEEE 11th Annual Wireless and Microwave Technology Conference (WAMICON),* 12–13 April 2010.

[28] C. Goldsmith, et al, ″Micromechanical microwave switching,″ US Patent 5 619 061, Apr. 8, 1997.

[29] C. Palego, J. Deng, Z. Peng, S. Halder, J.C. Hwang, D.I. Forehand, D. Scarbrough, C.L. Goldsmith, I. Johnston, S.K. Sampath, and A. Datta, "Robustness of RF MEMS capacitive switches with molybdenum membranes," *IEEE Trans. on Microwave Theory and Techniques*, vol. 57, no. 12, pp. 3262–3269, 2009.

[30] C. Goldsmith, D. Forehand, D. Scarbrough, I. Johnston, S. Sampath, A. Datta, Z. Peng, C. Palego, and J.C.M. Hwang, "Performance of molybdenum as a mechanical membrane for RF MEMS switches", in *IEEE MTT-S International Microwave Symposium Digest,* pp. 1229–1232, June 2009.

[31] C. L. Goldsmith, O. H. Auciello, J. A. Carlisle, S. Sampath, A. V. Sumant, R.W. Carpick, J. Hwang, D. C. Mancini, C. Gudeman, "RF-MEMS capacitive switches with high reliability", US Patent 8525185, 2013.

[32] C. Palego and F. Solazzi and S. Halder and J. C. M. Hwang and P. Farinelli and R. Sorrentino and A. Faes and V. Mulloni and B. Margesin, "Effect of substrate on temperature range and power capacity of RF MEMS capacitive switches," in 40th *European Microwave Conf.*, Paris, 2010, pp. 505–508.

Chapter 3 Characterization

3.1 MEMS Switch

Each basic phase shifter unit cell uses two SPST capacitive MEMS switches in shunt and series configurations. Fig. 3-1 shows the details of the series and shunt MEMS switches that was fabricated on a 600-µm thick sapphire substrate. The switches have a squared-shaped movable electrode with four long and narrow slits along each side, so that the movable electrode is anchored only at the four corners in the north, south, east and west directions of Fig. 3-1(a) and Fig. 3-1(b). This not only makes the MEMS switch more compact, but also increases its tolerance of variations in temperature and residual stress [33].

(a)	(b)
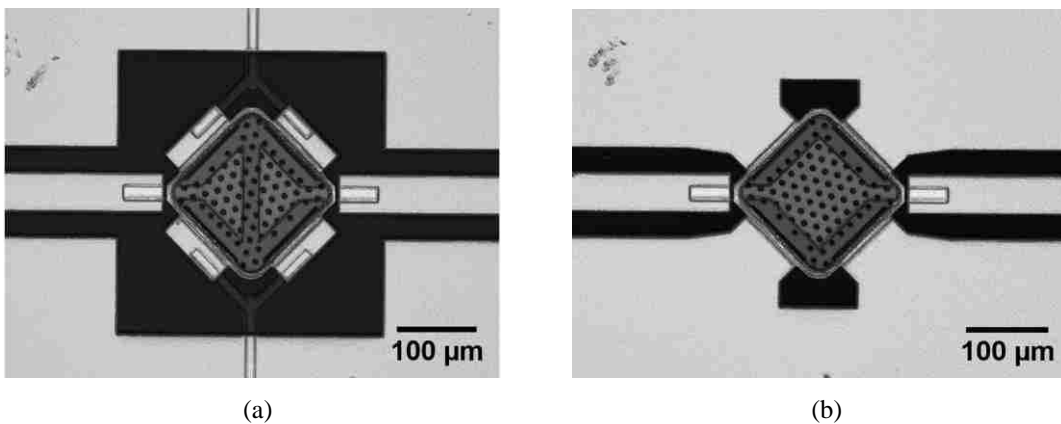
Fig. 3-1   Details of (a) series and (b) shunt MEMS switches used in the present phase shifters. The movable electrode of each switch is approximately 165 µm × 165 µm.

The series switch differs from the shunt switch mainly by splitting the stationary electrode into two halves, which are DC connected but RF isolated unless the movable electrode is pulled in on top of the stationary electrode. The gap between two stationary electrodes is 20 µm in the present design. This resulted in approximately 25% smaller stationary electrode and 3 V higher pull-in voltage (36 V vs. 33 V) than that of the shunt switch as shown in Fig. 3-5. However, since the switches can tolerate more than their pull-in voltage, we will overdrive them by applying 40 V DC bias. The movable electrode is DC connected to the ground lines in the north and south through large resistors that are open in RF frequencies.

To verify the difference in the actuation voltage and locate working switches across the wafer, capacitance vs. voltage (C-V) measurements were performed on many switches. The actuation voltage was found to vary between 20 V and 60 V across the wafer. Fig. 3-2 shows the C-V characteristics of typical series and shunt switch. It can be seen that the actuation voltage of a typical shunt and series switch is almost 33 V and 36 V, respectively. It can also be seen that the actuated capacitance is 720 fF for shunt switch and 75 fF for series switch, which is significantly lower than the simulated value of 1100 fF and 300 fF, respectively for shunt and series switches. On the other hand, the
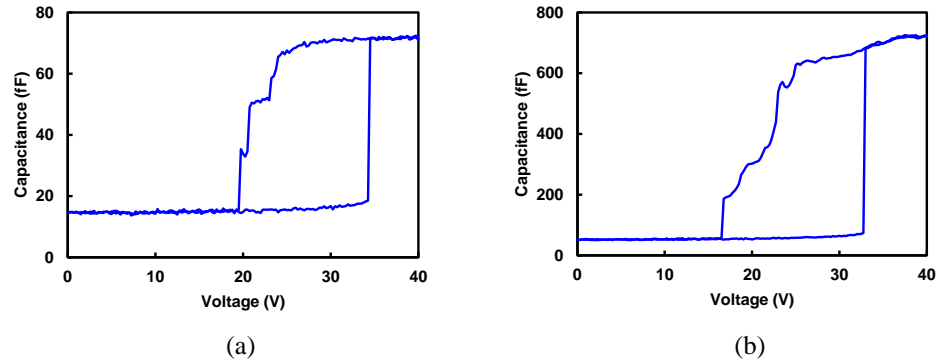
Fig. 3-2   C-V characteristics of (a) series and (b) shunt MEMS switches.

unactuated capacitance is 51 fF for shunt switch and 15 fF for the series switch which

agrees well with the simulated value. The actuated capacitance of shunt switch is 35%

and that of series switch is 75% smaller than the desired values. This will negatively

influence the performance of the phase shifter, especially in terms of insertion loss as

shown in next section.

3.1.1   Basic Phase Shifter Unit Cells

3.1.2   Asynchronous Unit cells

In these unit cells, series switches are actuated while the shunt switches are

suspended in the through state, and vice versa in the delayed state [34]-[36]. Since the

switches were not flatly actuated under the biased voltage and thus there was 35% less

shunt capacitance and 75% less series capacitance, there was a slight frequency shift and

<center>(a)   (b)</center>
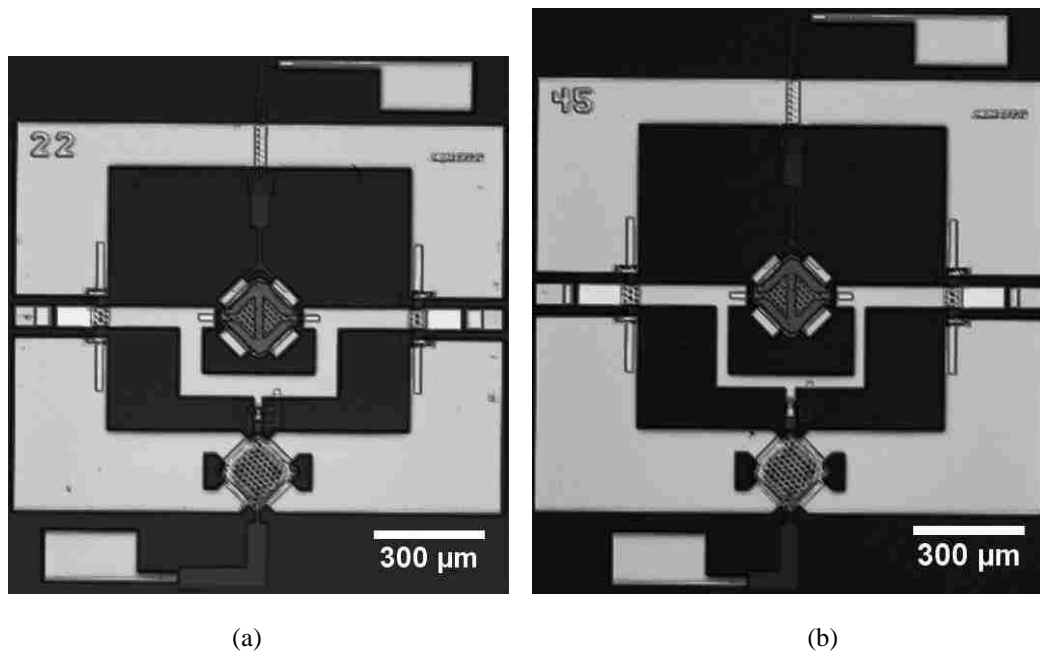
Fig. 3-3　Micrograph of (a) 22.5° and (b) 45° unit cells with chip sizes of 1.3 mm × 1.4 mm and 1.35 mm × 1.5 mm, respectively.

<center>(a)   (b)</center>

Fig. 3-4　Measured (a) insertion phase and (b) insertion/return losses of the 22.5° basic cell with real MEMS switches.

extra insertion loss associated with each phase shifter basic cell.

Fig. 3-3 shows the micrograph of 22.5° and 45° unit cells. Fig. 3-4 and Fig. 3-5

show the measured scattering parameters of the 22.5° and 45° unit cells, respectively. The

<center>71</center>

Fig. 3-5   Measured (a) insertion phase and (b) insertion/return losses of the 45° basic cell with real MEMS switches.

22.5° basic cell exhibits less than 1 dB insertion loss, greater than 14 dB return loss, and 29±1° phase shift between 26 GHz and 30 GHz. Note that the insertion loss in this case is more than the design values by a factor of 2 and there is a 2 GHz frequency shift toward upper band. The main reason for this discrepancy is the intrinsic loss of the switches as well as their non-flat membrane which reduces their actuated-state capacitance.

The 45° basic cell provides 55±2° phase shift with less than 1.5 dB insertion loss and better than 13 dB return loss between 23 GHz and 27 GHz. Note that the insertion loss in this case is more than the design values by a factor of 3 due to intrinsic loss of the switches as well as their non-flat membrane. Further, there is a 1 GHz frequency shift toward lower band.

3.1.3 Synchronous Unit cells

In these unit cells the series and shunt switches actuate simultaneously to change the unit cell from the delayed state to the through state [35]-[37]. Fig. 3-6 shows the micrograph of 90° and 180° unit cells. Fig. 3-7 and Fig. 3-8 show the measured scattering parameters of 90° and 180° unit cells, respectively. The 90° basic cell exhibits less than 1.9 dB insertion loss, greater than 16 dB return loss, and 103±3° phase shift between 23 GHz and 27 GHz. The measured insertion loss is 4 times higher than the simulated value and there is a 1 GHz frequency shift toward lower band.

(a)   (b)
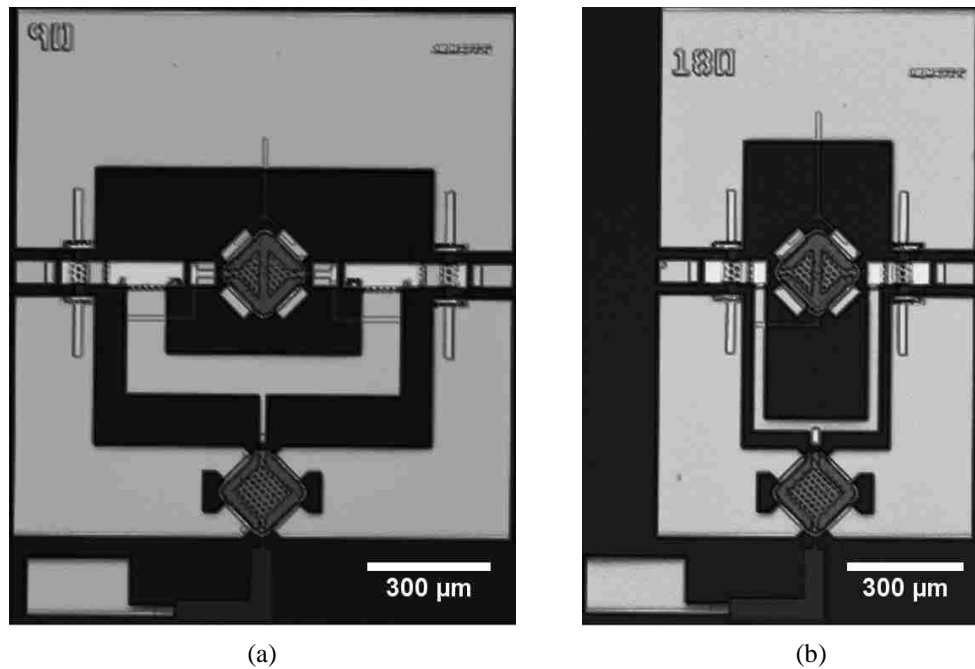
Fig. 3-6   Photograph of (a) 90° and (b) 180° unit cells with chip sizes of 1.2 mm × 1.5 mm and 1 mm × 1.5 mm, respectively.

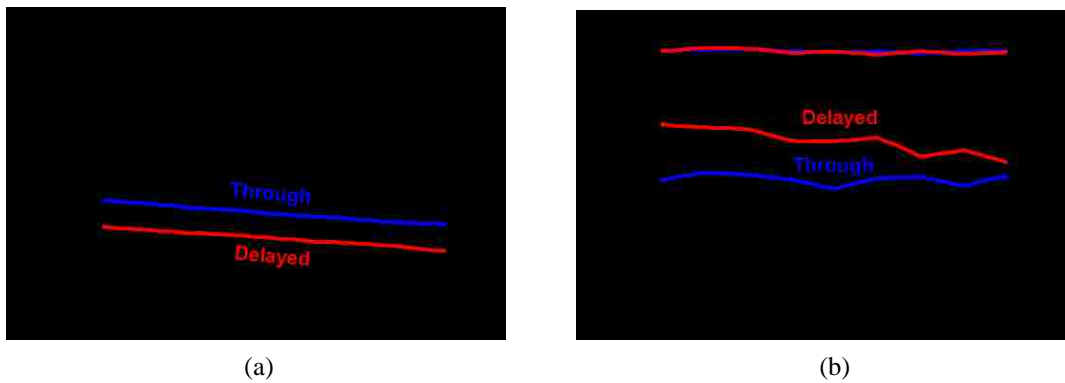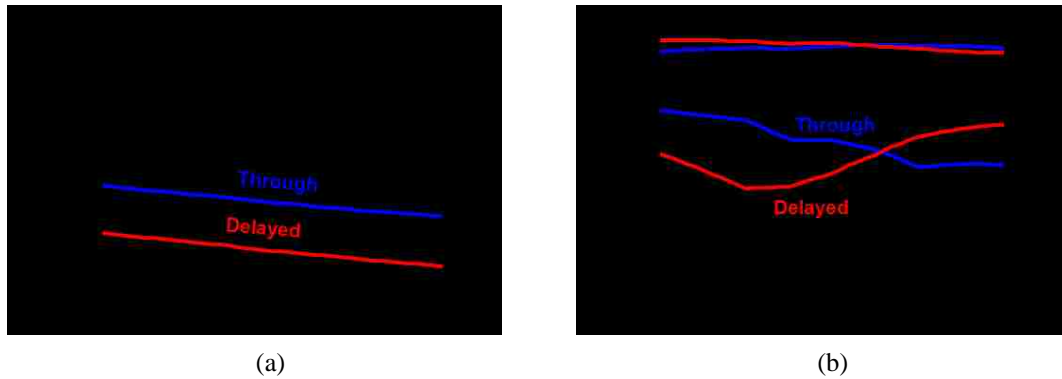(a)   (b)
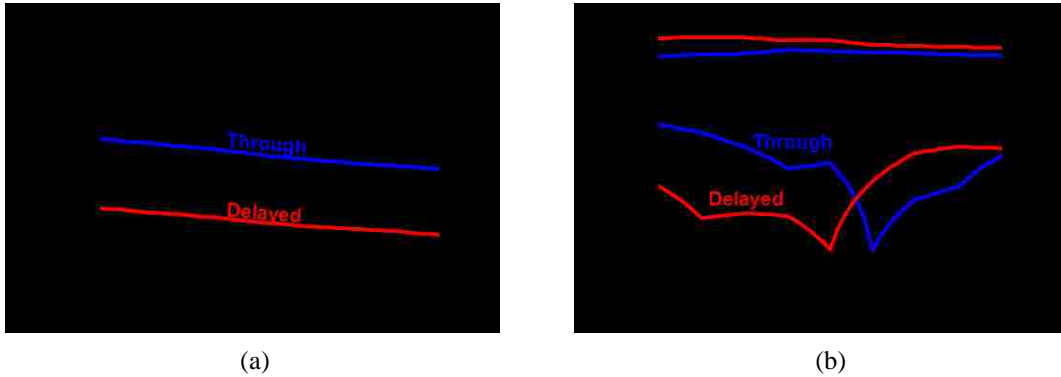
Fig. 3-7   Measured (a) insertion phase and (b) insertion/return losses of the 90° basic cell with real MEMS switches.

(a)   (b)
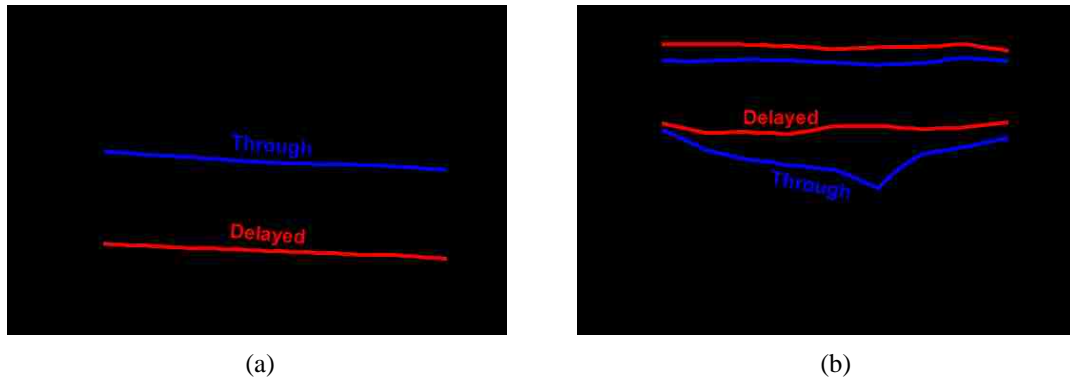
Fig. 3-8   Measured (a) insertion phase and (b) insertion/return losses of the 180° basic cell with real MEMS switches.

180° basic cell provides 172±4° phase shift with less than 2.4 dB insertion loss, and better than 15 dB return loss between 29 GHz and 33 GHz. The measured insertion loss is 2.5 times higher than the simulated value. Further, there is a 5 GHz frequency shift toward higher band.

3.2 Multi-bit Phase Shifters

Individual basic cells were then cascaded to form 2-bit and 3-bit digital phase

shifters with 90° and 45° phase resolution, respectively.

3.2.1   2-bit Phase Shifter

Fig. 3-9 shows the micrograph of the fabricated 2-bit phase shifter that is comprised

of a flipped 90° basic cell, a 500-µm long 50-Ω coplanar waveguide (CPW), and a 180°

basic cell. The measured performance of the 2-bit phase shifter across the band of 26–31

GHz at all four phase states is shown in Fig. 3-10. Note that there is a 2 GHz frequency

shift toward higher band due to imperfect actuation of the switches. The 90° and 180°

basic cells actuate according to Table 3-1 to switch between different phase shifter states.
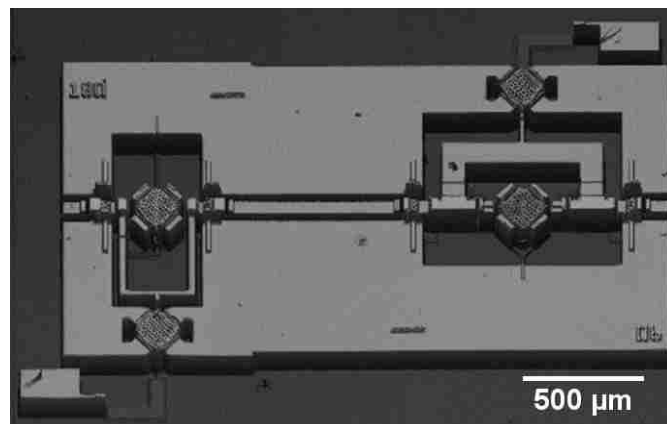
Fig. 3-9   Micrograph of the 2-bit phase shifter comprising 90° and 180° basic cells. The chip size is 2.5 mm × 1.6 mm.

<center>(a)</center>

<center>(b)</center>
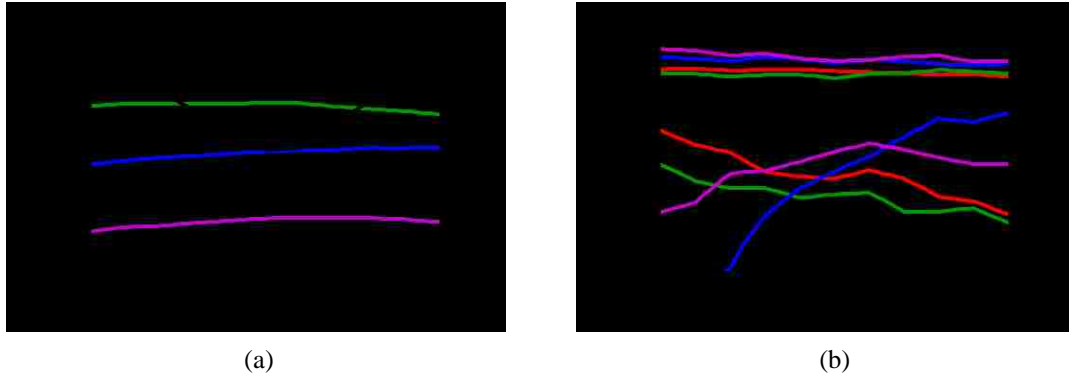
Fig. 3-10　Measured (a) insertion phase, (b) insertion and return losses of all four phase states of the input port of the 2-bit phase shifter across the band of 26−31 GHz.

<center>Table 3-1　Two-bit Phase Shifter States</center>

State	Phase Shift (°)	180° Basic Cell	90° Basic Cell
1	0	Through	Through
2	90	Through	Delayed
3	180	Delayed	Through
4	270	Delayed	Delayed

As shown in Fig. 3-10, even in the worst case across the band of 26.5−30.5 GHz, the root-mean-square phase error of the present 2-bit phase shifter is less than 17°, the insertion loss is less than 4 dB, and the return loss is greater than 8 dB. Note that the insertion loss of 2-bit phase shifter equals to the sum of insertion loss of the 90° and the 180° basic cells. This suggests that by utilizing switches with smaller insertion loss and better actuation, (i.e. less than 0.4 dB), this phase shifter can indeed perform with less than 1.6 dB insertion loss as initially designed by using HFSS in previous chapter.

3.2.2   3-bit Phase Shifter

Fig. 3-11 shows the micrograph of the fabricated 3-bit phase shifter that is comprised of a 45°, a 90° and a 180° basic cell without any extra 50-Ω line between them. There is no alteration in the unit cells as discussed in previous chapter. The phase shifter occupies less than 5 mm^2 on the sapphire substrate. As it can be seen from the 3D micrograph in Fig. 3-11, the membranes of the switches are not flatly suspended which along with their non-flat actuation harms the phase shifter performance.

Since there are 4 DC bias pads, a homemade DC probe-card was assembled as shown in Fig. 3-12 to bias all the unit cells. The measured performance of the 3-bit phase shifter across the band of 24–27 GHz at all eight phase states is detailed in Fig. 3-13. The 45°, 90° and 180° unit cells actuate according to Table 3-2 to switch between different
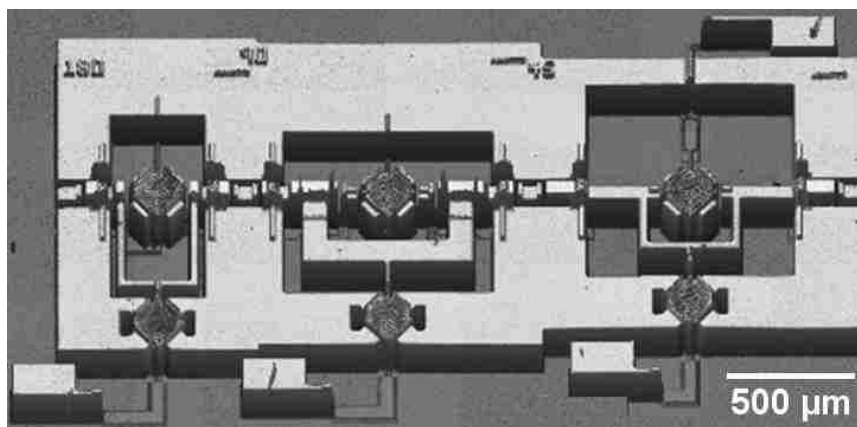
Fig. 3-11   Micrograph of the 3-bit phase shifter comprising 45°, 90° and 180° basic cells. The chip size is 3.3 mm × 1.6 mm.

Fig. 3-12   Test setup for charactering the 3-bit phase shifter using a homemade DC probe-card.

Table 3-2   Three-bit Phase Shifter States

State	Phase Shift (°)	180° Unit Cell	90° Unit Cell	45° Unit Cell
1	0	Through	Through	Through
2	45	Through	Through	Delayed
3	90	Through	Delayed	Through
4	135	Through	Delayed	Delayed
5	180	Delayed	Through	Through
6	225	Delayed	Through	Delayed
7	270	Delayed	Delayed	Through
8	315	Delayed	Delayed	Delayed

phase states.

As shown in Fig. 3-13, even in the worst case across the band of 24−27 GHz, the

root-mean-square phase error of the present 3-bit phase shifter is less than 55°, the

78
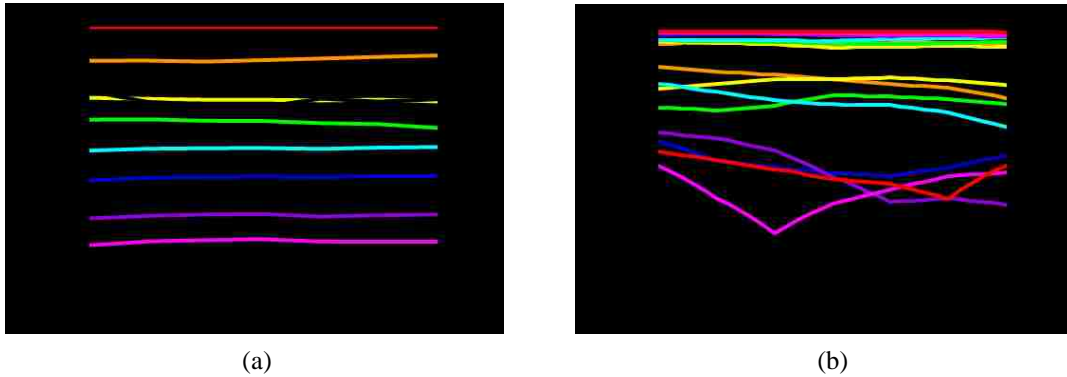
Fig. 3-13   Measured (a) insertion phase and (b) insertion/return loss of all eight states of the 3-bit phase shifter.

insertion loss is less than 7.5 dB, and the return loss is greater than 5 dB. The main reason

for the much-worse-than-expected insertion loss is the frequency shift of 180° basic cell

which causes four initial states to exhibit large insertion loss. On the other hand, the main

reason for the worse-than-expected phase flatness is the over 130° phase shift the 90°

basic cell due to non-flat switch membranes. The average insertion loss over the eight

states across the frequency band of 24–27 GHz is less than 4.6 dB and the average return

loss over the eight states in the same frequency band is greater than 11.2 dB. The

root-mean-square phase error of the 3-bit phase shifter can be reduced to below 18° as

shown in Fig. 3-14 by redefining the phase states according to Table 3-3. Also note that

the insertion loss is 1.3 times higher than the sum of the losses of individual cells mainly

because of membrane buckling in un-actuated states. This can be seen from Fig. 3-11.

79
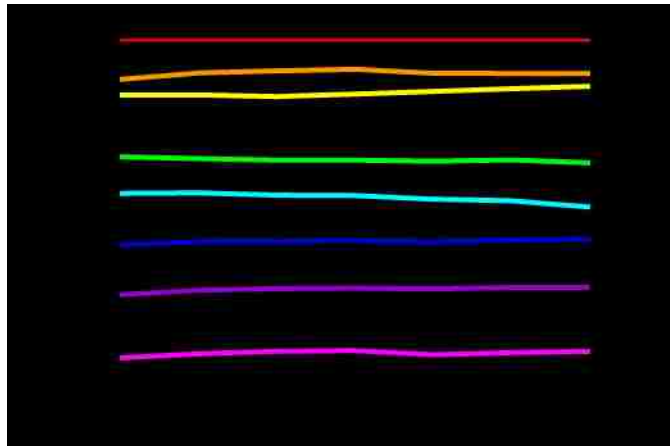
Fig. 3-14　Measured insertion phase of all redefined eight states of the input port of the present 3-bit phase shifter across the band of 24−27 GHz

Table 3-3　Redefined Three-bit Phase Shifter States

State	Phase Shift (°)	180° Unit Cell	90° Unit Cell	45° Unit Cell
1	0	Through	Through	Through
2	45	Delayed	Delayed	Delayed
3	90	Through	Through	Delayed
4	135	Through	Delayed	Through
5	180	Through	Delayed	Delayed
6	225	Delayed	Through	Through
7	270	Delayed	Through	Delayed
8	315	Delayed	Delayed	Through

References

[33] H. Nieminen, V. Ermolov, S. Silanto, K. Nybergh, and T. Ryhanen, "Design of a temperature-stable RF MEM capacitor," *J. Microelectromech. Syst.*, vol. 13, no. 5, pp. 705–714, Oct. 2004.

[34] C. Palego, Y. Ning, V. Gholizadeh, X. Luo, J. C. M. Hwang, and C. L. Goldsmith, "Compact, wideband, low-dispersion, metamaterial-based MEMS phase shifters," in *IEEE MTT-S Int. Microwave Symp. Dig.*, Tampa Bay, Florida, Jun. 2014, pp. 1–4.

[35] V. Gholizadeh, Y. Ning, X. Luo, C. Palego, J. C. M. Hwang, and C. L. Goldsmith, "Improved Compact, Wideband, Low-dispersion, Metamaterial-based MEMS Phase Shifters," in *IEEE Int. Wireless Symp. Dig.*, Shenzhen, China, Mar. 2015, pp. 1–4.

[36] V. Gholizadeh, M. J. Asadi, Y. Ning, C. Palego, J. C. M. Hwang, D. Scarbrough, and C. L. Goldsmith, "Low-dispersion metamaterial-based phase shifters with reduced size and number of MEMS switches," in *IEEE MTT-S Int. Wireless Symp. Dig*., Shanghai, China, Mar. 2016, pp. 1−4.

[37] V. Gholizadeh, M. J. Asadi, Y. Ning, C. Palego, J. C. M. Hwang, D. Scarbrough, and C. L. Goldsmith, "Low-dispersion 180° phase shifter using two synchronized MEMS switches," in *IEEE Lester Eastman Conference*, Bethlehem, PA, 2016, pp. 35–37.

Chapter 4 Experimental Validation of Design and Discussion

4.1 Ohmic Loss Characterization

Ohmic loss was first characterized to validate the design and discover the underlying reason for the discrepancy between the electromagnetic simulations and measurements. Fabrication process related parameters such as thickness of different layers, their conductivity, substrate permittivity and its loss tangent were characterized. Shunt MEMS switch, as the main building block of the present design was selected to evaluate the overall loss.

Dektak benchtop stylus profilometer and Bruker's 3D optical microscope were used to measure the thickness of different layers as shown in Fig. 4-1 [1], [2]. The measurement results confirm that several modifications have been made over fabrication process which deviates the MEMS switch performance from the expectations. Table 4-1 compares the measured information for different layers with those of used in the design of temperature independent switch. It can be seen that the dielectric is thicker than expected. The actuated state capacitance, C_{on}, is defined as [3]:
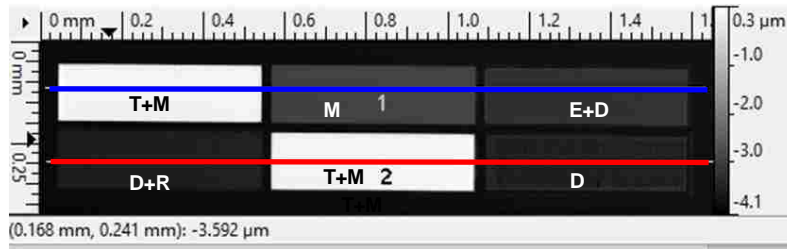
(a)
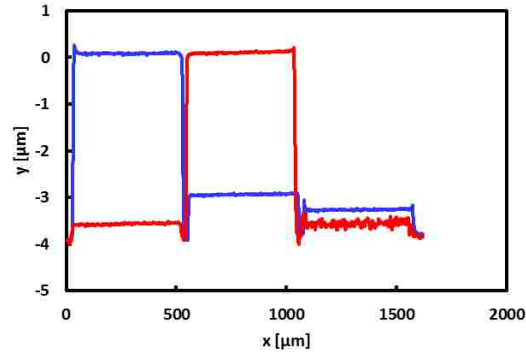
(b)

Fig. 4-1   (a) Micrograph of test structures that is made of different deposited layers, and (b) the optical profile along the horizontal lines shown in (a).

Table 4-1   Layer Information of Temperature Independent Switch

Layer	Designed		Fabricated	
	Material	Thickness (um)	Material	Thickness (um)
T-Line	Copper	3.1	Gold	3.9
Electrode	Gold	0.6	Gold	0.6
Dielectric	SiO$_2$	0.3	SiO$_2$	0.35
Airgap	air	2.2	air	2.15
Membrane	Gold	0.8	Gold	1
Substrate	Sapphire	600	Sapphire	600

$$C_{on} = \frac{\varepsilon_0 A}{2}\left(\frac{1}{d_1 + \dfrac{d_2}{\varepsilon_r}} + \frac{\varepsilon_r}{d_2} \right),$$ (4-1)

83

where A is the capacitive area of the membrane, d_1 is the amplitude of the roughness, d_2

is the dielectric thickness, and ε_r is the relative dielectric constant of the dielectric

layer. If we ignore the roughness we can see that 17% thicker dielectric layer can

decrease the C_{on} by 16%. The isolation can be defined as:

$$S_{21} = \frac{1}{1 + j\omega C_{on} Z_0 / 2},$$
(4-2)

which shows that the 16% less C_{on} translates into 17% less isolation. Table 4-1 shows

that the airgap is smaller than the designed value. The unactuated state capacitance, C_{off},

of the MEMS switch is defined as:

$$C_{off} = \frac{\varepsilon_0 A}{g + \dfrac{d_2}{\varepsilon_r}},$$
(4-3)

where g is the airgap. Plugging the numbers from Table 4-1 shows that the C_{off} is

increasing by 2-3%. The insertion loss of the switch with smaller than 13 dB return loss

can be defined as:

$$Loss = \omega^2 \, C_{off}^2 \, R_s \, Z_0,$$
(4-4)

where R_s is the series resistance of the membrane. Therefore from (4-4) a 2%-3% smaller

airgap leads to 4%-6% extra insertion loss. Furthermore, the pull-in voltage of the switch

is defined as:

84

$$V_p = \sqrt{\frac{8k}{27\varepsilon_0 A}g^3} \,, \qquad\qquad (4\text{-}5)$$

where k is the spring constant of the membrane. From Table 4-1, 2%-3% smaller airgap

can decrease the pull-in voltage by 3%-5%. The transmission line is made of gold instead

of copper which increases the ohmic loss because the conductivity of gold is 30% smaller

than copper. Furthermore, as we show later in this chapter, the membrane is not flat and

is buckled down in most of cases which causes even more obvious increase in insertion

loss, especially for the phase shifters.

Conductivity of each layer was measured by measuring the resistance of two test

structures for each layer, one with 40 squares and the other with 280 squares and then

deembed to cancel the contact resistance and cable effects. Agilent 4156C precision

semiconductor parameter analyzer along with RF Cascade ACP probes were used to

reduce the contact resistance and improve the accuracy [4], [5]. This is diefferent than the

4-probe measurement method that usually uses DC probes [6]. Fig. 4-2 shows the typical

layout of the test structures to measure the conductivity of each layer. Fig. 4-3 shows the

conductivity of deposited layers for stationary electrode, membrane and transmission

line. The conductivity of each layer then can be calculated by using their thicknesses
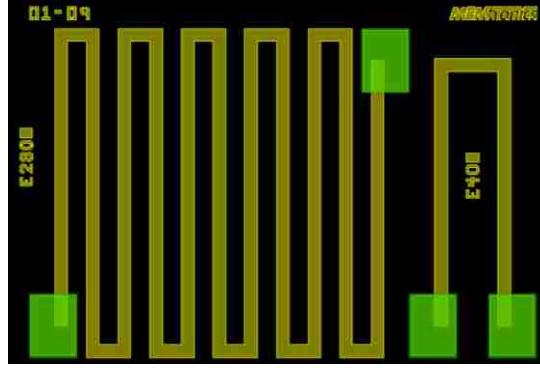
Fig. 4-2   Layout of the conductivity measurement test structures.

from Table 4-1 as follows:

$$T_E = 0.6 \ \mu m \Rightarrow R_E = 33.6 \ n\Omega.m \Rightarrow \sigma_E = 29.76 \ MS / m$$
$$T_M = 1 \ \mu m \Rightarrow R_M = 33 \ n\Omega.m \Rightarrow \sigma_M = 30.3 \ MS / m \qquad (4\text{-}6)$$
$$T_T = 3.9 \ \mu m \Rightarrow R_T = 31.98 \ n\Omega.m \Rightarrow \sigma_M = 31.27 \ MS / m$$

which shows 27% smaller conductivity than bulk gold.

In order to characterize the switch ohmic loss and to understand the loss from each section, i.e bottom electrode, membrane and feed-lines the resistance of those sections were measured. Fig. 4-4 shows that the open structure was used to calibrate the impact of feed-lines in the stationary electrode resistance measurement. The resistance of the open structure was calculated using the sheet resistance of transmission line and the dimensions of open structure. Then the resistance of the open structure was subtracted from the measured resistance value for the open structure to obtain the contact resistance. Then the sheet resistance of bottom electrode was used along with its dimensions to

86
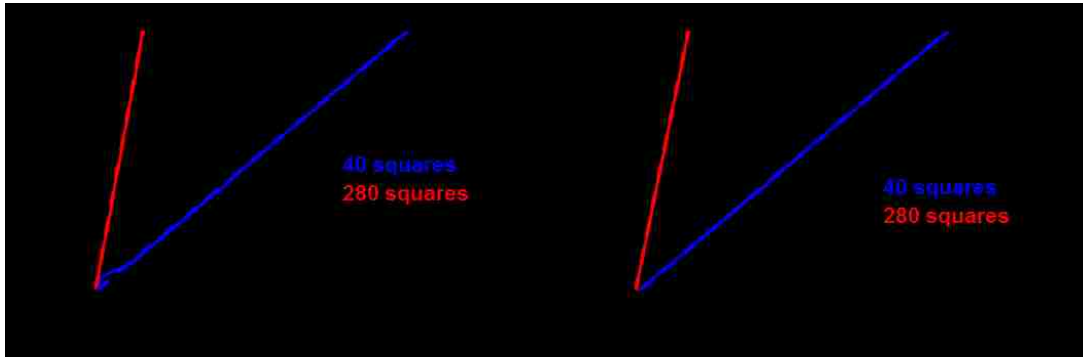
(a)   (b)
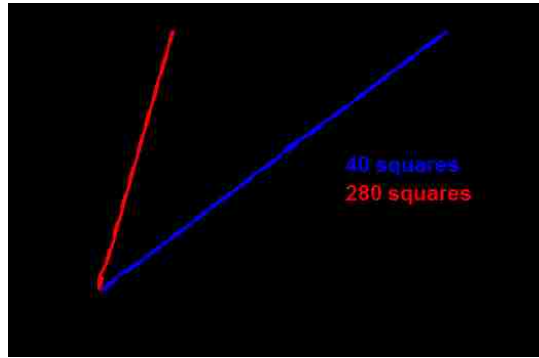
(c)

Fig. 4-3   Measured sheet resistance of (a) stationary electrode, (b) membrane, and (c) transmission line.

calculate and verify the measured values as follows:

$$R_{Open} = R_S \frac{L}{W} = 0.0082 \left(\frac{235}{50}\right) = 39 \quad m\Omega$$

$$R_{Contact} = R_{Cal} - R_{Open} = 207 - 39 = 168 \quad m\Omega \tag{4-7}$$

$$R_{Electrode} = R_S \frac{L}{W} = 0.056 \left(2 + \frac{90}{80} + 2\frac{47}{18}\right) = 467 \quad m\Omega.$$

Similarly, the resistance of the membrane was measured as shown in Fig. 4-5. The

resistance   of   the   membrane   was   obtained   to   be   61   mΩ and

87

(a)	(b)

(c)
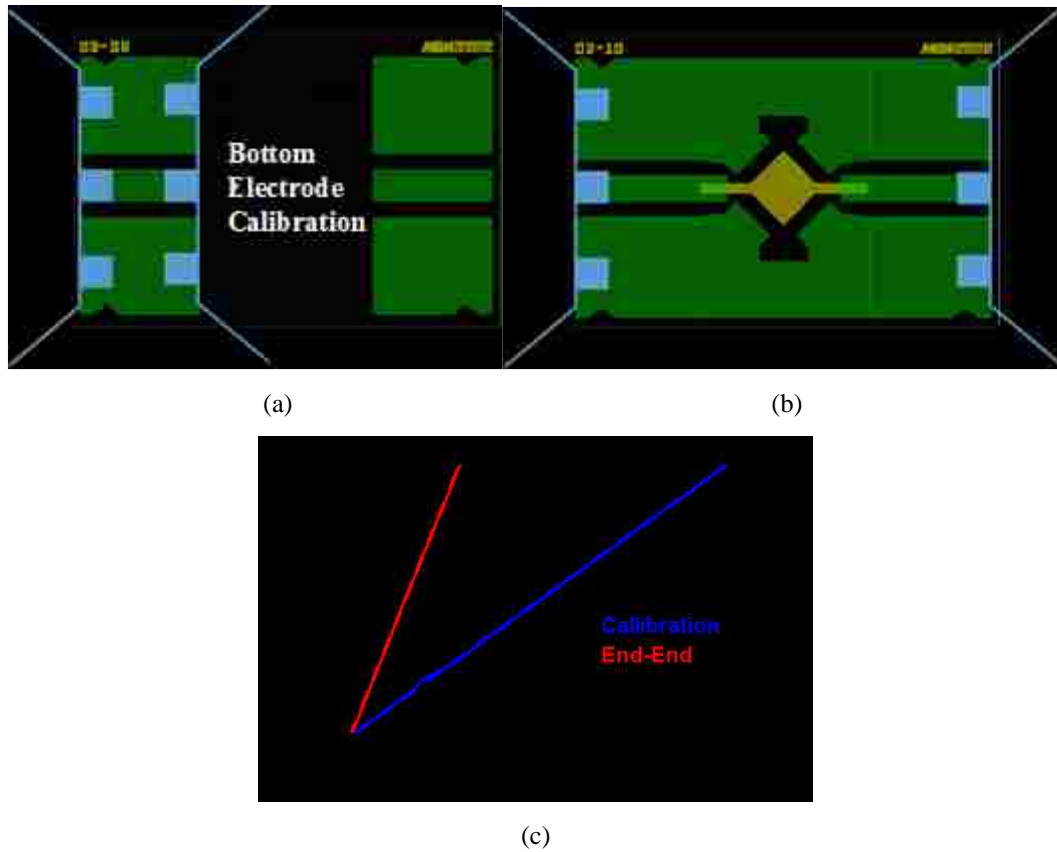
Fig. 4-4   (a) Layout of open structure, (b) layout of bottom electrode, and (c) measured bottom electrode resistance.

it is calculated be 60.5 mΩ as follows:

$$R_{Membrane} = R_S \frac{L}{W} = 0.033 \left(\frac{165}{90} \right) = 60.5 \quad m\Omega. \tag{4-8}$$

As shown in Fig. 4-6, through line was also characterized to obtain the ohmic loss of feed-lines as well as to verify the contact resistance. The resistance of the through line was obtained to be 131 mΩ while the contact resistance was 155 mΩ as follows:

88
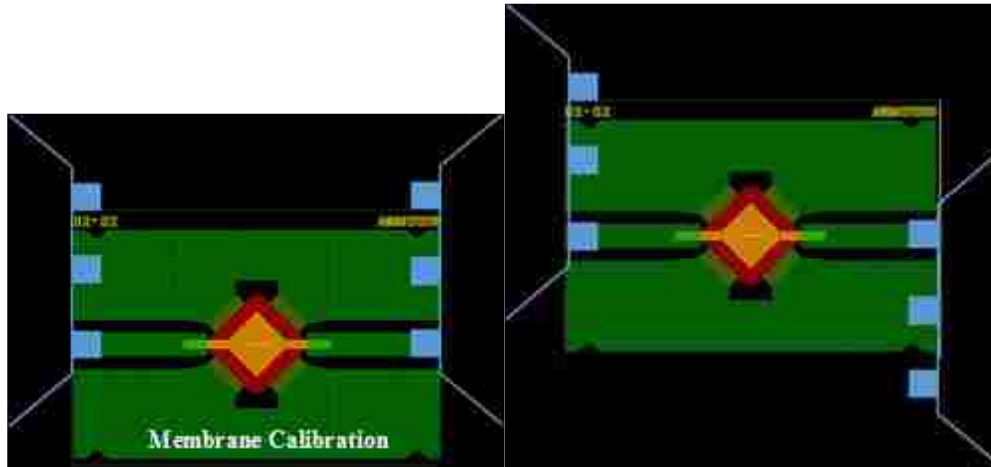
(a)   (b)
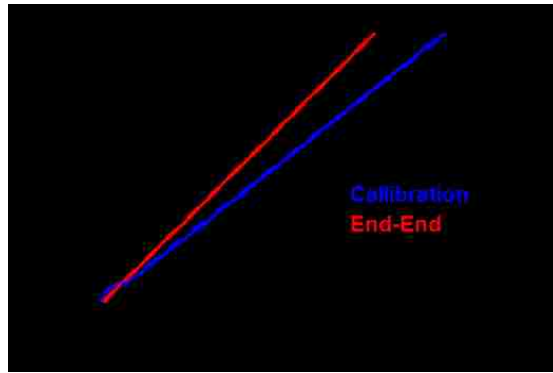
(c)

Fig. 4-5   (a) Layout of membrane for calibration, (b) layout of membrane for end-end measurement, and (c) measured membrane resistance.

(a)   (b)

Fig. 4-6   (a) Layout of through line, and (b) measured through line resistance.

$$R_{Through} = R_S \frac{L}{W} = 0.0082 \left(\frac{800}{50}\right) = 131 \quad m\Omega$$

$$R_{Contact} = R_{Measured} - R_{Through} = 155 \quad m\Omega.$$

(4-9)

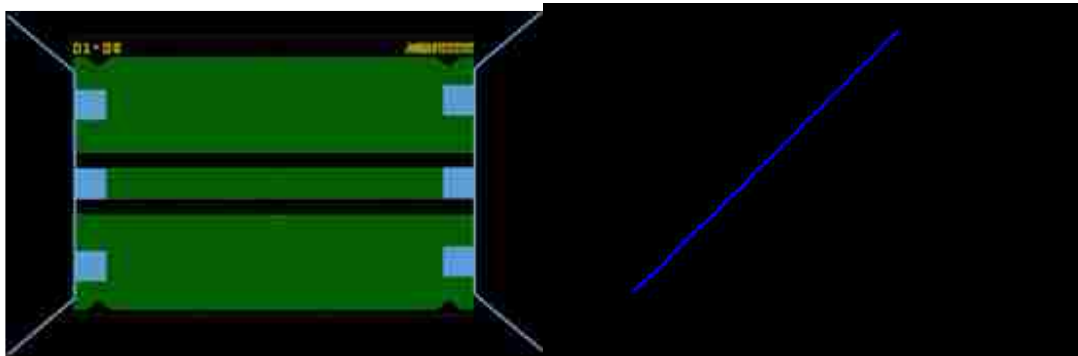Note that the characterized ohmic losses are 39% greater than the designed values. In order to understand what is the impact of ohmic loss in shunt switch performance, we analyzed different loss mechanisms, including conduction loss, substrate loss, mismatch loss and radiation loss, as shown in Fig. 4-7. The conduction loss is the dominant loss factor in frequency of interest such that more than 75% of insertion loss in 25 GHz is coming from conduction loss. Therefore, 39% extra ohmic loss can be easily interpreted as 30% extra insertion loss in the shunt switch.

Fig. 4-7   Different losses of shunt MEMS switch. The results were normalized to the total switch loss.

90

4.2 Substrate Permittivity and Loss Tangent

1mm and 4 mm long transmission lines with 50 Ω characteristic impedance were measured and their scattering parameters were fitted in HFSS by incorporating the measured conductivities of previous section. The permittivity and loss tangent of the substrate was tuned to obtain the best fit to the measured insertion loss and phase as shown in the Fig. 4-8 and Fig. 4-9. The results confirm that the substrate permittivity is 9.3 and its loss tangent is approximately 0.005 which was assumed 10.2 and 0 in the original HFSS design, respectively. The permittivity of 9.3 agrees well with the literature for substrate with perpendicular to Caxis orientation [7]. According to the Fig. 4-7, greater than 0 substrate loss tangent contributes 23% extra insertion loss at 25 GHz to the shunt switch performance.

So, the substrate loss and conduction loss together add more than 53% extra loss to the total insertion loss of the switch. This along with over 6% extra insertion loss due to smaller than expected airgap, adds up to 60% larger than expected insertion loss for the shunt switch.
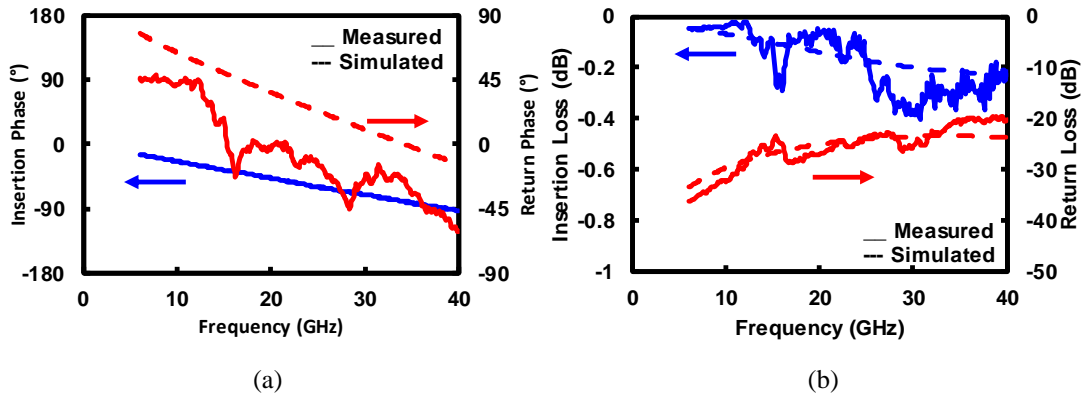
Fig. 4-8 Electromagnetics-simulated (dashed) vs. measured (solid) (a) insertion phase ($<S_{21}$) and return phase ($<S_{11}$) and (b) insertion loss ($|S_{21}|$) and return loss ($|S_{11}|$) of the 1mm transmission line.
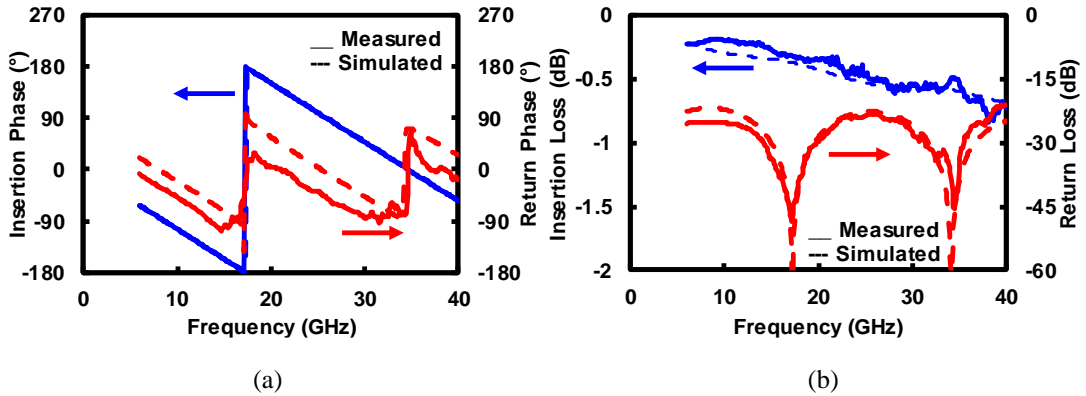
Fig. 4-9 Electromagnetics-simulated (dashed) vs. measured (solid) (a) insertion phase ($<S_{21}$) and return phase ($<S_{11}$) and (b) insertion loss ($|S_{21}|$) and return loss ($|S_{11}|$) of the 4mm transmission line.

The other factor is switch off-capacitance which is 5% larger than expected value and hence the loss in the switch is related to the off-capacitance square then the impact would be 9% in the total insertion loss if and only if the membrane be flat. Therefore, we expect that the switches in the present design show over 62% extra insertion loss than the designed values. From chapter 2, we expected that the shunt switch insertion loss to be

92

less than 0.4 dB in 25 GHz and according to the analysis in this chapter we expect switches with over 0.64 dB insertion loss at 25 GHz. This value matches well with the measured results for the shunt switch shown in chapter 3. Note that this value can increase even further by membrane flatness effect and mismatch loss due to that.

4.3 *Membrane Flatness Characterization*

From equation (4-5), it is evident that airgap variations change the pull-in voltage. In the present wafer, the measured pull-in voltage was from 20 V to 60 V which shows a large variation in airgap because of membrane flatness. From equation (4-3) and equation (4-4), the airgap variations also influence the insertion loss. In this section, we study the influence of the flatness of the membrane on the performance of individual switches and phase shifters. Also, to remove the impact of bad actuation of the switches, only faux switches (the switches with pre-actuated membranes) were examined. HFSS simulations were used to model the measured performance of the switches and phase shifters.

4.3.1   *Individual Switch*

Fig. 4-10 shows the micrograph and profile of a shunt switch along with its scattering performance in both unactuated and faux or pre-actuated states. As it can be

93

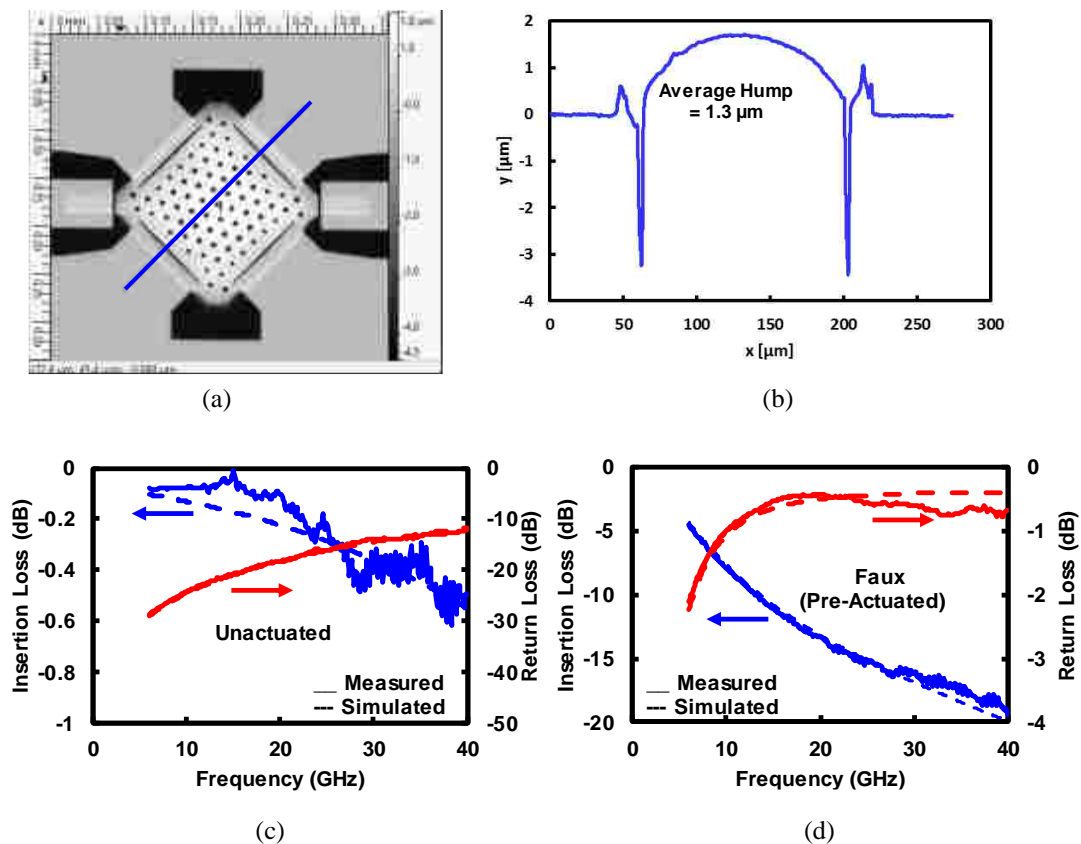Fig. 4-10   (a) Micrograph, (b) profile of the unactuated shunt switch along the cut, (c) electromagnetics-simulated (dashed) vs. measured (solid) insertion loss ($|S_{21}|$) and return loss ($|S_{11}|$) of (c) unactuated and (d) faux shunt switch.

seen the switch is buckled up with average hump of 1.3 µm. This improves the switch loss by reducing the off-capacitance. This causes almost 40% reduction of the insertion loss but 49% increase in the pull-in voltage. As it can be seen from the Fig. 4-10 (c) the insertion loss is almost 0.45 dB in 25 GHz which matches well with the 0.48 dB calculated loss. Also, the pull-in voltage of this switch was measured to be almost 50 V which shows 56% increase to the calculated value of 32 V and matches well with our
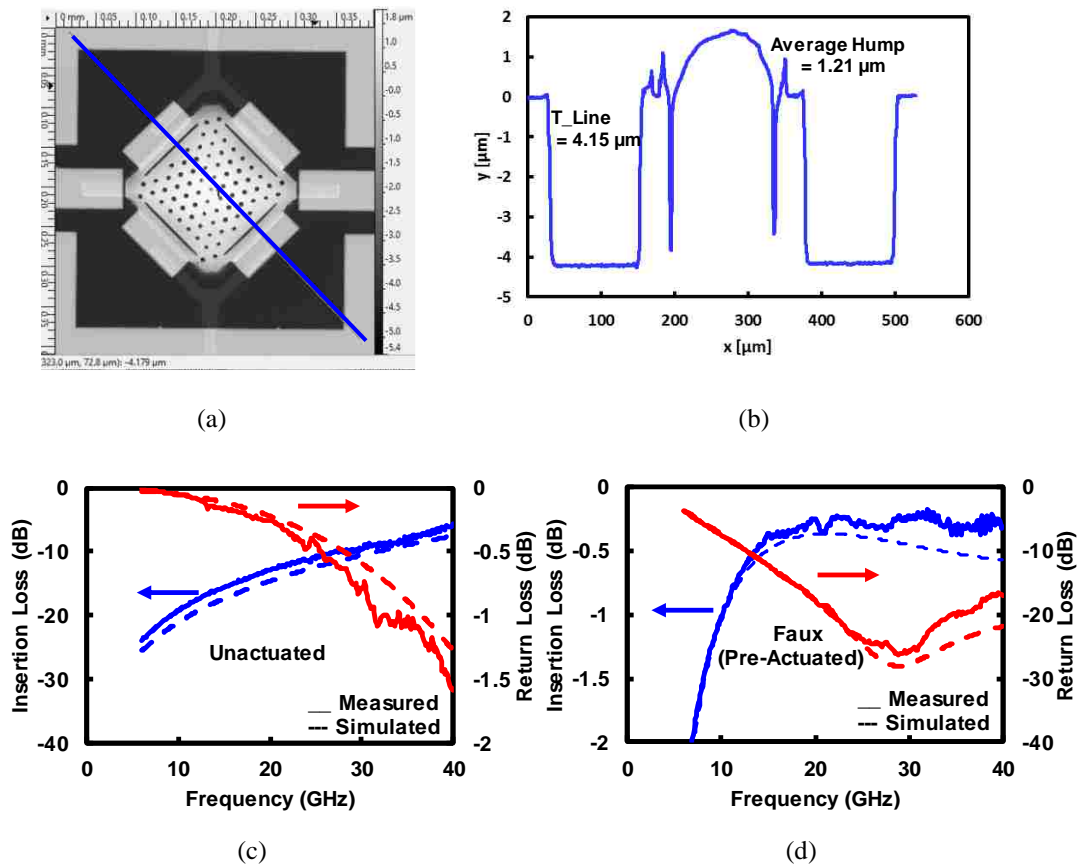
Fig. 4-11 (a) Micrograph, (b) profile of the unactuated series switch along the cut, (c) electromagnetics-simulated (dashed) vs. measured (solid) insertion loss ($|S_{21}|$) and return loss ($|S_{11}|$) of (c) unactuated and (d) faux series switch.

estimation of 49%. The reason for the further increase in the pull-in voltage and further decrease in insertion loss is the fact that the membrane is curved however we averaged the curvature and tried to estimate it with flat membrane.

Similar to the shunt switch, Fig. 4-11 shows the micrograph and profile along with scattering parameters of unactuated and faux series switch. It can be seen that his switch

95

is buckled up by 1.21 µm and has a thicker transmission line which causes the actuation voltage to rise up to 60 V. In practice this switch were overdrived by applying 70 V to make sure it is actuated.

4.3.2   Individual Phase Shifter Basic Cells with Faux Switches

After characterization of individual phase shifter basic cells with faux switches, they were cascaded in ADS circuit simulator to estimate the performance of the multi-bit phase shifters. Fig. 4-12 shows the micrograph of the 22.5° unit cell. As it can be seen from Fig. 4-12 (b) the shunt switch is buckled down by over 1 µm which changes the insertion loss in delayed state. It also influences the performance of the through state by deviating the input impedance and creating the mismatch loss. The 22.5° unit cell exhibits less than 0.9 dB insertion loss, greater than 14 dB return loss, and $21\pm2°$ phase shift between 22 GHz and 26 GHz. We can see that this value is almost 1.8 times higher than the expected designed value in chapter 2. The main reason for this extra loss is 60% extra switch loss as well as the extra 13% loss due to the switch curvature which in total causes 73% extra insertion loss. The rest of extra loss along with 2 GHz frequency shift toward lower frequencies comes from bad actuation of the shunt switch in the delayed state.
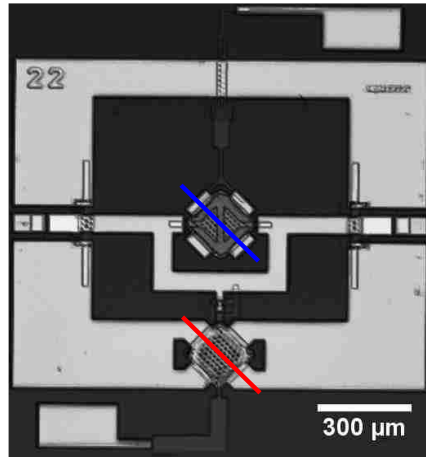
(a)
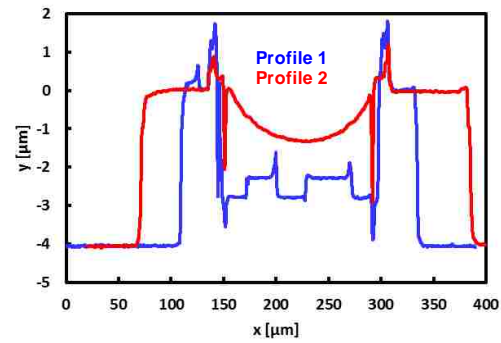
(b)
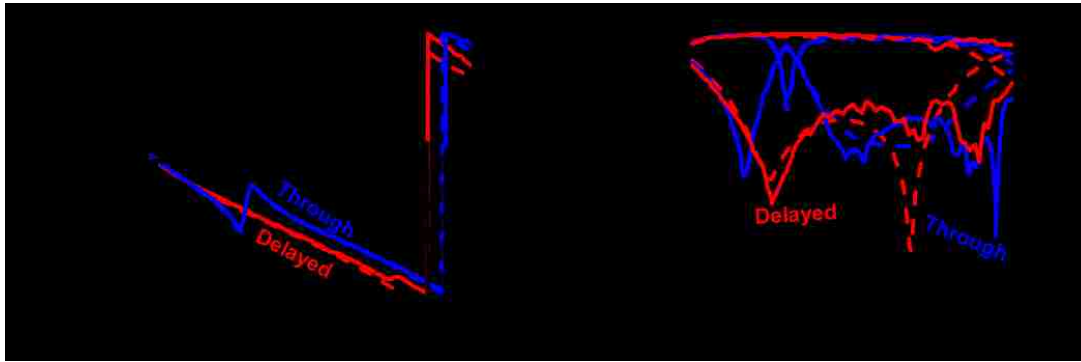
(c)   (d)

Fig. 4-12   (a) Micrograph of 22.5° basic cell with faux switches in through state (b) profile of the
series and shunt switch along the cut. Measured (solid), and 3D electromagnetics simulated (dashed)
(c) insertion phase ($\angle S_{21}$) and (d) insertion loss ($|S_{21}|$) and return loss ($|S_{11}|$) of the 22.5° unit cell.

Fig. 4-13 shows the micrograph of the 45° unit cell. As it can be seen from Fig. 4-13

(b) the shunt switch is buckled down by over 1 µm which changes the insertion loss in

delayed state. It also influences the performance of the through state by deviating the

input impedance and creating the mismatch loss. The 45° unit cell exhibits less than 1.1

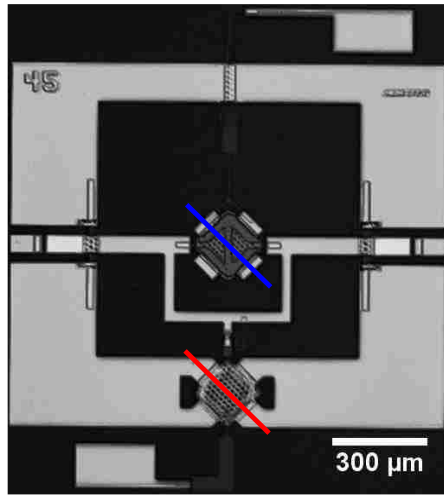dB insertion loss, greater than 17 dB return loss, and 38±5° phase shift between 22 GHz
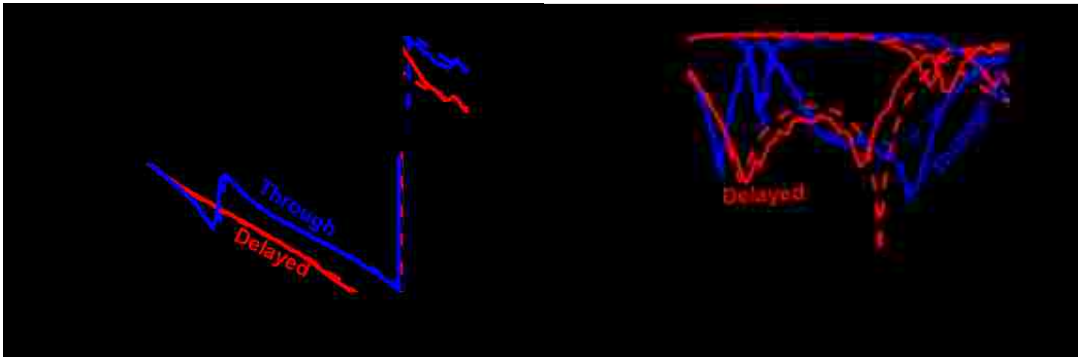
Fig. 4-13 (a) Micrograph of 45° basic cell with faux switches in through state (b) profile of the series and shunt switch along the cut. Measured (solid), and 3D electromagnetics simulated (dashed) (c) insertion phase ($\angle S_{21}$) and (d) insertion loss ($|S_{21}|$) and return loss ($|S_{11}|$) of the 45° unit cell.

and 26 GHz. We can see that the insertion loss value is almost 2 times higher than the expected designed value. The main reason for this extra loss is 60% extra switch loss as well as the extra 13% loss due to the switch curvature which in total causes extra 73% insertion loss. Moreover, there are extra loss due to bad actuation of shunt switch in the
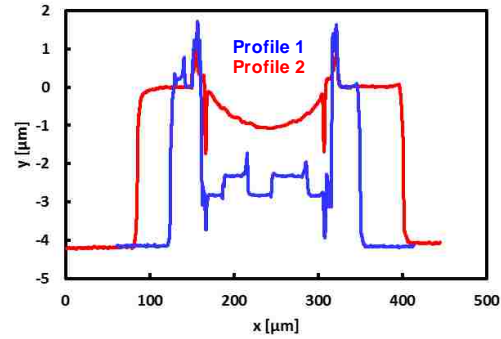
(a)

(b)

(c)

(d)

Fig. 4-14　(a) Micrograph of 90° basic cell with faux switches in through state (b) profile of the series and shunt switch along the cut. Measured (solid), and 3D electromagnetics simulated (dashed) (c) insertion phase ($\angle S_{21}$) and (d) insertion loss ($|S_{21}|$) and return loss ($|S_{11}|$) of the 90° unit cell.

delayed state as well as 15% smaller MIM capacitance which contribute to the rest of

extra loss.

Fig. 4-14 shows the micrograph of the 90° unit cell. As it can be seen from Fig. 4-14

(b) the shunt switch is buckled up by over 0.1 µm while the series switch is buckled

down by over 0.2 µm which reduces the insertion loss in delayed state. It also influences the performance of the through state by deviating the input impedance and creating the mismatch loss. The 90° unit cell exhibits less than 1.1 dB insertion loss, greater than 13 dB return loss, and 92±2° phase shift between 22 GHz and 26 GHz. We can see that the insertion loss value is almost 2 times higher than the expected designed value. The main reason for this extra loss is 60% extra switch loss as well as the extra 19% loss due to the switch curvature which in total causes extra 79% insertion loss. Moreover, there are extra loss due to the 15% smaller than expected MIM capacitors and on-capacitance of the switches which increases the insertion loss in the through state and causes the frequency shift.

Fig. 4-15 shows the micrograph of the 180° unit cell. As it can be seen from Fig. 4-15 (b) the shunt switch is buckled down by over 0.18 µm while the series switch is buckled down by over 0.21 µm which increases the insertion loss in delayed state. It also influences the performance of the through state by deviating the input impedance and creating the mismatch loss. The 180° unit cell exhibits 170±12° phase shift with less than 1.8 dB insertion loss, and better than 18 dB return loss between 22 GHz and 26 GHz. We can see that the insertion loss value is almost 1.8 times higher than the expected
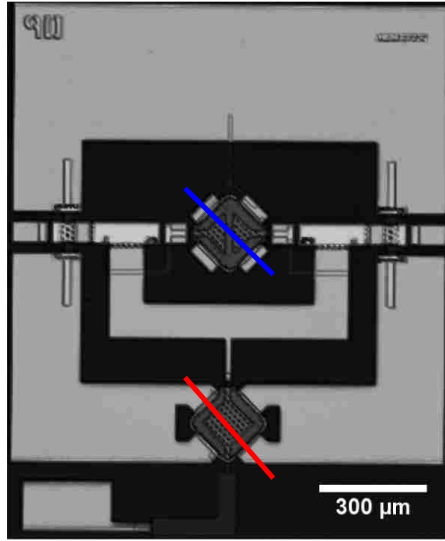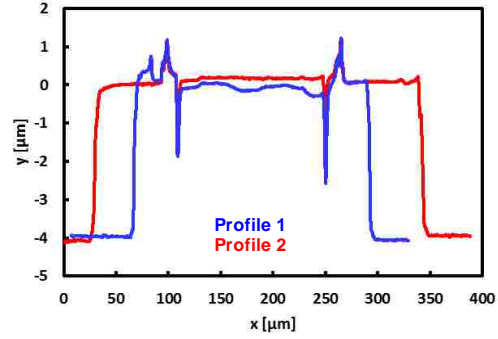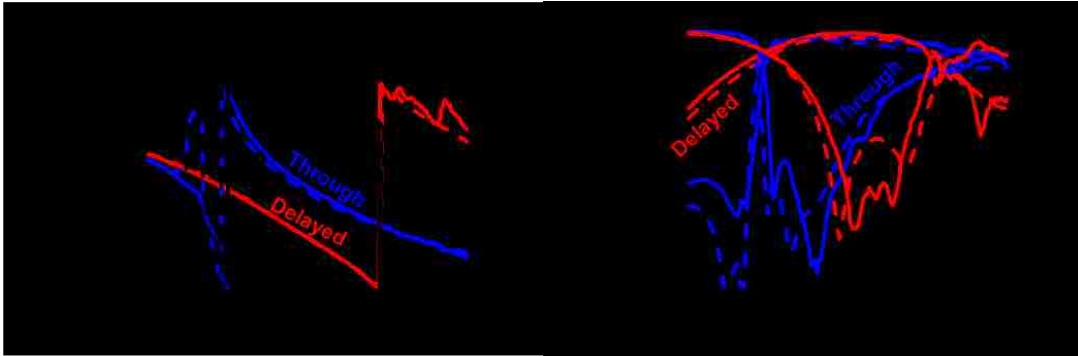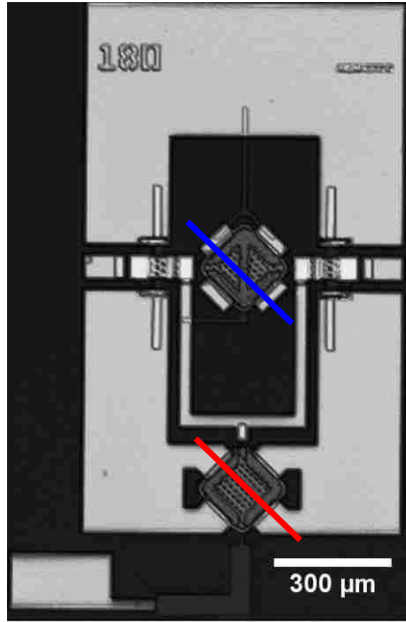
100
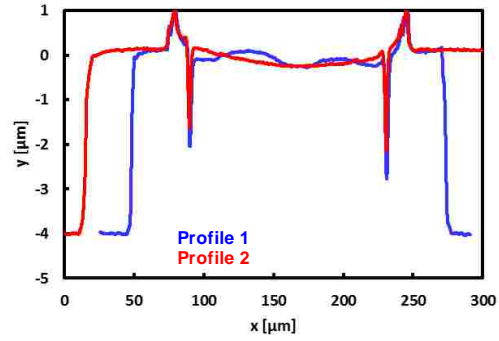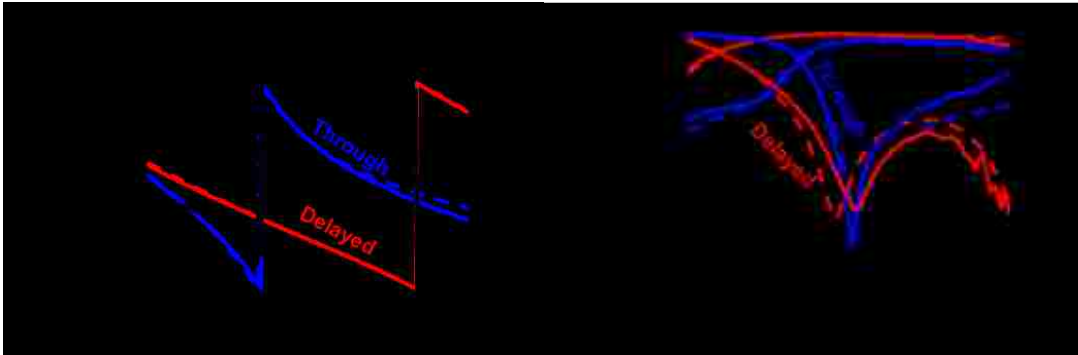
Fig. 4-15 (a) Micrograph of 180° basic cell with faux switches in through state (b) profile of the series and shunt switch along the cut. Measured (solid), and 3D electromagnetics simulated (dashed) (c) insertion phase ($\angle S_{21}$) and (d) insertion loss ($|S_{21}|$) and return loss ($|S_{11}|$) of the 180° unit cell.

designed value. The main reason for this extra loss is 60% extra switch loss as well as the extra 18% loss due to the switch curvature which in total causes extra 78% insertion loss.

Note that, there are extra loss due to the 15% smaller than expected MIM capacitors and

on-capacitance of the switches which influences the mismatch loss and increases the insertion loss in the through state and causes the frequency shift.

4.3.3 Multi-bit Phase Shifters with Faux Switches

After evaluating the source of extra insertion loss in individual basic phase shifter cells by using their measured optical profiles, these basic cells were cascaded in the ADS circuit simulator to evaluate their performance with faux switches and separate the loss from bad actuation from the intrinsic loss of the circuit. In this regard, first a 2-bit phase shifter with real switches was measured when the switches are suspended, i.e. both of states delaying, then the results compared with the circuit-simulator cascaded 2-bit phase shifter comprised of 180° and 90° in the delayed states. The delayed state was selected because it is independent of switch actuation for 180° and 90° with symmetric switch actuation topology. The 500-µm-long 50-Ω coplanar waveguide was inserted between the 90° and 180° unit cells in circuit simulator to imitate the actual phase shifter. Fig. 4-16 confirms that the individual unit cells' performance can be cascaded in circuit simulator to estimate the performance of multibit phase shifter accurately. Therefore, the results for the ADS-cascaded phase shifters is reported in the following part.
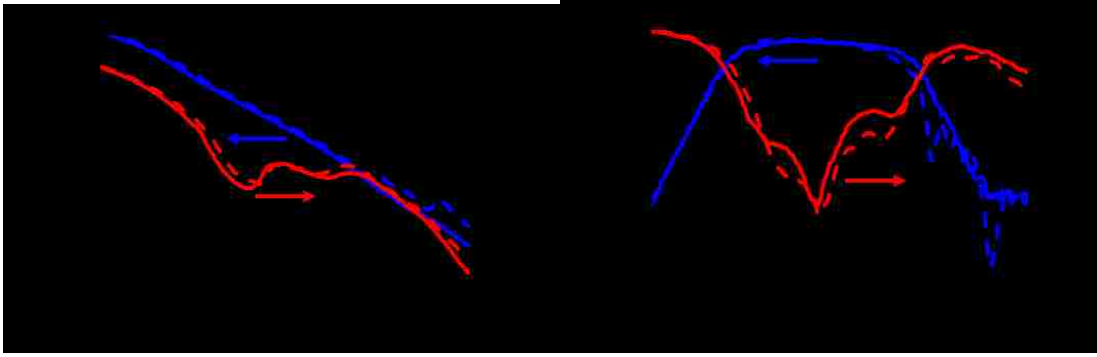
(a)   (b)

Fig. 4-16   (a) Measured (solid), and ADS-cascaded (dashed) (a) insertion phase ($\angle S_{21}$) and return phase ($\angle S_{11}$) and (b) insertion loss ($|S_{21}|$) and return loss ($|S_{11}|$) of the last state of the 2-bit phase shifter.
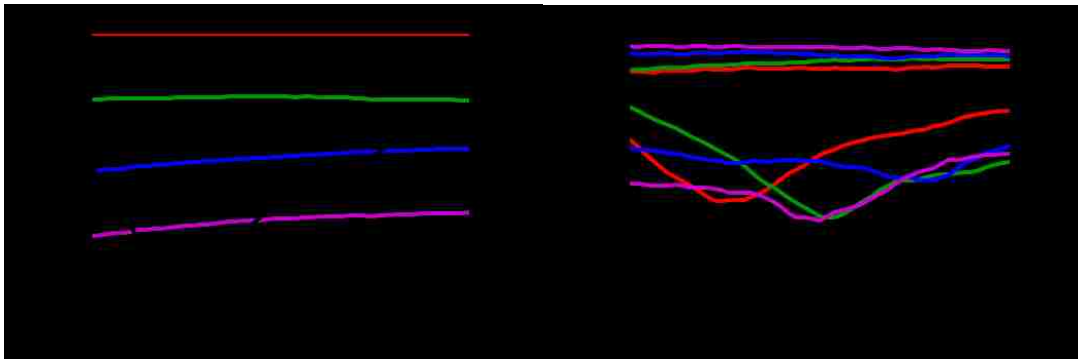
(a)   (b)

Fig. 4-17   ADS-cascaded (a) insertion phase ($\angle S_{21}$) and RMS phase error and (b) insertion loss ($|S_{21}|$) and return loss ($|S_{11}|$) of the 2-bit phase shifter.

Fig. 4-17 shows the performance of the 2-bit phase shifter. Even in the worst case across the band of 21−26 GHz, the root-mean-square phase error of the present 2-bit phase shifter is less than 13°, the insertion loss is less than 2.7 dB, and the return loss is greater than 12 dB. The loss is 1.5 times higher than the designed value and there is 3 GHz of downward frequency shift. The main reason for this is 50% extra loss of the

103

<div align="center">(a)   (b)</div>

Fig. 4-18   ADS-cascaded (a) insertion phase ($\angle S_{21}$) and RMS phase error and (b) insertion loss ($|S_{21}|$) and return loss ($|S_{11}|$) of the 3-bit phase shifter.

conductors and substrate, and the main reason for the frequency shift is 15% less capacitance value for both MIMs and switches. There is a 500-µm-long 50-Ω coplanar waveguide which shows only 50% extra loss due to conductivity and substrate loss changes. The extra loss were canceled by coupling between basic cells and the impedance match, so the overall insertion loss is only 50% over the designed value.

Fig. 4-18 shows the performance of the 3-bit phase shifter. Across frequency range of 21.5-24.5 GHz, root-mean-square phase error of the present 3-bit phase shifter is less than 14°, the insertion loss is less than 3.4 dB, and the return loss is greater than 12 dB. With further optimization of the switches and CPW structure to minimize the radiation loss of individual bits, the overall insertion loss of 3-bit phase shifter can be reduced well over 1dB. The loss is 1.7 times higher than the designed value and there is 3 GHz of

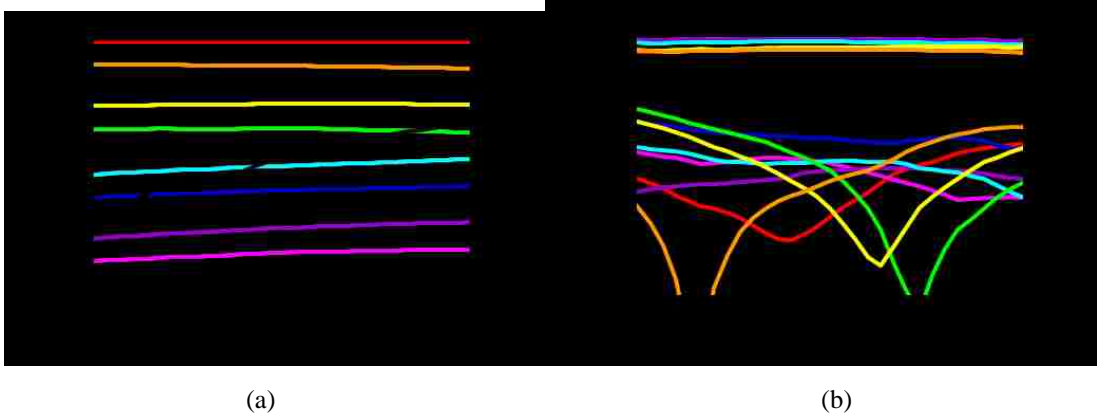downward frequency shift. The main reason for the extra loss is 60% extra loss of the switches and the main reason for the frequency shift is 15% less capacitance value for both MIMs and switches. There is no extra transmission line in this case to reduce the loss and as a matter of fact there is even some further loss because of smaller than expected capacitance values. Also there is some contribution due to 0.1-0.2 µm down-buckling of the switches which adds the insertion loss to 1.7 times of expected value.

According to the results obtained from 3-bit phase shifter, the present design requires tighter manufacturing tolerance to work properly. Considering the immaturity of RF MEMS technology, the most important achievement in this work is decreasing number of required MEMS switches for a phase shifter that directly impact yield and reliability. Nevertheless, the multibit phase shifters with faux switches show the proof of principle for the present design and show that the present design can be well compared to the other state of the art MEMS phase shifters as listed in Table 4-2.

Table 4-2   Summary of State-Of-The-Art MEMS Phase Shifters

Year	2003	2004	2006	2008	2013	2016
Reference	[8]	[9]	[10]	[11]	[12]	This Work
Design	Switched Line	Loaded Line	Slow Wave	High/Low-Pass	DMTL	High/Low-Pass
Variable	ℓ	C	L, C	C	C	C
Dispersion	Linear	Linear	Linear	Low	Low	Low
Bandwidth (GHz)	1−20	75−110	1−50	8−12	29-30	21.5-24.5
Resolution	4 bits	3 bits	2.5 bits	5 bits	3 bits	3-bits
RMS Error			$< 6°$	$< 10°$	$<4°$	$< 14°$
Insertion Loss	< 4 dB	< 6 dB	< 1.4 dB	< 9 dB	< 7 dB	< 3.4 dB
Return Loss	> 10 dB	> 10 dB	> 21 dB	> 10 dB	> 8 dB	> 12 dB
SPST Switches	16	28	50	20	32	6
Size	21 mm^2	10 mm^2	12 mm^2	9 mm^2	64 mm^2	5.3 mm^2

References

[1] https://www.bruker.com/products/surface-and-dimensional-analysis/stylus-profilometers.html?gclid=Cj0KEQjwkN3KBRCu2fWmy9LLqN4BEiQANP9-Wv6b2fTHoGyuKLqCRicfvbPjT4dS2270ZhYW2FIEvTMaAqki8P8HAQ

[2] https://www.bruker.com/products/surface-and-dimensional-analysis/3d-optical-microscopes.html?gclid=Cj0KCQjwkN3KBRCuARIsADT_flpCG9hdIckpMgX0ylrBkcWqLBEXm2ql4RoIOu0Ajkb8kZxeJwy36FQaAmliEALw_wcB

[3] G. M. Rebeiz, RF MEMS: *Theory, Design, and Technology*. New York: Wiley, 2003, pp. 87–103.

[4] http://eecs.oregonstate.edu/matdev/man/Agilent4155C_4156C_Users_Guide_Vol2.pdf

[5] https://www.cascademicrotech.com/products/probes/rf-microwave/rf-microwave-probes

[6] http://www.sardarsinghsir.com/MSc/MSc%20pdf%20files/Four-Probe-Method.pdf

[7] http://global.kyocera.com/prdct/fc/product/pdf/s_c_sapphire.pdf

[8] G. L. Tan, R. E. Mihailovich, J. B. Hacker, J. F. DeNatale, and G. M. Rebeiz, "Low-loss 2- and 4-bit TTD MEMS phase shifters based on SP4T switches," *IEEE Trans. Microw. Theory Techn.,* vol. 51, no. 1, pp. 297–304, Jan. 2003.

[9] J. J. Hung, L. Dussopt, and G. M. Rebeiz, "Distributed 2- and 3-bit *W*-band MEMS phase shifters on glass substrates," *IEEE Trans. Microw. Theory Tech.,* vol. 52, no. 2, pp. 600–606, Feb. 2004.

[10] B. Lakshminarayanan and T. M. Weller, "Design and modeling of a 4-bit slow-wave phase shifter," *IEEE Trans. Microwave Theory Techniques*, vol. 54, no. 1, pp. 120−127, Jan. 2006.

[11] M. A. Morton and J. Papapolymerou, "A packaged MEMS-based 5-bit X-Band high-pass/low-pass phase shifter," *IEEE Trans. Microwave Theory Tech.*, vol. 56, no. 9, pp. 2025−2031, Sep. 2008

[12] M. Unlu, S. Demir, and T. Akin, "A 15–40-GHz Frequency Reconfigurable RF MEMS Phase Shifter," *IEEE Trans. Microwave Theory Tech*., vol. 61, no. 8, pp. 2865–2877, Aug. 2013.

Chapter 5 Conclusions

5.1 Conclusions of This Dissertation

This dissertation studies design, implementation, characterization and modeling of novel metamaterial-based low-dispersion multibit phase shifters that use single-pole-single-throw MEMS capacitive switches to switch between right-handed (low-pass) and left-handed (high-pass) states for the specified phase shift. Three-dimensional finite-element electromagnetic simulation was used to design the basic unit cells. Each phase shifter unit cell is based on a coplanar slow-wave structure with defected ground and uses two MEMS switches in series and parallel configurations. In this dissertation, for the first time, we enhanced the maximum achievable phase shift of metamaterial-based MEMS phase shifter unit cell from 45° to 180°.

Thanks to our novel 180° unit cell design, for the first time, the number of required MEMS switches for multibit phase shifter was reduced to two times of bits count such that a 3-bit phase shifter requires only six MEMS switches. For 2-bit and 3-bit phase shifters fabricated on a 600-µm-thick sapphire substrate, a relatively flat phase shift was obtained across the band of 21.5–24.5 GHz so that the root-mean-square phase error was

reduced to below 14°. Across the same frequency band, the present 2-bit and 3-bit phase shifters have less than 2.7 dB and 3.4 dB insertion loss, respectively.

Accurate modeling and electromagnetic simulations were performed to characterize the beyond expectation insertion loss sources. The loss is mainly due to higher-than-expected switch loss because of extra ohmic loss, extra substrate loss and smaller than expected airgap of the switch. Furthermore, there is more loss associated with the non-flat membrane as well as radiation loss. This can be further reduced by optimizing the MEMS switch and the coplanar waveguide. Nevertheless, the present design principle appears to be sound and can lead to phase shifters with high performance, yield and reliability with low cost for electrically large phased-array antennas.

5.2 Recommendation for Future Study

The main recommendation for the future studies can be improvement on the MEMS switch actuation and insertion loss. Also, an optimized fabrication process can improve the reliability. As shown in chapter 4, there are narrow arms of the stationary electrode in the shunt switch that causes large conduction loss. This can be easily improved and

109

(a)   (b)

(c)   (d)
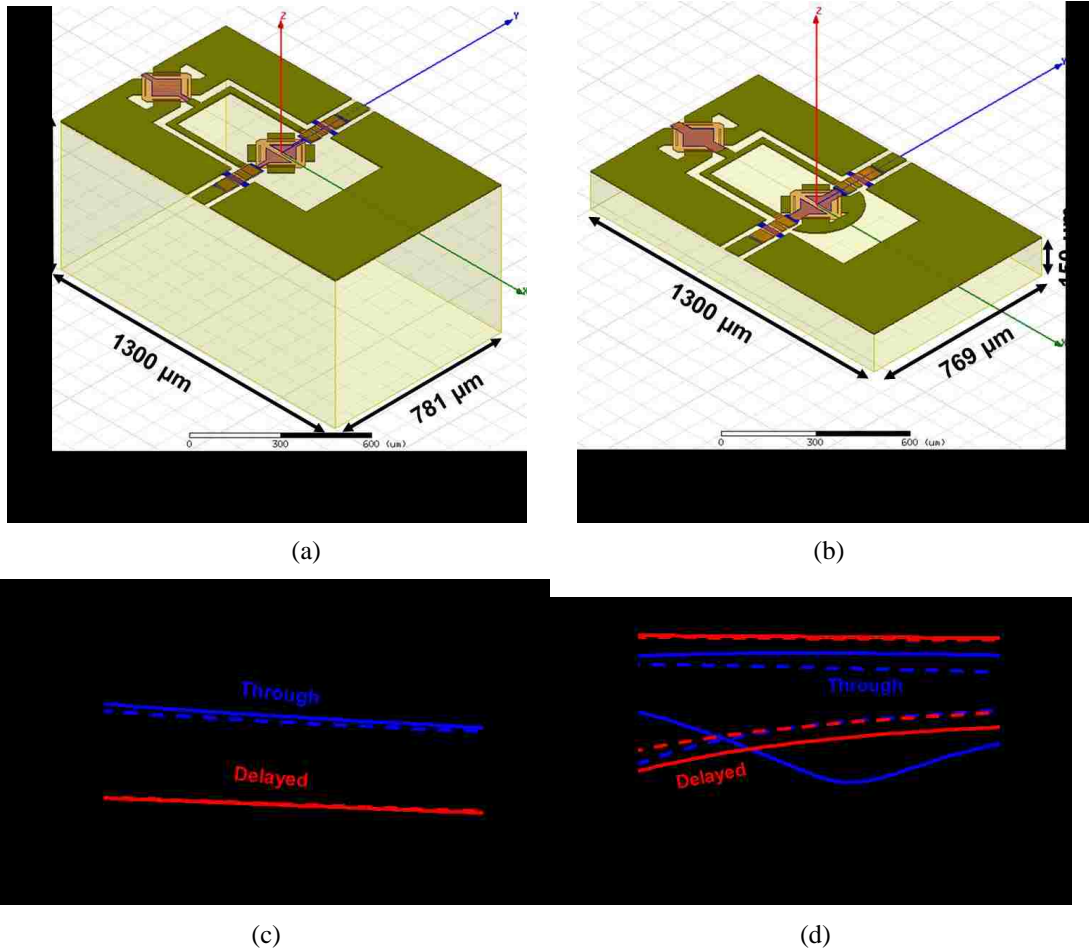
Fig. 5-1   Layout of (a) present, and (b) improved 180° unit cell. Present (dashed) and improved (solid) (c) insertion phase ($\angle S_{21}$) and (d) insertion loss ($|S_{21}|$) and return loss ($|S_{11}|$) of the 180° unit cell.

optimized by widening those arms, however it should be done carefully because it adds extra unactuated state capacitance, C_{off}. Moreover, the substrate loss can be reduced by using thinner substrate. From chapter 2, it was evident that the novel 180° has the greatest loss among the phase shifter unit cells. Our HFSS simulations in Fig. 5-1 shows that there are room for over 33% reduction of its insertion loss by thinning the substrate and

110

(a)   (b)

$-jX_N$ $-jX_N$ jX_N jX_N

$-jB_N$ jB_N

(c)   (d)
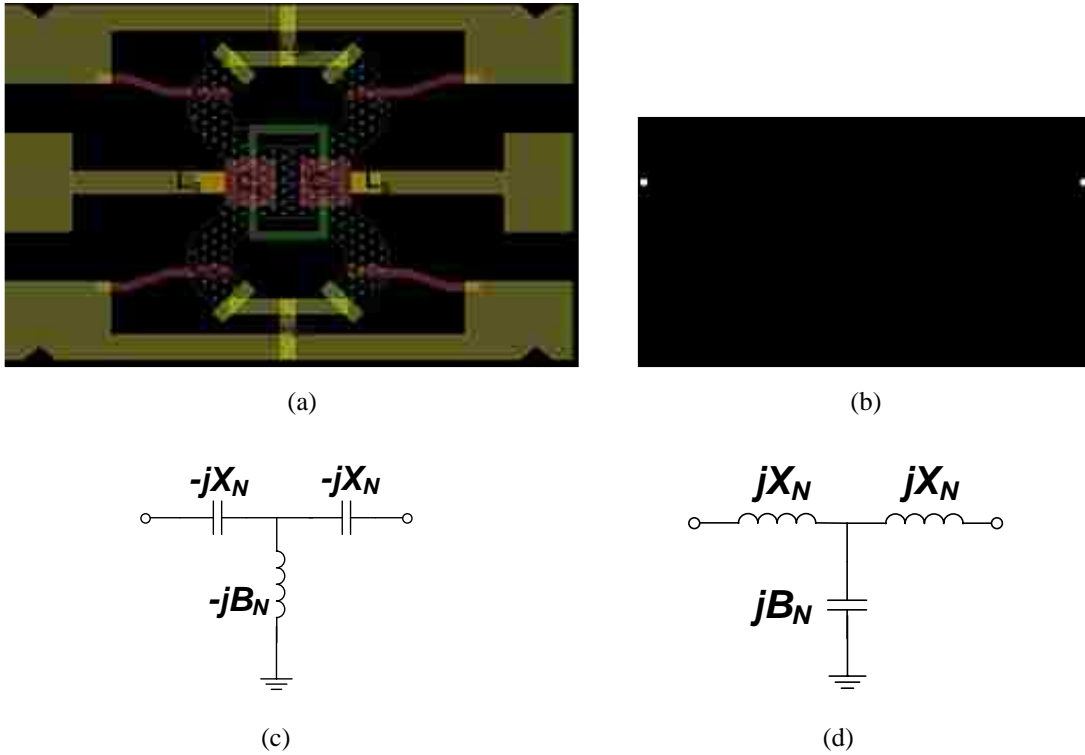
Fig. 5-2   (a) Layout, and (b) equivalent circuit model of a single switch MEMS phase shifter. (c) Through, and (d) delayed state.

modifying the series switch such that more filed being confined in the through state.

Number of switches play a critical role in the insertion loss of the present design. Revisiting the design principles of the high-pass/low-pass filters [1], shows that it is possible to design a low-pass/high-pass structure by using only one MEMS switch as shown in Fig. 5-2. The switch can be replaced by temperature independent switch. In this design, we ignored the losses to simplify the calculations. In the high-pass (left-handed) case, switch is unactuated so the shunt capacitor, C_{SH} is small and the shunt path is

111

inductive. In this case, RF signal can go through. In the low-pass (right-handed) case,

switch is actuated so the shunt capacitor, C_{SH} is large and the shunt path is capacitive.

Also since the series capacitor, C_S is large the series path is inductive. Whether this

design is valid or not, detailed study and control experiments are needed.

References

[1] R. V. Grover, "Broad-Band Diode Phase Shifters," *IEEE Trans. Microwave Theory Tech.*, vol. 20, no. 5, pp. 314–323, May 1972.

Publications

[1] **V. Gholizadeh**, M. Asadi, Y. Ning, C. Palego, J. C. M. Hwang, D. Scarbrough, and C. L. Goldsmith, "Compact, Wideband, Low-dispersion, Multibit MEMS Phase Shifters," under preparation for *IEEE Trans. Microwave Theory Tech*, 2017.

[2] X. Ma, X. Du, **V. Gholizadeh**, H. Li, X. Cheng, and J. C. M. Hwang, "One Resistor and Two Capacitors:An Electrical Engineer's Simple View of a Biological Cell," *IEEE International Microwave Workshop Series on Advanced Materials and Processes,* Pavia, Italy, September 2017, accepted for publication.

[3] N. Gholizadeh, X. Ma, H. Li, X. Du, Y. Ning, **V. Gholizadeh**, X. Cheng and J. C. M. Hwang, "Ultra-wideband Electromagnetic Detection of Biological Cells," *IEEE MTT-S 89th ARFTG Microwave Meas. Symp*. Dig. Honolulu, HI, June 2017, accepted for publication.

[4] X. Ma, X. Du, C. R. Multari, Y. Ning, X. Luo, **V. Gholizadeh**, C. Palego, X. Cheng, and J. C. M. Hwang, "Reproducible Broadband Measurement for Cytoplasm Capacitance of a Biological Cell," *IEEE MTT-S Int. Microwave Symp. Dig.,* San Francisco, CA, May. 2016.

[5] **V. Gholizadeh**, M. Asadi, Y. Ning, C. Palego, J. C. M. Hwang, D. Scarbrough, and C. L. Goldsmith, "Low-dispersion 180° phase shifter using two synchronized MEMS switches," *IEEE LEC.*, Bethlehem, PA, Aug. 2016, pp. 35–37.

[6] **V. Gholizadeh**, M. Asadi, Y. Ning, C. Palego, J. C. M. Hwang, D. Scarbrough, and C. L. Goldsmith, "Low-dispersion Metamaterial-based Phase Shifters with Reduced Size and Number of MEMS switches," *IEEE MTT-S Int. Wireless Symp. Dig*., Shanghai, China, Mar. 2016, pp. 1–4.

[7]   X. Ma, X. Du, C. R. Multari, Y. Ning, C. Palego, X. Luo, **V. Gholizadeh**, X. Cheng, and J. C. M. Hwang, "Broadband Single-Cell Detection with a Coplanar Series Gap," *IEEE MTT-S 86th ARFTG Microwave Meas. Symp. Dig*. Atlanta, GA, Dec. 2015.

[8]   Y. Ning, X. Ma, C. R. Multari, X. Luo, **V. Gholizadeh**, C. Palego, X. Cheng, and J. C. M. Hwang, "Improved broadband electrical detection of individual biological cells," *IEEE MTT-S Int. Microwave Symp. Dig*., Phoenix, AZ, May. 2015, pp. 1–3.

[9]   **V. Gholizadeh**, Y. Ning, X. Luo, C. Palego, J. C. M. Hwang, and C. L. Goldsmith, "Improved Compact, Wideband, Low-dispersion, Metamaterial-based MEMS Phase Shifters," *IEEE MTT-S Int. Wireless Symp. Dig.*, Shenzhen, China, Mar. 2015, pp. 1–4.

[10]   C. Palego, Y. Ning, **V. Gholizadeh**, X. Luo, J. C. M. Hwang, and C. L. Goldsmith, "Compact, wideband, low-dispersion, metamaterial-based MEMS phase shifters," *IEEE MTT-S Int. Microwave Symp. Dig*., Tampa, FL, Jun. 2014, pp. 1–4.

[11]   **V. Gholizadeh**, A. Rostami, S. Golmohammadi, K. Abbasian, and A. Javadi, "Non-singular material parameters for arbitrarily elliptical-cylindrical invisibility cloaks," *Optik*, vol. 124, no. 15, pp. 2174–2179, 2013.

[12]   A. Javadi, A. Rostami, K. Abbasian, and **V. Gholizadeh**, "Evolution of nonclassical light propagating through passive optical coupled waveguides: Entanglement dynamic," *Optik*, vol. 122, no. 22, pp. 2034–2038, 2011.

Vita

Vahid Gholizadeh was born on 1983 in Tabriz, Iran. He received the B.S. degree in electrical engineering and the M.S. degree in photonic engineering from University of Tabriz, Tabriz, Iran in 2007 and 2011, respectively. Since 2012, he has been pursuing his Ph.D. degree in electrical engineering at Lehigh University, Bethlehem, Pennsylvania. During his study at Lehigh University, he had been awarded with P.C. Rossin Doctoral Fellowship since 2014. In 2012, he was also awarded with Dean's Doctoral Student Assistantship by P. C. Rossin College of Engineering and Applied Science, Lehigh University.

In summer 2015, he worked as an intern at Anadigics Inc. on characterization and compact modeling of GaAs and GaN PHEMTs. His research interest includes RF MEMS, Metamaterials, Phase shifters, compound semiconductors, HBTs, HEMTs, CMOS Biosensor, CMOS-based silicon photonics and other microwave devices and circuits. He is a student member of IEEE Microwave Theory and Techniques Society.